

MODELING AND ANALYSIS OF STOCHASTIC BASE FLOW UNCERTAINTIES
IN WALL-BOUNDED SHEAR FLOWS

by

Dhanushki B. Hewawaduge

APPROVED BY SUPERVISORY COMMITTEE:

Armin Zare, Chair

Stefano Leonardi

Todd Griffith

Justin Koeln

Copyright © 2022

Dhanushki B. Hewawaduge

All rights reserved

*Dedicated to my parents, my brother,
and all my teachers.*

MODELING AND ANALYSIS OF STOCHASTIC BASE FLOW UNCERTAINTIES
IN WALL-BOUNDED SHEAR FLOWS

by

DHANUSHKI B. HEWAWADUGE , BS, MS

THESIS

Presented to the Faculty of
The University of Texas at Dallas
in Partial Fulfillment
of the Requirements
for the Degree of

MASTER OF SCIENCE IN
MECHANICAL ENGINEERING

THE UNIVERSITY OF TEXAS AT DALLAS

December 2022

ACKNOWLEDGMENTS

It is a pleasure to express my sincere gratitude and thanks to my mentor Dr. Armin Zare who expertly guided me through my graduate education in Mechanical Engineering. His dedication, timely feedback, meticulous scrutiny, and scholarly advice have helped me to a great extent to accomplish this task in completing my thesis. His unwavering enthusiasm kept me constantly engaged with my research that helped make my time in his group immensely gainful.

I would like to thank Dr. Todd Griffith, Dr. Stefano Leonardi, and Dr. Justin Koeln for serving on my committee and providing me with insightful comments. My sincere thanks also goes to Dr. Tyler Summers with whom I have collaborated , on my first publication.

I thank profusely all the faculty who have taught me throughout my graduate period in the Mechanical Engineering Department. I will be forever grateful for their competent guidance in moulding my academic enhancement.

My deepest thanks for my loving parents Cyril and Vasanthi, and my brother Chamith for being my constant emotional support throughout this journey. I will be forever grateful for their limitless love and strength that help me get back on my feet every time I fall.

January 2022

MODELING AND ANALYSIS OF STOCHASTIC BASE FLOW UNCERTAINTIES
IN WALL-BOUNDED SHEAR FLOWS

Dhanushki B. Hewawaduge , MS
The University of Texas at Dallas, 2022

Supervising Professor: Armin Zare, Chair

Spatially distributed dynamical systems arise in a variety of science and engineering problems and are typically described by Partial Integro-Differential (P(I)DEs) equations. Important examples of such systems include the wave equations, Maxwell equations, Burgers equations, Schrodinger equations, and the Navier-Stokes equations. An appropriate way to study and control such systems often involves the spatio-temporal analysis of linearized forms of these equations around base profiles, which either describe a steady-state solution or a long-time averaged mean of a simulation- or experiment-based field. In addition, deterministic or stochastic forcing is commonly used to compensate for the neglected nonlinear terms and evaluate the input-output features of the linearized dynamics. However, uncertainty in both the base profile and nature of the inputs challenge the effectiveness of linearized models for analysis and control design. Motivated by applications in the analysis and control of complex fluid flows, this thesis demonstrates how modeling sources of stochastic base flow uncertainty can enable physical discovery and statistical modeling of quantities of interest.

We provide an input-output framework to analyze the effect of base flow perturbations on the stability and receptivity properties of transitional and turbulent channel flows. Such base flow variations are modeled as persistent white-in-time stochastic excitations that enter the linearized dynamics as multiplicative sources of uncertainty that can alter the stability of

the linearized dynamics and their receptivity to exogenous excitation. We provide verifiable conditions for mean-square stability and study the frequency response of the flow subject to additive and multiplicative sources of uncertainty using the solution to the generalized Lyapunov equation. Our approach does not rely on costly stochastic simulations or adjoint-based sensitivity analyses. We use our framework to uncover the Reynolds number scaling of critically destabilizing variance levels of the base flow uncertainty, study the reliability of numerically estimated mean velocity profiles in turbulent channel flows, and the robust performance of a typical boundary control strategy for turbulence suppression in the wake of parametric uncertainties. For small-amplitude base flow perturbations, we adopt a perturbation analysis to provide a computationally efficient method for computing the variance amplification of velocity fluctuations around the uncertain base. Moreover, we study the flow structures that are extracted from a modal decomposition of the resulting velocity covariance matrix at energetically dominant locations of wall-parallel wavenumbers. In the final part of this thesis, we use the developed input-output framework to evaluate the robust performance transverse lower-wall oscillations as a flow control strategy when oscillations are subject to imperfections in amplitude and phase. These imperfections, cause the nominally harmonic flow control strategy to resemble a random oscillatory pattern.

TABLE OF CONTENTS

| | |
|----------------------------------------------------------------------------------------------------------------|----|
| ACKNOWLEDGMENTS | v |
| ABSTRACT | vi |
| LIST OF FIGURES | x |
| CHAPTER 1 INTRODUCTION | 1 |
| CHAPTER 2 FLUCTUATIONS DYNAMICS AROUND UNCERTAIN BASE FLOW | 6 |
| CHAPTER 3 MEAN-SQUARE STABILITY AND INPUT-OUTPUT ANALYSIS . | 11 |
| 3.1 Stochastic feedback interconnection | 11 |
| 3.2 Mean-square stability conditions | 13 |
| 3.3 Frequency response of uncertain dynamics | 15 |
| CHAPTER 4 EFFECT OF BASE FLOW VARIATIONS ON TRANSITIONAL FLOWS | 18 |
| 4.1 Stability analysis | 18 |
| 4.2 Energy spectrum of velocity fluctuations | 20 |
| 4.3 Maximally affected flow structures | 24 |
| CHAPTER 5 EFFECT OF BASE FLOW VARIATIONS ON TURBULENT FLOW DYNAMICS | 32 |
| 5.1 Stability analysis | 34 |
| 5.2 Energy spectrum of velocity fluctuations | 35 |
| 5.3 Maximally affected flow structures | 37 |
| CHAPTER 6 REYNOLDS NUMBER DEPENDENCE | 41 |
| CHAPTER 7 EFFECT OF PARAMETRIC UNCERTAINTIES ON THE PERFOR- MANCE OF TRANSVERSE WALL OSCILLATIONS | 46 |
| 7.1 Dynamics of velocity fluctuations in the presence of random wall oscillations | 47 |
| 7.2 MSS conditions and Frequency response analysis | 48 |
| 7.3 MSS and variance amplification in channel ow subject to random lower-wall oscillations | 51 |
| CHAPTER 8 CONCLUSION | 55 |
| APPENDIX A OPERATORS $\bar{\mathbf{A}}$, \mathbf{A}_u , AND \mathbf{A}_w FOR LAMINAR FLOW | 58 |
| APPENDIX B PERTURBATION ANALYSIS FOR SOLVING THE GENERALIZED LYAPUNOV EQUATION | 59 |

| | |
|----------------------------------------------------------------------------------------------------------------------------------------------------------------|----|
| APPENDIX C OPERATORS $\bar{\mathbf{A}}$ AND \mathbf{A}_u FOR TURBULENT FLOW | 60 |
| APPENDIX D PROOF OF THEOREM 1 | 61 |
| APPENDIX E PROOF OF THEOREM 2 | 62 |
| APPENDIX F MEAN AND VARIANCE OF WHITE-IN-TIME STOCHASTIC UN- CERTAINTIE γ_1 AND γ_{-1} | 63 |
| APPENDIX G FUNCTIONS $W_{+1}(y)$ AND $W_{-1}(y)$ IN A SYSTEM OF DIFFEREN- TIAL EQUATIONS IN THE PRESENCE OF RANDOM WALL OSCILLATIONS | 64 |
| APPENDIX H OPERATORS \mathbf{A}_0 , \mathbf{A}_{+1} , AND \mathbf{A}_{-1} IN THE DYNAMIC MATRIX OF THE SYSTEM WITH RANDOM WALL OSCILLATIONS | 65 |
| APPENDIX I PERTURBATION ANALYSIS FOR SOLVING THE GENERALIZED LYAPUNOV EQUATION IN THE PRESENCE RANDOM WALL OSCILLATIONS | 66 |
| REFERENCES | 68 |
| BIOGRAPHICAL SKETCH | 73 |
| CURRICULUM VITAE | |

LIST OF FIGURES

| | | |
|-----|-------------------------------------------------------------------------------------------------------------------------------------------------------------------------------------------------------------------------------------------------------------------------------------------------------------------------------------------------------------------------------------------------------------------------------------------------------------------------------------------------------------------------------------------------------------------------------------------------------------------------------------------------------------------------------|----|
| 1.1 | Side view of the three-dimensional canonical flows considered in this study along with various realizations of stochastic base flow perturbations $\gamma_u(t)$ represented by the shaded area surrounding the base flow profiles. (a) Couette flow; (b) Poiseuille flow; and (c) turbulent channel flow. | 5 |
| 2.1 | (a) A shape function $f(y)$ determined using Eq. (2.7) with $\{y_1, y_2\} = \{-0.9, 0.9\}$ and $a = 200$; and (b) a two-sided shape function $f(y) = f_1(y) + f_2(y)$ in which $f_1(y)$ and $f_2(y)$ are determined using Eq. (2.7) with $\{y_1, y_2\} = \{-1, -0.95\}$ for $f_1(y)$, $\{y_1, y_2\} = \{0.95, 1\}$ for $f_2(y)$, and $a = 200$ | 10 |
| 3.1 | Linear fractional transformation of an LTI system subject to both additive and multiplicative stochastic disturbances (Eqs. (3.3)). Here, $d\mathbf{f}$ and the $d\tilde{\gamma}_i$ represent differentials of Wiener processes that model additive and multiplicative sources of stochastic uncertainty, respectively. | 13 |
| 4.1 | Stability curves for fluctuation dynamics with $\mathbf{k} = (1, 1)$ in (a) Couette flow; and (b) Poiseuille flow. The curves demonstrate the Reynolds number dependence of the maximum tolerable variance for stochastic base flow perturbations entering the dynamics through $f(y) = \bar{U}(y)/ \bar{U}(y) $ (+) or the shape functions $f(y)$ depicted in Figs. 2.1(a) (*) and 2.1(b) (o). For a given Reynolds number, the shaded areas under the curves denote the variances of stochastic base flow uncertainty that do not violate MSS ($\rho(\mathbb{L}) < 1$ with $\alpha = 1$). The triangles in the upper right corners demonstrate an R^{-1} slope. | 20 |
| 4.2 | Logarithmically scaled critical variance levels for stochastic multiplicative uncertainty $\bar{\gamma}_u$ with $\alpha = 1$ and $f(y) = \bar{U}(y)/ \bar{U}(y) $ over the horizontal wavenumber spectrum in (a) Couette flow with $R = 500$; and (b) Poiseuille flow with $R = 2000$ | 21 |
| 4.3 | Energy spectra of (a) plane Couette flow with $R = 500$ and (b) plane Poiseuille flow with $R = 2000$. Color plots show $\log_{10}(E_0(\mathbf{k}))$ | 22 |
| 4.4 | The discounted energy spectrum E_c in Couette flow with $R = 500$ and $k_x = 1$ subject to base flow perturbations with $f(y) = \bar{U}(y)/ \bar{U}(y) $ with $\sigma_u^2 = 0.43$ and $\alpha = 0.01$. Direct solution from solving Eq. (3.11)(-); and approximate solutions from perturbation analysis: $E_c = \alpha^2 E_2(\mathbf{k})$ (*) and $E_c = \alpha^2 E_2(\mathbf{k}) + \alpha^4 E_4(\mathbf{k})$ (o). | 23 |
| 4.5 | The second-order correction to the energy spectrum $E_2(\mathbf{k})$ due to multiplicative uncertainty $\bar{\gamma}_u$ in Couette flow with $R = 500$ (left); and Poiseuille flow with $R = 2000$ (right). Shape functions: (a,b) $f(y) = \bar{U}(y)/ \bar{U}(y) $; (c,d) Fig. 2.1(a); (e,f) Fig. 2.1(b). Variances σ_u^2 : (a) 4.38×10^{-3} ; (b) 6.25×10^{-4} ; (c) 0.004; (d) 6.25×10^{-4} ; (e) 0.005; (f) 0.001. Color plots show $\log_{10}(E_2(\mathbf{k}))$. The symbols (\times) and (\bullet) mark the wavenumber pairs associated with oblique waves and TS waves, respectively. | 25 |

- 4.6 The correction to the energy spectrum $E_c(\mathbf{k})$ due to multiplicative uncertainty $\bar{\gamma}_u$ with $\alpha = 0.5$ in Couette flow with $R = 500$ (left); and Poiseuille flow with $R = 2000$ (right). Shape functions: (a,b) $f(y) = \bar{U}(y)/|\bar{U}(y)|$; (c,d) Fig. 2.1(a); (e,f) Fig. 2.1(b). Variances σ_u^2 : (a) 4.38×10^{-3} ; (b) 6.25×10^{-4} ; (c) 0.004; (d) 6.25×10^{-4} ; (e) 0.005; (f) 0.001. Color plots show $\log_{10}(E_c(\mathbf{k}))$ 26
- 4.7 The relative correction to the turbulent kinetic energy $\int_{\mathbf{k}} E_c(\mathbf{k}) d\mathbf{k} / \int_{\mathbf{k}} E_0(\mathbf{k}) d\mathbf{k}$ in (a) Couette flow with $R = 500$; and (b) Poiseuille flow $R = 2000$ subject to base flow variations with amplitude α . The curves demonstrate the α dependence of the energy correction due to stochastic base flow perturbations entering the dynamics through $f(y) = \bar{U}(y)/|\bar{U}(y)|$ (+), Fig. 2.1(a) (*), and Fig. 2.1(b) (o). (a) Base flow perturbations are introduced with variances of $\sigma_u^2 = 4.38 \times 10^{-3}$ (+), 0.004 (*); and 0.005 (o) into Couette flow, and (b) $\sigma_u^2 = 6.25 \times 10^{-4}$ (+), 6.25×10^{-4} (*); and 0.001 (o) into Poiseuille flow. 27
- 4.8 Contribution of the first six eigenvalues of the velocity covariance matrix Φ of channel flow in the absence (*) and presence (o) of base flow perturbations with $f(y) = \bar{U}(y)/|\bar{U}(y)|$ and amplitude $\alpha = 1$. (a) Couette flow with $R = 500$ at $\mathbf{k} = (0.95, 2.29)$; and (b) Poiseuille flow with $R = 2000$ at $\mathbf{k} = (0.38, 3.02)$. The variance of base flow uncertainties: (a) $\sigma_u^2 = 0.50$; (b) $\sigma_u^2 = 0.21$ 27
- 4.9 Streamwise component of dominant flow structures of Couette flow with $R = 500$ and $\mathbf{k} = (0.95, 2.29)$ in the absence (first rows) and presence (second rows) of stochastic base flow perturbations with $f(y) = \bar{U}(y)/|\bar{U}(y)|$, $\alpha = 1$, and $\sigma_u^2 = 0.50$; (a) principal modes; and (b) second most energetic modes: (left) the spatial structure of the eigenmodes with high(red) and low(blue) velocity; (middle) the streamwise velocity at $z = 0$; and (right) the $y - z$ slice of streamwise velocity (color plots) and vorticity (contour lines) at the streamwise location indicated by the dashed vertical lines in the middle panel. 30
- 4.10 Streamwise component of dominant flow structures of Poiseuille flow $R = 2000$ and $\mathbf{k} = (0.38, 3.02)$ in the absence (first rows) and presence (second rows) of stochastic base flow perturbations with $f(y) = \bar{U}(y)/|\bar{U}(y)|$, $\alpha = 1$, and $\sigma_u^2 = 0.21$; (a) principal modes; and (b) second most energetic modes: (left) the spatial structure of the eigenmodes with high(red) and low(blue) velocity; (middle) the streamwise velocity at $z = 0$; and (right) the $y - z$ slice of streamwise velocity (color plots) and vorticity (contour lines) at the streamwise location indicated by the dashed vertical lines in the middle panel. 31
- 5.1 (a) Stability curves for fluctuation dynamics with $\mathbf{k} = (2.5, 7)$ in turbulent channel flow subject to stochastic base flow perturbations following $f(y) = \bar{U}(y)/|\bar{U}(y)|$ (+); or the shape functions $f(y)$ shown in Fig. 2.1(a) (*); and Fig. 2.1(b) (o). The shaded areas under the curves denote the variances of stochastic base flow uncertainty that do not violate MSS ($\rho(\mathbb{L}) < 1$ with $\alpha = 1$). The triangle in the upper right corner demonstrates an R_τ^{-1} slope. (b) Logarithmically scaled critical variance levels of stochastic multiplicative uncertainty $\bar{\gamma}_u$ with $\alpha = 1$ and $f(y) = \bar{U}(y)/|\bar{U}(y)|$ over the horizontal wavenumber spectrum of turbulent channel flow with $R_\tau = 186$ 35

| | | |
|-----|---------------------------------------------------------------------------------------------------------------------------------------------------------------------------------------------------------------------------------------------------------------------------------------------------------------------------------------------------------------------------------------------------------------------------------------------------------------------------------------------------------------------------------------------------------------------------------------------------------------------------------------------------------------------------------------------------------------------------------------------------------------|----|
| 5.2 | (a) Premultiplied energy spectrum of turbulent channel flow with $R = 186$ in the absence of stochastic base flow perturbations ($E_0(\mathbf{k})$). Correction to the premultiplied energy spectra $E_c(\mathbf{k})$ of turbulent channel flow $R = 186$ due to stochastic multiplicative uncertainty γ_u with variance $\sigma_u^2 = 0.13$ and perturbation amplitudes $\alpha = 0.05$ (second row) and $\alpha = 0.9$ (third row) that follow perturbations shapes $f(y) = \bar{U}(y)/ \bar{U}(y) $ (b, e), $f(y)$ in Fig. 2.1(a) (c, f), and $f(y)$ in Fig. 2.1(b) (d, g). | 38 |
| 5.3 | The total effect of stochastic perturbations of amplitude α on the energy spectrum of turbulent channel flow with $R_\tau = 186$. The curves demonstrate the α dependence of the energy correction due to base flow perturbations entering the dynamics through $f(y) = \bar{U}(y)/ \bar{U}(y) $ (+), or the shape functions $f(y)$ depicted in Figs. 2.1(b) (\circ) and 2.1(a) ($*$). | 39 |
| 5.4 | Contribution of the first eight eigenvalues of the velocity covariance matrix Φ of channel flow in the absence ($*$), and presence (\circ) of base flow perturbations with $f(y) = \bar{U}(y)/ \bar{U}(y) $ and amplitude $\alpha = 1$ in turbulent channel flow with $R_\tau = 186$ at $(k_x, k_z) = (1.86, 1.94)$ | 39 |
| 5.5 | The streamwise component of the dominant flow structures of turbulent channel flow with $R_\tau = 186$ and $(k_x, k_z) = (1.86, 1.94)$ in the absence and (first row) and presence (second row) of stochastic base flow perturbations of amplitude $\alpha = 1$, shape $f(y) = \bar{U}(y)/ \bar{U}(y) $, and variance $\sigma_u^2 = 0.49$. The three columns correspond to: (left) the spatial structure of the eigenmodes with red and blue colors denoting regions of high and low velocity; (middle) the streamwise velocity at $z = 0$; and (right) the $y - z$ slice of streamwise velocity (color plots) and vorticity (contour lines) at the streamwise location indicated by the dashed vertical lines in the middle panel ($x = 0.6$). | 40 |
| 6.1 | The k_z -dependence of functions (a) f , (b) h , and (c) g in Eq. (6.1) for Couette flow with $R = 500$ (—) and Poiseuille flow with $R = 2000$ (—) subject to base flow perturbations of shape $f(y) = \bar{U}(y)/ \bar{U}(y) $ of variance $\sigma_u^2 = 1.13 \times 10^5$ and $\sigma_u^2 = 3.22 \times 10^3$, respectively. The function f , which is responsible for the $O(R)$ energy amplification is the same for both channel flows. | 44 |
| 6.2 | Logarithmically scaled terms that are responsible for the $O(R^2)$ energy amplification in Eq. (6.1) ($\log_{10}(g(k_z, \sigma_u^2))$) as a function of spanwise wavenumber k_z and base flow perturbation variance σ_u^2 . Perturbations to the base flow follow $f(y) = \bar{U}(y)/ \bar{U}(y) $. (a) Couette flow with $R = 500$; and (b) Poiseuille flow with $R = 2000$ | 44 |
| 6.3 | The k_z -dependence of functions (a) f , (b) h , and (c) g in Eq. (6.1) for turbulent flow with $R = 186$ subject to base flow perturbations of shape $f(y) = \bar{U}(y)/ \bar{U}(y) $ and variance $\sigma_u^2 = 62.5$. (d) The logarithmically scaled term responsible for the $O(R^2)$ energy amplification in Eq. (6.1) ($\log_{10}(g(k_z, \sigma_u^2))$) as a function of spanwise wavenumber k_z and base flow perturbation variance σ_u^2 | 45 |

| | | |
|-----|---------------------------------------------------------------------------------------------------------------------------------------------------------------------------------------------------------------------------------------------------------------------------------------------------------------------------------------------------------------------------------------------------------------------------------------------------------------------------------------------------------------------------------------------------------------------------------------------------------------------------------------------|----|
| 7.1 | (a) Channel flow subject to transverse wall oscillations with amplitude and phase imperfections; and (b) Boundary condition on spanwise velocity due to stochastic processes $\gamma_\alpha \sim \mathcal{N}(0, 0.1)$ and $\gamma_\theta \sim \mathcal{N}(0, 1)$ (gray); see Eqs. (7.1). The amplitude and frequency of the nominal sinusoidal oscillation are given by $\alpha = 0.1$ and $\omega_t = 1$ (red). | 47 |
| 7.2 | Stability curves for the dynamics of fluctuations in a channel flow with $R = 2000$ and $\mathbf{k} = (0, 2)$ subject to random lower-wall oscillations of frequency $\omega_t = 8.8 \times 10^{-3}$ (*) and $\omega_t = 5 \times 10^{-4}$ (—) with nominal oscillation amplitudes (a) $\alpha = 0.01$; and (b) $\alpha = 0.1$. The shaded areas under the curves correspond to variances of γ_α and γ_θ that do not violate MSS. | 52 |
| 7.3 | (a) Energy spectrum ($E_0(\mathbf{k})$) of the uncontrolled Poiseuille flow with $R = 2000$. Energy spectrum ($E(\mathbf{k})$) due to lower-wall oscillations with $\omega_t = 8.8 \times 10^{-3}$ up to the level of α^2 : (b) in the absence of zero-mean parametric uncertainty; and (c), (d), (e) in the presence of zero-mean parametric uncertainty with variances (c) $\sigma_\alpha^2 = 38$ and $\sigma_\theta^2 = 0.69$; (d) $\gamma_\alpha = 0$ and $\sigma_\theta^2 = 0.69$; (e) $\sigma_\alpha^2 = 38$ and $\gamma_\theta = 0$ of Poiseuille flow with $R = 2000$. The plots are given in log-log scale. | 54 |

CHAPTER 1

INTRODUCTION

The linearized Navier-Stokes (NS) equations have been used to capture the early stages of transition and identify key mechanisms for subcritical transition in wall-bounded shear flows. The non-normality of the linearized dynamical generator induces interactions of the exponentially decaying normal modes (Trefethen et al., 1993; Schmid and Henningson, 2001) even in the absence of transition, and results in the high sensitivity of velocity fluctuations to different sources of perturbation. This feature has played a critical role in explaining the large transient growth of velocity fluctuations (Gustavsson, 1991; Butler and Farrell, 1992; Reddy and Henningson, 1993; Henningson and Reddy, 1994; Schmid and Henningson, 1994) and the amplification of deterministic and stochastic disturbances in transitional and turbulent wall-bounded flows (Trefethen et al., 1993; Farrell and Ioannou, 1993, 1998; Bamieh and Dahleh, 2001; Jovanovic and Bamieh, 2005; Hwang and Cossu, 2010a,b; McKeon and Sharma, 2010; Ran et al., 2019). The success of this approach has also paved the way for the model-based design of active and passive flow control strategies for suppressing turbulence or reducing skin-friction drag (Kim and Bewley, 2007; Jovanovic, 2008; Moarref and Jovanovic, 2010, 2012; Luhar et al., 2014; Ran et al., 2021). These studies have used additive stochastic excitation to model the effect of background disturbances and exogenous perturbations, or model the uncertainty caused by excluding the nonlinear terms in the NS equations. Despite most studies being focused on stochastic excitations to be white-in-time, efforts have also been made to shape the spectra of colored-in-time stochastic forcing to match the second-order statistics of turbulent flows (Zare et al., 2016, 2017; Morra et al., 2019; Towne et al., 2020; Zare et al., 2017, 2020), which highlights the dynamical significance of such additive stochastic excitations in augmenting the linearized dynamics (Zare et al., 2017). An important, but rather less studied aspect of the linearized NS equations, however, arises

from the uncertainty surrounding the choice of a base flow state and its implications for stability analysis, turbulence modeling, and the performance of model-based flow control.

Depending on the flow configuration and its characteristic regime, a base flow profile can either be obtained as the solution to the NS equations in steady state, or as a long-time averaged mean of a simulation-based flow field or experimental dataset. Due to insufficient data or imprecise measurements can cause the time-averaged mean to be poorly approximated, resulting in uncertainties that prevail over the statistical averaging process (small data issues). For example, experimental constraints may confine reliable measurement collection and subsequent data acquisition procedures to certain parts of the flow domain, and in numerical simulations, segments of the computational domain may be poorly resolved. Furthermore, analytical or numerical approximations may have been made outside their range of validity implying a degree of uncertainty in the expressions for base flow profiles. Therefore, development of techniques that account for various sources of uncertainty and evaluate the validity and robustness of linearized models around uncertain base flow profiles plays an important role in accounting for these uncertainties in flow dynamics.

For examining the sensitivity of the eigenvalues of the Orr–Sommerfeld operator to deterministic variations in the base flow, previous studies have used an adjoint-based variational procedure to identify worst-case perturbations with the most destabilizing effect on the eigenspectrum (Bottaro et al., 2003). Similar tools were later used in a locally temporal framework for identifying the optimal modification to the base flow for stabilizing a bluff-body wake (Hwang and Choi, 2006) and extended to global stability analysis (Marquet et al., 2008; Pralits et al., 2010). While it has been shown that minute perturbations of the dynamic generator can cause significant displacement of eigenvalues (Reddy et al., 1993; Schmid et al., 1993; Trefethen and Embree, 2005), it is generally accepted that the disturbance behavior of the linearized NS equations would be robust. Furthermore in (Brandt et al., 2011), an analytical expression was found for the gradient of singular values of the

resolvent operator with respect to base flow modifications thereby accounting for variations in the non-modal behavior of wall-bounded shear flows. Besides adjoint-based methods for analyzing the sensitivity to deterministic modifications, there has also been efforts in quantifying the effect of random spatial base flow variations using stochastic spectral projection based on generalized polynomial chaos theory (Ko et al., 2011).

Additive sources of uncertainty in the base flow enter the linearized dynamics multiplicatively and in a structured manner. The structured singular value provides a robust stability theory for the uncertain dynamics in the presence of deterministic and set-valued uncertainties (Skogestad and Postlethwaite, 2007). However, implementation deficiencies often results in unpredictable time-varying parametric variations. While this approach is based on a worst-case analysis and may not provide a realistic model for experimental/numerical imperfections, the dynamical equations for the second moments of stochastically perturbed linear systems can be used determine the effect of perturbations on optimal finite-time energy growth (Farrell and Ioannou, 2002). Application of similar analysis techniques to stochastically perturbed Poiseuille flow uncovers the effect of multiplicative uncertainty on optimal energy growth as well as the robust amplification of streaks (Schmid, 2007). As highlighted in these studies, persistent multiplicative uncertainty increases the sensitivity of non-normal linear dynamical systems by influencing their asymptotic and transient mean-square response. In contrast to its additive counterpart, however, white-in-time multiplicative uncertainty can compromise the mean-square stability properties of linear systems. Mean-square stability (MSS) is a strong form of stability that implies stability of the mean and convergence of all trajectories of the stochastic dynamical system (in the absence of exogenous excitation) to zero with probability one (Kushner, 1967; Willems, 1973).

In this thesis, we have revisited the problem of analyzing internal stochastic uncertainties by modeling structured perturbations to the base flow as white-in-time stochastic processes. The dynamics of velocity fluctuations around the uncertain base state are governed by a

set of stochastic differential equations (SDEs) and we provide an input-output treatment by rewriting the SDEs as a feedback interconnection of the linearized dynamics and structured stochastic uncertainties. This allows us to separate the nominal (known) dynamics from the sources of uncertainty and facilitates both stability and receptivity analyses of the fluctuation dynamics in the presence of persistent additive and multiplicative stochastic excitation. Following recent developments of (Filo and Bamieh, 2018), we provide specialized conditions for the MSS of the uncertain dynamics. Furthermore, we analyze the energy spectrum of the linearized NS equations subject to additive and multiplicative sources of excitation. To this end, we compute the second-order statistics of the velocity field from the solution to a generalized Lyapunov equation. We demonstrate the utility of our approach by studying the stability and receptivity of the three-dimensional channel flow around canonical Couette and Poiseuille profiles as well as a turbulent mean velocity profile resulting from direct numerical simulations (DNS), all of which are contaminated with persistent stochastic perturbations; see Fig. 1.1 for an illustration. We also uncover the Reynolds number scaling of the critical variance of stochastic base flow uncertainty that guarantees MSS and identify length scales that are most influenced by such perturbations. In the final chapter, we use our input-output framework to study the effect of random lower-wall oscillations in a channel flow with $Re = 2000$. The random oscillations are due to stochastic parametric uncertainties in the amplitude and phase of nominally harmonic wall oscillations.

The rest of the presentation is organized as follows. In chapter 2, we describe our model of stochastic base flow perturbation, introduce the stochastically forced linearized NS equations around the uncertain base flow, and demonstrate how base flow perturbations enter the dynamics as multiplicative sources of uncertainty. In chapter 3, we rewrite the linearized dynamics as a feedback interconnection between nominal dynamics and sources of stochastic uncertainty. We then use this input-output representation to provide MSS conditions for our model, characterize its frequency response, and describe the generalized Lyapunov

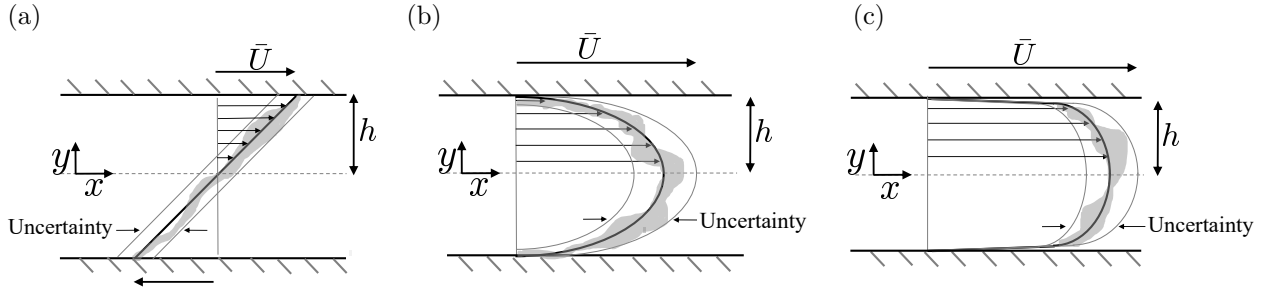


Figure 1.1. Side view of the three-dimensional canonical flows considered in this study along with various realizations of stochastic base flow perturbations $\gamma_u(t)$ represented by the shaded area surrounding the base flow profiles. (a) Couette flow; (b) Poiseuille flow; and (c) turbulent channel flow.

equation that we use to compute the second-order statistics and energy spectrum of velocity fluctuations. In chapter 4, we examine the MSS and energy amplification of velocity fluctuations around Couette and Poiseuille profiles, and study eigenvalue contributions and flow structures corresponding to principal modes that has the maximum energy contributions. In chapter 5, we conduct a similar analysis for the linearized NS equations around the DNS-based mean velocity profiles of turbulent channel flow at various Reynolds numbers. We then provide a Reynolds number dependence on the energy amplification of streamwise constant parallel channel flows in chapter 6. In chapter 7, we examine the MSS of channel flow over random wall oscillations and discuss the influence of parametric uncertainty on the energy of velocity fluctuations. We provide concluding remarks in chapter 8. The material

CHAPTER 2

FLUCTUATIONS DYNAMICS AROUND UNCERTAIN BASE FLOW

The dynamics of incompressible Newtonian fluids is governed by the NS equations,

$$\begin{aligned}\tilde{\mathbf{u}}_t &= -(\tilde{\mathbf{u}} \cdot \nabla) \tilde{\mathbf{u}} - \nabla \tilde{P} + \frac{1}{R} \Delta \tilde{\mathbf{u}} \\ 0 &= \nabla \cdot \tilde{\mathbf{u}}\end{aligned}\tag{2.1}$$

where $\tilde{\mathbf{u}}$ is the velocity vector, \tilde{P} is the pressure, ∇ is the gradient, $\Delta = \nabla \cdot \nabla$ is the Laplacian, and t is time. Here, the Reynolds number R is defined in terms of appropriate length and velocity scales, e.g., for a laminar channel flow configuration, $R = \bar{U}h/\nu$, where \bar{U} is the maximum nominal velocity, h is the channel half-height, and ν denotes the kinematic viscosity. Linearization of the NS equations around an arbitrary, parallel base flow $\mathbf{u} = [U(y) \ 0 \ W(y)]^T$ and pressure P yields the equations that govern the dynamics of velocity, \mathbf{v} , and pressure, p , fluctuations,

$$\begin{aligned}\mathbf{v}_t &= -(\nabla \cdot \mathbf{u}) \mathbf{v} - (\nabla \cdot \mathbf{v}) \mathbf{u} - \nabla p + \frac{1}{R} \Delta \mathbf{v} + \mathbf{f} \\ 0 &= \nabla \cdot \mathbf{v}.\end{aligned}\tag{2.2}$$

Here, $\mathbf{v} = [u \ v \ w]^T$, with u , v , and w representing the fluctuating components in the streamwise, x , wall-normal, y , and spanwise, z directions, and \mathbf{f} denotes a three-dimensional zero-mean white-in-time additive stochastic forcing.

We assume the base flow \mathbf{u} to be contaminated with an additive source of uncertainty, i.e.,

$$\mathbf{u}(y, t) = \bar{\mathbf{u}}(y) + \gamma(y, t).\tag{2.3}$$

Here, $\bar{\mathbf{u}} = [\bar{U}(y) \ 0 \ \bar{W}(y)]^T$ is the nominal base flow in the absence of uncertainty and γ is a zero-mean white-in-time stochastic process that can enter both streamwise and spanwise components of $\bar{\mathbf{u}}$, i.e., $\gamma = [\gamma_u(y, t) \ 0 \ \gamma_w(y, t)]^T$. The uncertain base flow \mathbf{u} enters the

linearized Eqs. (2.2) as a coefficient that multiplies the vector of velocity fluctuations \mathbf{v} . While \mathbf{u} includes the sources of uncertainty γ , it remains constant in x and z . Elimination of pressure and application of the Fourier transform in the spatially invariant wall-parallel directions brings Eqs. (2.2) into the evolution form

$$\begin{aligned}\varphi_t(y, \mathbf{k}, t) &= [\mathbf{A}(\mathbf{k}, t) \varphi(\cdot, \mathbf{k}, t)](y) + [\mathbf{B}(\mathbf{k}) \mathbf{f}(\cdot, \mathbf{k}, t)](y) \\ \mathbf{v}(y, \mathbf{k}, t) &= [\mathbf{C}(\mathbf{k}) \varphi(\cdot, \mathbf{k}, t)](y)\end{aligned}\tag{2.4}$$

where the state variable $\varphi = [v \ \eta]^T$ contains the wall-normal velocity v and vorticity $\eta = \partial_z u - \partial_x w$, and $\mathbf{k} = [k_x \ k_z]^T$ is the vector of streamwise and spanwise wavenumbers. These SDEs involve multiplicative sources of stochastic uncertainty γ_u and γ_w in addition to the additive source of stochastic uncertainty \mathbf{f} . In (2.4), operators \mathbf{A} , \mathbf{B} , and \mathbf{C} are given by

$$\mathbf{A}(\mathbf{k}, t) := \begin{bmatrix} \mathbf{A}_{11} & 0 \\ \mathbf{A}_{21} & \mathbf{A}_{22} \end{bmatrix}\tag{2.5}$$

$$\begin{aligned}\mathbf{A}_{11}(\mathbf{k}, t) &:= \Delta^{-1} \left(\frac{1}{R} \Delta^2 + ik_x (\bar{U}''(y) + \gamma_u''(y, t) - (\bar{U}(y) + \gamma_u(y, t)) \Delta) + \right. \\ &\quad \left. ik_z (\bar{W}''(y) + \gamma_w''(y, t) - (\bar{W}(y) + \gamma_w(y, t)) \Delta) \right)\end{aligned}$$

$$\mathbf{A}_{21}(\mathbf{k}, t) := -ik_z (\bar{U}'(y) + \gamma_u'(y, t)) + ik_x (\bar{W}'(y) + \gamma_w'(y, t))$$

$$\mathbf{A}_{22}(\mathbf{k}, t) := \frac{1}{R} \Delta - ik_x (\bar{U}(y) + \gamma_u(y, t)) - ik_z (\bar{W}(y) + \gamma_w(y, t))$$

$$\mathbf{B}(\mathbf{k}) := \begin{bmatrix} -ik_x \Delta^{-1} \partial_y & -k^2 \Delta^{-1} & -ik_z \Delta^{-1} \partial_y \\ ik_z & 0 & -ik_x \end{bmatrix},\tag{2.6}$$

$$\mathbf{C}(\mathbf{k}) := \begin{bmatrix} \mathbf{C}_u \\ \mathbf{C}_v \\ \mathbf{C}_w \end{bmatrix} = \frac{1}{k^2} \begin{bmatrix} ik_x \partial_y & -ik_z \\ k^2 & 0 \\ ik_z \partial_y & ik_x \end{bmatrix}$$

where prime denotes differentiation with respect to the wall-normal coordinate, i is the imaginary unit, $k^2 = k_x^2 + k_z^2$, $\Delta = \partial_y^2 - k^2$ is the Laplacian, $\Delta^2 = \partial_y^4 - 2k^2\partial_y^2 + k^4$, and $v(\pm 1, \mathbf{k}, t) = v_y(\pm 1, \mathbf{k}, t) = \eta(\pm 1, \mathbf{k}, t) = 0$, which can be derived from the original no-slip and no-penetration boundary conditions on u , v , and w .

We confine the class of stochastic base flow perturbations to the form $\gamma(y, t) = \alpha \bar{\gamma}(t)f(y)$, in which α is the constant amplitude, $\bar{\gamma}(t)$ is a zero-mean stochastic parameter of unit amplitude, and $f(y)$ is a smooth filter function that determines the wall-normal region of influence and is defined as

$$f(y) := \frac{1}{\pi} [\arctan(a(y - y_1)) - \arctan(a(y - y_2))]. \quad (2.7)$$

Here, y_1 and y_2 determine the wall-normal extent of $f(y)$ and a specifies the roll-off rate. In chapters. 4 and 5, we study the influence of stochastic base flow perturbations that follow the shape of the associated nominal base flows ($f(y) = \bar{U}(y)/|\bar{U}(y)|$), in addition to the two shape functions shown in Fig. 2.1. While the shape function in Fig. 2.1(a) does not restrict the wall-normal extent of the perturbations (besides a roll-off at the wall in accordance with the boundary conditions), Fig. 2.1(b) represents an extreme case corresponding to base flow perturbations that may result from active/passive boundary actuation (e.g., blowing and suction or surface roughness). Beyond application specificities, these extreme cases allow us to study the dependence of our results on the wall-normal extent of base flow perturbations.

Based on the class of stochastic perturbations $\gamma(y, t)$ considered in this thesis, the operator-valued matrix \mathbf{A} in evolution model (2.4) can be decomposed into nominal and perturbed components as

$$\mathbf{A}(\mathbf{k}, t) = \bar{\mathbf{A}}(\mathbf{k}) + \alpha (\bar{\gamma}_u(t) \mathbf{A}_u(\mathbf{k}) + \bar{\gamma}_w(t) \mathbf{A}_w(\mathbf{k})) \quad (2.8)$$

where expressions for $\bar{\mathbf{A}}$, \mathbf{A}_u , and \mathbf{A}_w are given in Appendix A. The nominal base flow profile $\bar{\mathbf{u}}(y)$, and shape functions $f_u(y)$ and $f_w(y)$ enter operators $\bar{\mathbf{A}}$, \mathbf{A}_u , and \mathbf{A}_w as deterministic

parameters, respectively. Note that while we have assumed the streamwise and spanwise components of the base flow uncertainty $\gamma(y, t)$ to be of equal amplitude, all mathematical developments can be easily extended to scenarios where the streamwise and spanwise components have different amplitudes.

In this study, we use a pseudospectral scheme with N Chebyshev collocation points in the wall-normal direction (Weideman and Reddy, 2000) to discretize the operators in the linearized equations (2.4). In addition, we employ a change of variables to obtain a state-space representation in which the kinetic energy is determined by the Euclidean norm of the state vector (Zare et al., 2017, Appendix A). This yields the state-space model

$$\begin{aligned}\dot{\boldsymbol{\psi}}(\mathbf{k}, t) &= A(\mathbf{k}, t) \boldsymbol{\psi}(\mathbf{k}, t) + B(\mathbf{k}) \mathbf{f}(\mathbf{k}, t) \\ \mathbf{v}(\mathbf{k}, t) &= C(\mathbf{k}) \boldsymbol{\psi}(\mathbf{k}, t)\end{aligned}\tag{2.9}$$

where vectors $\boldsymbol{\psi}$ and \mathbf{v} are vectors with complex-valued entries and $2N$ and $3N$ components, respectively, and matrices A , B , and C are discretized versions of the corresponding operators that incorporate the aforementioned change of coordinates. We next provide an input-output reformulation of SDE (2.9) to analyze the influence of stochastic sources of uncertainty on the mean-square asymptotic stability and second-order statistics of velocity fluctuations.

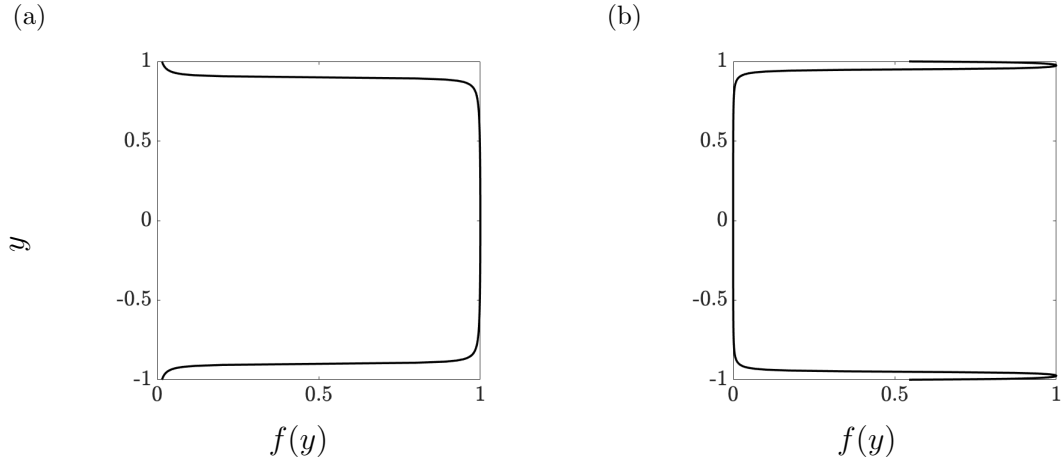


Figure 2.1. (a) A shape function $f(y)$ determined using Eq. (2.7) with $\{y_1, y_2\} = \{-0.9, 0.9\}$ and $a = 200$; and (b) a two-sided shape function $f(y) = f_1(y) + f_2(y)$ in which $f_1(y)$ and $f_2(y)$ are determined using Eq. (2.7) with $\{y_1, y_2\} = \{-1, -0.95\}$ for $f_1(y)$, $\{y_1, y_2\} = \{0.95, 1\}$ for $f_2(y)$, and $a = 200$.

CHAPTER 3

MEAN-SQUARE STABILITY AND INPUT-OUTPUT ANALYSIS

The evolution of $\boldsymbol{\psi}$ in SDE (2.9) is affected by the presence of both stochastic base flow perturbations $\gamma(y, t)$ and additive forcing $\mathbf{f}(t)$. While there is no ambiguity in the treatment of additive noise in continuous-time systems, multiplicative noise is not generally well-defined and its treatment calls for the adoption of a suitable stochastic calculus (e.g., Itô (Ito, 1979) or Stratonovich (Stratonovich, 1966)). In this chapter, we provide an appropriate interpretation for the multiplicative uncertainty, extract these sources using a linear fractional transformation, and establish an input-output relation between stochastic sources and the output velocity fluctuations of system (2.9). Building on this representation, we examine conditions for MSS and analyze the frequency response of the system in the presence of multiplicative stochastic uncertainty.

3.1 Stochastic feedback interconnection

In input-output form, SDE (2.9) can be rewritten as

$$\begin{bmatrix} \mathbf{v} \\ \mathbf{z} \end{bmatrix} = \mathcal{M} \begin{bmatrix} \mathbf{f} \\ \mathbf{r} \end{bmatrix} \Leftrightarrow \begin{bmatrix} \mathbf{v}(\mathbf{k}, t) \\ \mathbf{z}(\mathbf{k}, t) \end{bmatrix} = \int_0^t M(\mathbf{k}, t - \tau) \begin{bmatrix} \mathbf{f}(\mathbf{k}, \tau) \\ \mathbf{r}(\mathbf{k}, \tau) \end{bmatrix} d\tau$$

$$\mathbf{r}(\mathbf{k}, t) = \alpha \mathcal{D}(\bar{\gamma}(t)) \mathbf{z}(\mathbf{k}, t) \tag{3.1}$$

which extracts the role of multiplicative uncertainties by rearranging the dynamics as a feedback connection between the nominal (known) dynamics (captured by the impulse response operator \mathcal{M}) and the structured uncertainty $\mathcal{D}(\bar{\gamma}(t)) := \text{diag}\{\bar{\gamma}_u(t)I, \bar{\gamma}_w(t)I\}$. In Eqs. (3.1), M denotes the finite-dimensional approximation to the impulse response operator \mathcal{M} , \mathbf{v} is the output velocity vector (cf. Eqs. (2.9)), and \mathbf{z} is computed from the state $\boldsymbol{\psi}$. Moreover,

the exogenous stochastic input \mathbf{f} , the uncertain feedback signal \mathbf{r} , and the sources of uncertainty $\tilde{\gamma}_u$ and $\tilde{\gamma}_w$ are white processes that are all defined as derivatives of Wiener processes (or Brownian motion) (Øksendal, 2003), i.e.,

$$\tilde{\gamma}_u(t) := \frac{d\tilde{\gamma}_u(t)}{dt}; \quad \tilde{\gamma}_w(t) := \frac{d\tilde{\gamma}_w(t)}{dt}; \quad \mathbf{f}(\mathbf{k}, t) := \frac{d\tilde{\mathbf{f}}(\mathbf{k}, t)}{dt}; \quad \mathbf{r}(\mathbf{k}, t) := \frac{d\tilde{\mathbf{r}}(\mathbf{k}, t)}{dt}.$$

Here, $\tilde{\gamma}_i$ are zero-mean Wiener processes with variance σ_i^2 and $\tilde{\mathbf{f}}$ is a zero-mean vector-valued Wiener process with instantaneous covariance

$$\langle \tilde{\mathbf{f}}(\mathbf{k}, t) \tilde{\mathbf{f}}^*(\mathbf{k}, t) \rangle = \Omega(\mathbf{k}) t$$

in which $\Omega(\mathbf{k}) = \Omega^*(\mathbf{k}) \succeq 0$ is the spatial covariance matrix. We assume that $\tilde{\gamma}_i$ and $\tilde{\mathbf{f}}$ are uncorrelated at all times, adopt the Itô interpretation, and assume that \mathbf{r} has temporally independent increments, i.e., its differentials $(d\mathbf{r}(\mathbf{k}, t_1), d\mathbf{r}(\mathbf{k}, t_2))$ are independent when $t_1 \neq t_2$. Given this mathematical interpretation, the differential form of Eqs. (3.1) is given by

$$\begin{bmatrix} \mathbf{v} \\ \mathbf{z} \end{bmatrix} = \mathcal{M} \begin{bmatrix} d\tilde{\mathbf{f}} \\ d\tilde{\mathbf{r}} \end{bmatrix} \Leftrightarrow \begin{bmatrix} \mathbf{v}(\mathbf{k}, t) \\ \mathbf{z}(\mathbf{k}, t) \end{bmatrix} = \int_0^t M(\mathbf{k}, t - \tau) \begin{bmatrix} d\tilde{\mathbf{f}}(\mathbf{k}, \tau) \\ d\tilde{\mathbf{r}}(\mathbf{k}, \tau) \end{bmatrix}$$

$$d\tilde{\mathbf{r}}(\mathbf{k}, t) = \alpha \mathcal{D}(d\tilde{\gamma}(t)) \mathbf{z}(\mathbf{k}, t) \quad (3.2)$$

and is described by the block diagram in Fig. 3.1. A corresponding state-space model is given by

$$\mathcal{M} : \begin{cases} d\boldsymbol{\psi}(\mathbf{k}, t) = \bar{A}(\mathbf{k}) \boldsymbol{\psi}(\mathbf{k}, t) dt + B_0(\mathbf{k}) d\tilde{\mathbf{r}}(\mathbf{k}, t) + B(\mathbf{k}) d\tilde{\mathbf{f}}(\mathbf{k}, t) \\ \mathbf{z}(\mathbf{k}, t) = C_0(\mathbf{k}) \boldsymbol{\psi}(\mathbf{k}, t) \\ \mathbf{v}(\mathbf{k}, t) = C(\mathbf{k}) \boldsymbol{\psi}(\mathbf{k}, t) \end{cases}$$

$$d\tilde{\mathbf{r}}(\mathbf{k}, t) = \alpha \mathcal{D}(d\tilde{\gamma}(t)) \mathbf{z}(\mathbf{k}, t) \quad (3.3)$$

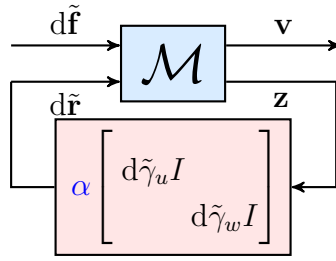


Figure 3.1. Linear fractional transformation of an LTI system subject to both additive and multiplicative stochastic disturbances (Eqs. (3.3)). Here, $d\tilde{\mathbf{f}}$ and the $d\tilde{\gamma}_i$ represent differentials of Wiener processes that model additive and multiplicative sources of stochastic uncertainty, respectively.

with

$$B_0(\mathbf{k}) := \begin{bmatrix} I & I \end{bmatrix}, \quad C_0(\mathbf{k}) := \begin{bmatrix} A_u(\mathbf{k}) \\ A_w(\mathbf{k}) \end{bmatrix}. \quad (3.4)$$

Here, $\boldsymbol{\psi}$, \mathbf{z} , and \mathbf{v} are complex-valued vectors of appropriate dimension, B and C are finite-dimensional approximations of the input and output operators in (2.9), and \bar{A} , A_u and A_w are finite-dimensional approximations of the nominal dynamics and their perturbations in (2.8).

3.2 Mean-square stability conditions

For the causal LTI system (3.3), MSS certifies that for all differential inputs, $[d\tilde{\mathbf{f}} \ d\tilde{\mathbf{r}}]^T$, with independent increments and uniformly bounded variances, the output process

$$\begin{bmatrix} \mathbf{v} \\ \mathbf{z} \end{bmatrix} = \underbrace{\begin{bmatrix} \mathcal{M}_{11} & \mathcal{M}_{12} \\ \mathcal{M}_{21} & \mathcal{M}_{22} \end{bmatrix}}_{\mathcal{M}} \begin{bmatrix} d\tilde{\mathbf{f}} \\ d\tilde{\mathbf{r}} \end{bmatrix}$$

has a uniformly bounded variance; see, e.g., (Samuels, 1959). Following (Filo and Bamieh, 2020, Theorem 3.2), the necessary and sufficient conditions for MSS can be generalized for the continuous-time scenario, i.e., the output \mathbf{v} in (3.3) has a finite covariance if and only if the feedback subsystem $(\mathcal{M}_{22}, \Gamma)$ is MSS. Based on this, the exact necessary and sufficient

conditions for the MSS of (3.3) are: (i) \bar{A} is Hurwitz; and (ii) the spectral radius of the loop gain operator

$$\mathbb{L}(\mathbf{R}) := \Gamma \circ \left(\int_0^\infty M_{22}(\tau) \mathbf{R} M_{22}^*(\tau) d\tau \right) \quad (3.5)$$

is strictly less than $1/\alpha^2$, i.e., $\rho(\mathbb{L}) < 1/\alpha^2$. Here, \circ is the Hadamard product, M_{22} is the impulse response of the subsystem $\mathcal{M}_{22} : d\tilde{\mathbf{r}} \rightarrow \mathbf{z}$, which is given by

$$M_{22}(\mathbf{k}, t) = C_0(\mathbf{k}) e^{\bar{A}(\mathbf{k}, t)t} B_0(\mathbf{k})$$

and $*$ denotes complex-conjugate-transpose. The matrix Γ denotes the mutual correlation of the sources of uncertainties $\tilde{\gamma}_i$, i.e., $\Gamma := \langle \tilde{\gamma}_i(t) \tilde{\gamma}_j^*(t) \rangle$. For example, for mutually independent multiplicative uncertainties in the streamwise and spanwise directions that are spatially uncorrelated, $\Gamma = \text{diag}\{\sigma_u^2 I, \sigma_w^2 I\}$, where σ_u^2 and σ_w^2 are variances of $\bar{\gamma}_u$ and $\bar{\gamma}_w$, respectively. In this study, we consider $\bar{\gamma}_u$ and $\bar{\gamma}_w$ to be mutually independent, but repeated throughout the spatial domain, i.e., $\Gamma = \text{diag}\{\sigma_u^2 \mathbf{1}\mathbf{1}^T, \sigma_w^2 \mathbf{1}\mathbf{1}^T\}$, where $\mathbf{1}$ represents the vector of $2N$ ones. As explained in chapter 2, the wall-normal support of each multiplicative uncertainty $\bar{\gamma}_i$ will be captured by its associated shape function $f_i(y)$ within operators A_i in Eq. (3.4).

Remark 1. *We note that a similar condition for global mean-square asymptotic stability was proposed in (Buckwar and Kelly, 2014). This condition was based on the stability of the differential generalized Lyapunov equation and amounts to the eigenvalue stability of the mean-square stability matrix, which takes a similar form as the loop gain operator $\mathbb{L}(\cdot)$. The differential generalized Lyapunov equation governs the evolution of the state covariance matrix X . In chapter 3.3, we use the steady-state solution of this equation to compute the second-order statistics and energy spectrum of velocity fluctuations in the presence of both additive and multiplicative stochastic excitation.*

The loop gain operator propagates the steady-state covariance of $d\tilde{\mathbf{r}}$ denoted by \mathbf{R} through the feedback configuration in Fig. 3.1. Equivalently, we have

$$\mathbb{L}(\mathbf{R}) = \Gamma \circ (C_0 X C_0^*)$$

where X is the solution to the algebraic Lyapunov equation

$$\bar{A} X + X \bar{A}^* = -B_0 \mathbf{R} B_0^*.$$

In practice, the spectral radius of \mathbb{L} can be numerically computed using the power iteration algorithm; see, e.g., (Filo and Bamieh, 2020, Section VI.A). Starting from an initial $\mathbf{R}_0 \succeq 0$ an estimate for the spectral radius is updated via a sequence of steps:

$$\begin{aligned} \bar{A} X_{k+1} + X_{k+1} \bar{A}^* &= -B_0 \mathbf{R}_k B_0^* \\ \mathbf{R}_{k+1} &:= \frac{1}{\|\mathbf{R}_k\|_F} (\Gamma \circ (C_0 X_{k+1} C_0^*)) \\ \rho_{k+1} &:= \langle \mathbf{R}_k, \mathbf{R}_{k+1} \rangle \end{aligned}$$

until the residual $(\mathbf{R}_{k+1} - \rho_{k+1} \mathbf{R}_k) / \|\mathbf{R}_{k+1}\|_F$ is smaller than a desirable tolerance.

3.3 Frequency response of uncertain dynamics

We build on the input-output representation provided in chapter 3.2 and characterize the frequency response of the system subject to both additive and multiplicative sources of uncertainty. We show that the second-order statistics of the uncertain system and the energy spectrum of velocity fluctuations can be obtained from the solution of a generalized Lyapunov equation.

The impulse response M in (3.2) corresponding to the state-space representation (3.3) takes the form

$$M(\mathbf{k}, t) := \begin{bmatrix} C(\mathbf{k}) \\ C_0(\mathbf{k}) \end{bmatrix} e^{\bar{A}(\mathbf{k}, t)t} \begin{bmatrix} B(\mathbf{k}) & B_0(\mathbf{k}) \end{bmatrix}$$

When \mathbf{f} , $\bar{\gamma}_u$, and $\bar{\gamma}_w$ are zero-mean white-in-time processes with covariance matrix Ω , and variances σ_u^2 and σ_w^2 , the steady-state covariance of the state,

$$X(\mathbf{k}) = \lim_{t \rightarrow \infty} \langle \boldsymbol{\psi}(\mathbf{k}, t) \boldsymbol{\psi}^*(\mathbf{k}, t) \rangle \quad (3.6)$$

can be determined as the solution to the generalized Lyapunov equation

$$\bar{A}X + X\bar{A}^* + \alpha^2 B_0 (\Gamma \circ (C_0 X C_0^*)) B_0^* = -B \Omega B^* \quad (3.7)$$

which is parameterized over wavenumber pairs \mathbf{k} . The generalized Lyapunov equation relates the statistics of white-in-time forcing \mathbf{f} and multiplicative sources of excitation $\alpha \bar{\gamma}_u$ and $\alpha \bar{\gamma}_w$ with wall-normal support $f_u(y)$ and $f_w(y)$ to the steady-state covariance X via system matrices \bar{A} and B and perturbation matrices A_u and A_w . It can also be used to compute the energy spectrum of velocity fluctuations \mathbf{v} ,

$$E(\mathbf{k}) = \text{trace}(\Phi(\mathbf{k})) = \text{trace}(C(\mathbf{k})X(\mathbf{k})C^*(\mathbf{k})) \quad (3.8)$$

where Φ is the covariance matrix of \mathbf{v} . We can then capture the influence of multiplicative uncertainty on the energy spectrum using the discounted spectrum

$$E_c(\mathbf{k}) = E(\mathbf{k}) - E_0(\mathbf{k}) \quad (3.9)$$

where E_0 denotes the nominal energy spectrum in the absence of uncertainties $\bar{\gamma}_u$ and $\bar{\gamma}_w$.

Following (3.4) and the assumption of repeated base flow perturbations, which yield $\Gamma = \text{diag}\{\sigma_u^2 \mathbf{1}\mathbf{1}^T, \sigma_w^2 \mathbf{1}\mathbf{1}^T\}$, Eq. (3.7) can be expanded to reflect contributions from uncertainties affecting the streamwise and spanwise components of the base flow as

$$\bar{A}X + X\bar{A}^* + \alpha^2 (\sigma_u^2 (A_u X A_u^*) + \sigma_w^2 (A_w X A_w^*)) = -B \Omega B^* \quad (3.10)$$

A direct approach to solving (3.10) as a linear system of equations yields

$$(I \otimes \bar{A} + \bar{A} \otimes I + \alpha^2 (\sigma_u^2 (A_u \otimes A_u) + \sigma_w^2 (A_w \otimes A_w))) \text{vec}(X) = -\text{vec}(B \Omega B^*) \quad (3.11)$$

where \otimes is the Kronecker product and $\text{vec}(\cdot)$ denotes vectorization. However, in the absence of sparse matrix structures, solving for X can be challenging even for medium-size problems. Other existing methods for solving (3.10) explore solutions to surrogate equations and utilize

iterative methods to improve computational complexity (Benner, 2004; Benner et al., 2008; Damm, 2008; Benner and Damm, 2011). In what follows, we consider small-amplitude perturbations ($\alpha \ll 1$) and pursue an alternative approach by utilizing a perturbation analysis to achieve a computationally efficient way of obtaining the energy spectrum. As shown in Appendix B, this approach allows us to compute the second-order statistics of the uncertain model by solving a sequence of standard algebraic Lyapunov equations instead of the generalized Lyapunov equation (3.10). In addition to the computational benefit, the choice of small perturbation amplitude is motivated by the desire to account for uncertainties arising from measurement imperfections, small-data issues in the statistical averaging process, or the effect of active/passive boundary actuation strategies that influence the base flow. Based on this, up to a second order in the perturbation amplitude α , the state covariance X in (3.6) is given by

$$X(\mathbf{k}) = X_0(\mathbf{k}) + \alpha^2 X_2(\mathbf{k}) + O(\alpha^4) \quad (3.12)$$

where X_0 and X_2 are obtained from a set of decoupled Lyapunov equations; see Appendix B for details. Note that X_0 represents the steady-state covariance of $\boldsymbol{\psi}$, i.e., the state of the nominal dynamics in the absence of base flow perturbations, and X_2 represents the second-order correction induced by the random base flow uncertainty. The energy spectrum of velocity fluctuations \mathbf{v} (Eq. (3.8)) follows a similar perturbation series as (3.12):

$$E(\mathbf{k}) = E_0(\mathbf{k}) + \alpha^2 E_2(\mathbf{k}) + O(\alpha^4) \quad (3.13)$$

where $E_0(\mathbf{k}) = \text{trace}(X_0(\mathbf{k}))$ is the nominal energy spectrum in the absence of base flow perturbations, and $E_2(\mathbf{k}) = \text{trace}(X_2(\mathbf{k}))$ captures the effect of base flow perturbations at the level of α^2 . When $\alpha \ll 1$, the correction $\alpha^2 E_2(\mathbf{k})$ provides a good approximation of the discounted spectrum $E_c(\mathbf{k})$ in Eq. (3.9), and as α grows, higher-order terms may be needed to approximate $E(\mathbf{k})$.

CHAPTER 4

EFFECT OF BASE FLOW VARIATIONS ON TRANSITIONAL FLOWS

In this chapter, we examine the dynamics of stochastically forced Couette and Poiseuille flows in the presence of zero-mean white-in-time stochastic uncertainty $\bar{\gamma}_u$ in the streamwise direction. The nominal dynamics are obtained by linearizing the NS equations around $\bar{\mathbf{u}} = [\bar{U}(y) \ 0 \ 0]^T$ with $\bar{U}(y) = y$ for Couette flow (Fig. 1.1(a)) and $\bar{U}(y) = 1 - y^2$ for Poiseuille flow (Fig. 1.1(b)). Throughout this chapter, we use $N = 101$ Chebyshev collocation points to discretize the operators involved in the linearized equations. Grid convergence is ensured by doubling the number of collocation points. We first examine the MSS of the flow in the presence of streamwise base flow perturbations. Our analysis identifies critically destabilizing perturbation variances over a range of Reynolds numbers. Using these critical variance levels, we examine the effect of base flow perturbations of various amplitude on the energy spectrum and dominant flow structures.

4.1 Stability analysis

For both Couette and Poiseuille flows, we use the stability condition presented in chapter 3.2 to examine the MSS of the horizontal wavenumber pair $\mathbf{k} = (1, 1)$, which corresponds to an oblique flow structure. Both DNS (Reddy et al., 1998) and nonlinear optimal perturbation analysis (Rabin et al., 2012) have demonstrated the fragility of such flow structures in transition mechanisms, i.e., oblique modes require less energy to induce transition than streamwise elongated modes. The high sensitivity of such three-dimensional flow structures to additive streamwise excitations was also demonstrated using frequency response analysis of the linearized NS equations (Jovanovic and Bamieh, 2005).

Figure 4.1 shows the minimum destabilizing variance σ_u^2 over a range of Reynolds numbers for $\mathbf{k} = (1, 1)$ when the base flow is perturbed at different wall-normal regions. The shaded

areas under the curves denote the Reynolds numbers and perturbation variances for which the flows remain asymptotically mean-square stable. In both flows, higher variances σ_u^2 could be tolerated when stochastic perturbations were confined to the wall-normal regions close to the walls, i.e., when $f(y)$ corresponds to the shape function shown in Fig. 2.1(b). As expected, both flows become less robust to base flow perturbations as the region of influence grows in the wall-normal dimension. We also observe that while the stability curves corresponding to the oblique mode in Couette and Poiseuille flows are similar for near-wall perturbations (Fig. 2.1(b)), the oblique mode in Poiseuille flow is, generally, more sensitive to channel-wide base flow perturbations ($f(y) = \bar{U}(y)$ and Fig. 2.1(a)).

While it generally becomes easier to destabilize the flow at higher Reynolds numbers, critical variance levels demonstrate different Reynolds number scaling when base flow perturbations are confined to different wall-normal regions. In both Couette and Poiseuille flows the critical variance of near-wall base flow perturbations (Fig. 2.1(b)) are found to scale as R^{-1} . In other words, it is reasonable to expect larger persistent stochastic perturbations with variances of the same order (R^{-1}) to induce $O(R^{-1})$ growth rates that can instigate transition. On the other hand, if perturbations follow the shape of the corresponding base flows ($f(y) = \bar{U}(y)/|\bar{U}(y)|$), the critical variance levels decrease at a slower rate ($R^{-0.5}$). When the base flow perturbations are allowed to enter through the entire wall-normal extent of the channel (Fig. 2.1(a)), the critical variance levels are found to scale as $O(R^{-1})$ in Couette flow and at an increasing rate in Poiseuille flow ($O(R^{-0.5})$ for $R < 600$ and $O(R^{-1.2})$ for $R > 600$). It is noteworthy that the Reynolds number scaling obtained using our stochastic approach is in agreement with the scaling observed in (Bottaro et al., 2003) for the magnitude of deterministic (worst-case) base flow perturbations. We note that besides $\mathbf{k} = (1, 1)$, a similar Reynolds number dependence can be observed for the critical variance of base flow perturbations at other horizontal wavenumber pairs. For Couette flow at $R = 500$ and Poiseuille flow at $R = 2000$ subject to base flow perturbations with $f(y) = \bar{U}(y)/|\bar{U}(y)|$,

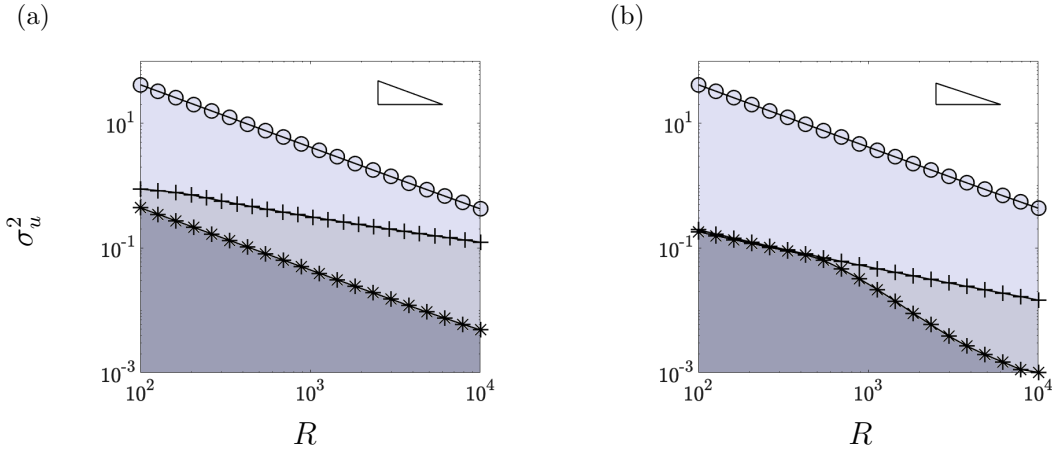


Figure 4.1. Stability curves for fluctuation dynamics with $\mathbf{k} = (1, 1)$ in (a) Couette flow; and (b) Poiseuille flow. The curves demonstrate the Reynolds number dependence of the maximum tolerable variance for stochastic base flow perturbations entering the dynamics through $f(y) = \bar{U}(y)/|\bar{U}(y)|$ (+) or the shape functions $f(y)$ depicted in Figs. 2.1(a) (*) and 2.1(b) (o). For a given Reynolds number, the shaded areas under the curves denote the variances of stochastic base flow uncertainty that do not violate MSS ($\rho(\mathbb{L}) < 1$ with $\alpha = 1$). The triangles in the upper right corners demonstrate an R^{-1} slope.

Fig. 4.2 shows the critical variance levels σ_u^2 for flow fluctuations with different spanwise and streamwise wavenumbers. In both flows, streamwise elongated structures (smaller k_x) are more robust toward streamwise base flow perturbations. On the other hand, the sensitivity to such perturbations is largely invariant to the width of flow structures and only decreases for longer flow structures when $\lambda_z \lesssim 1$. Based on Fig. 4.2, streamwise elongated structures (streaks) that are thin in the spanwise dimension exhibit the least sensitivity to such base flow uncertainty. Finally, we note that similar trends can be observed in both flows when base flow perturbations are allowed to enter a larger extent of the wall-normal domain (when $f(y)$ follows Fig. 2.1(a)).

4.2 Energy spectrum of velocity fluctuations

We now use the maximum tolerable variance over all horizontal wavenumber pairs to study the effect of base flow perturbations on the energy spectrum of velocity fluctuations. In

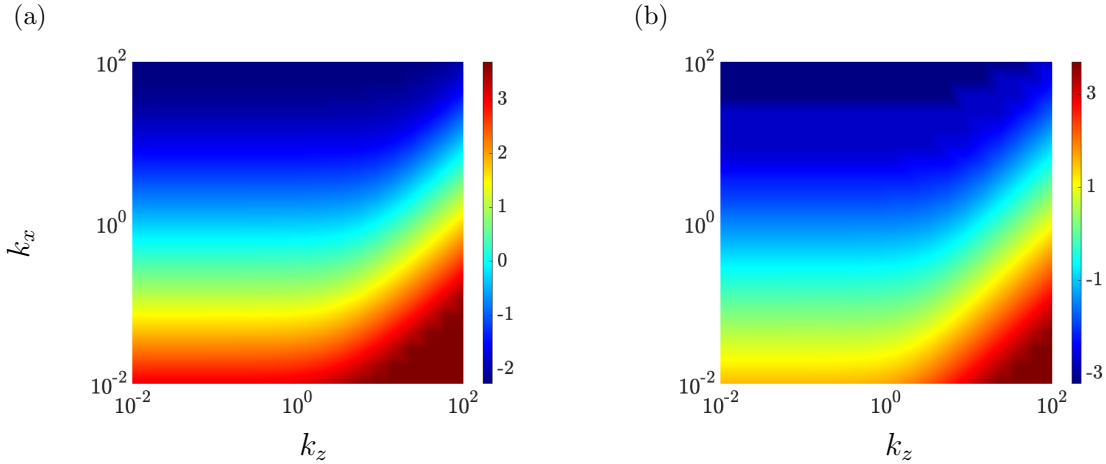


Figure 4.2. Logarithmically scaled critical variance levels for stochastic multiplicative uncertainty $\bar{\gamma}_u$ with $\alpha = 1$ and $f(y) = \bar{U}(y)/|\bar{U}(y)|$ over the horizontal wavenumber spectrum in (a) Couette flow with $R = 500$; and (b) Poiseuille flow with $R = 2000$.

both flows, the most sensitive modes that have been considered in Fig. 4.2 correspond to $\mathbf{k} = (100, 0.01)$. In Couette flow with $R = 500$, the critical variance levels σ_u^2 for streamwise base flow perturbations that enter through wall-normal regions corresponding to $f(y) = \bar{U}(y)/|\bar{U}(y)|$, Fig. 2.1(a), and Fig. 2.1(b) to destabilize this mode are 0.44, 0.09, and 8.3, respectively. These values change to 0.03, 0.008, and 2.09 in Poiseuille flow with $R = 2000$. In the numerical experiments of this section, we consider slightly lower variance levels than these critical values to ensure MSS over all length-scales. Moreover, we assume the stochastic input \mathbf{f} to be white-in-time with trivial covariance $\Omega = I$.

In the absence of multiplicative uncertainty ($\bar{\gamma}_u = 0$), Eq. (3.7) reduces to a standard algebraic Lyapunov equation. The nominal energy spectra E_0 of plane Couette and Poiseuille flows, which can be computed from the solution of this Lyapunov equation, are shown in Figs. 4.3(a) and 4.3(b), respectively. In the perturbed case, we use the perturbation analysis presented in chapter 3.3 to compute the effect of base flow perturbations on the energy of velocity fluctuations by solving a sequence of standard algebraic Lyapunov equations (Eqs. (B.2)) instead of the generalized Lyapunov equation (3.10). Figure 4.4 validates this

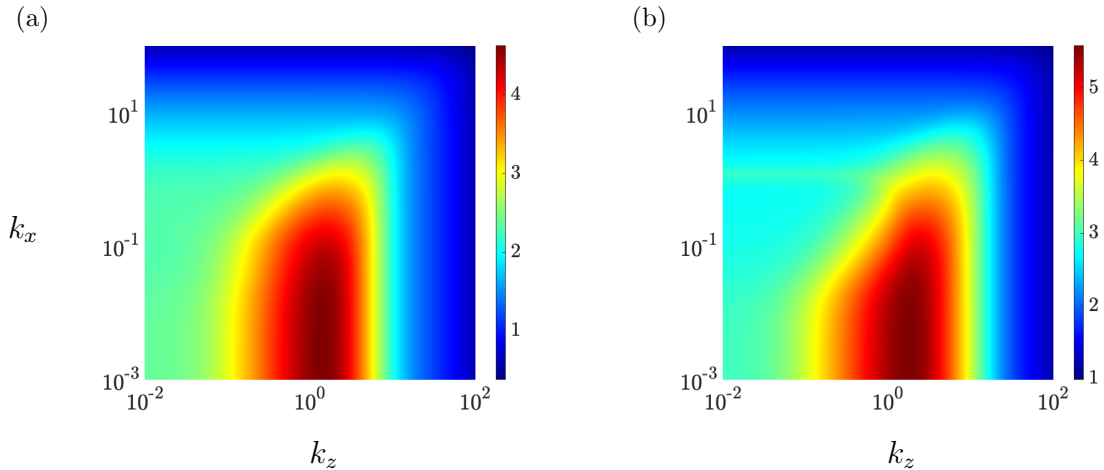


Figure 4.3. Energy spectra of (a) plane Couette flow with $R = 500$ and (b) plane Poiseuille flow with $R = 2000$. Color plots show $\log_{10}(E_0(\mathbf{k}))$.

approach in predicting the discounted energy spectrum E_c (Eq. (3.9)) of plane Couette flow at $k_x = 1$ due to small amplitude base flow perturbations with $f(y) = \bar{U}(y)/|\bar{U}(y)|$. This streamwise wavenumber will be shown to contain the most sensitive region of the spectrum (Fig. 4.5). It is evident that for small perturbation amplitudes α , even the second-order correction (at the level of α^2) is in excellent agreement with the direct solution whose computational cost is significantly higher.

Figure 4.5 shows the second-order correction to the energy spectrum ($E_2(\mathbf{k})$) of Couette and Poiseuille flow induced by base flow perturbations of various shape $f(y)$. Clearly, base flow perturbations have resulted in the amplification of all spatial scales. As shown in Fig. 4.3, the amplification of streamwise elongated flow structures (streaks) dominates the energy spectra of nominal (unperturbed) flows. In contrast, small-amplitude channel-wide base flow perturbations (when $f(y) = \bar{U}(y)/|\bar{U}(y)|$ or Fig. 2.1(a)) predominantly influence the oblique modes with $k_x \approx 1$ and $k_z \sim O(1)$ (marked by \times), and near-wall perturbations (when $f(y)$ corresponds to Fig. 2.1(b)) result in the dominant amplification of Tollmien–Schlichting (TS) waves (marked by \bullet). We remark that even though the amplification of TS waves is overcome by that of oblique modes when channel-wide base flow perturbations are applied,

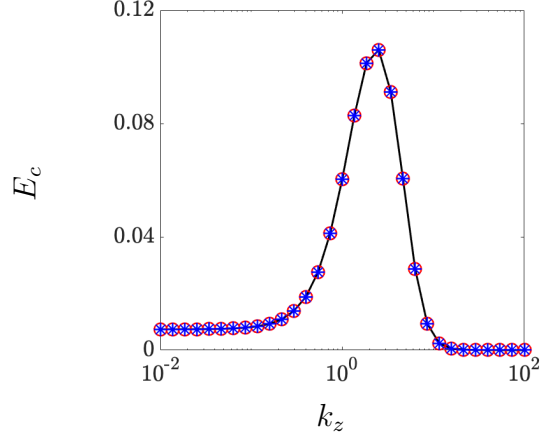


Figure 4.4. The discounted energy spectrum E_c in Couette flow with $R = 500$ and $k_x = 1$ subject to base flow perturbations with $f(y) = \bar{U}(y)/|\bar{U}(y)|$ with $\sigma_u^2 = 0.43$ and $\alpha = 0.01$. Direct solution from solving Eq. (3.11)(-); and approximate solutions from perturbation analysis: $E_c = \alpha^2 E_2(\mathbf{k})$ (*) and $E_c = \alpha^2 E_2(\mathbf{k}) + \alpha^4 E_4(\mathbf{k})$ (o).

their local signature at $k_z \approx 0$ prevails in all cases. Figures 4.5(c,d) demonstrate that the amplification of streaks is quite robust to base flow perturbations that are not confined in the wall-normal direction (Fig. 2.1(a)). This is because at $k_x = 0$ stochastic base flow perturbations have no way to influence the solution of Eq. (3.7) as the main diagonal blocks of A_u would be zero and the off-diagonal (coupling) term, which includes the wall-normal derivative of $f(y)$, is predominantly zero (apart from the immediate vicinity of the walls); see Appendix A. This is in agreement with the findings of the worst-case adjoint-based analysis conducted for a zero-pressure-gradient boundary layer in (Brandt et al., 2011), where the lack of influence on streamwise streaks is evident from the structure of the analytically derived gradient of resolvent singular values. It follows from the form of perturbation matrices A_u and A_w in Appendix A that streaks would be susceptible to multiplicative sources of uncertainty that enter the dynamics through other components of the base state or involve significant wall-normal variations (cf. Figs. 4.5(a,b) and 4.5(e,f)).

Figure 4.6 shows the correction to the energy spectrum ($E_c(\mathbf{k})$) of Couette and Poiseuille flows in the presence of higher-amplitude base flow perturbations. The perturbation ampli-

tude $\alpha = 0.5$ considered in this figure corresponds to the maximum perturbation amplitude for which the result of perturbation analysis is in agreement with the direct solution of Eq. (3.11). In obtaining these plots the limit of the perturbation series (3.13) was obtained using 4 terms in the perturbation series, i.e., $Ec = \alpha^2 E_2 + \alpha^4 E_4$, and verified using the Shanks transformation (Shanks, 1955; Dyke, 1964). This transformation provides the means to improve the convergence rate of slowly convergent series and to even achieve convergence when the original series is divergent (Sidi, 2003); see Appendix B for details. Figure 4.6 shows that for high amplitudes base flow perturbations, apart from a uniform increase in the energy correction over all scales (by approximately $O(3)$), the amplification trends predominantly follow the predictions of Fig. 4.5 for small amplitude perturbations. For both Couette and Poiseuille flows, Fig. 4.7 examines the dependence of the normalized correction to the total kinetic energy on the amplitude of base flow perturbations that enter the dynamics through various shape functions $f(y)$ and with uncertainty variances σ_u^2 that correspond to the maximum tolerable values identified in Fig. 4.1. These figures show that the correction to kinetic energy increases as the wall-normal extent of base flow perturbations becomes larger. We also observe that as the amplitude of base flow perturbations increases the exponential growth rate approaches that of higher powers of α (cf. Eq. (3.13)).

4.3 Maximally affected flow structures

Following the proper orthogonal decomposition of (Bakewell and Lumley, 1967; Moin and Moser, 1989), we extract the dominant flow structures that result from the steady-state stochastic analysis of transitional flow in the presence of base flow uncertainty. These flow structures can be formed from the energetically dominant eigenvectors of the velocity covariance matrix $\Phi(\mathbf{k}) = C(\mathbf{k})X(\mathbf{k})C^*(\mathbf{k})$, where $X(\mathbf{k})$ represents the solution of the generalized Lyapunov equation (3.11). Following the eigenvalue decomposition of Φ , the symmetries in

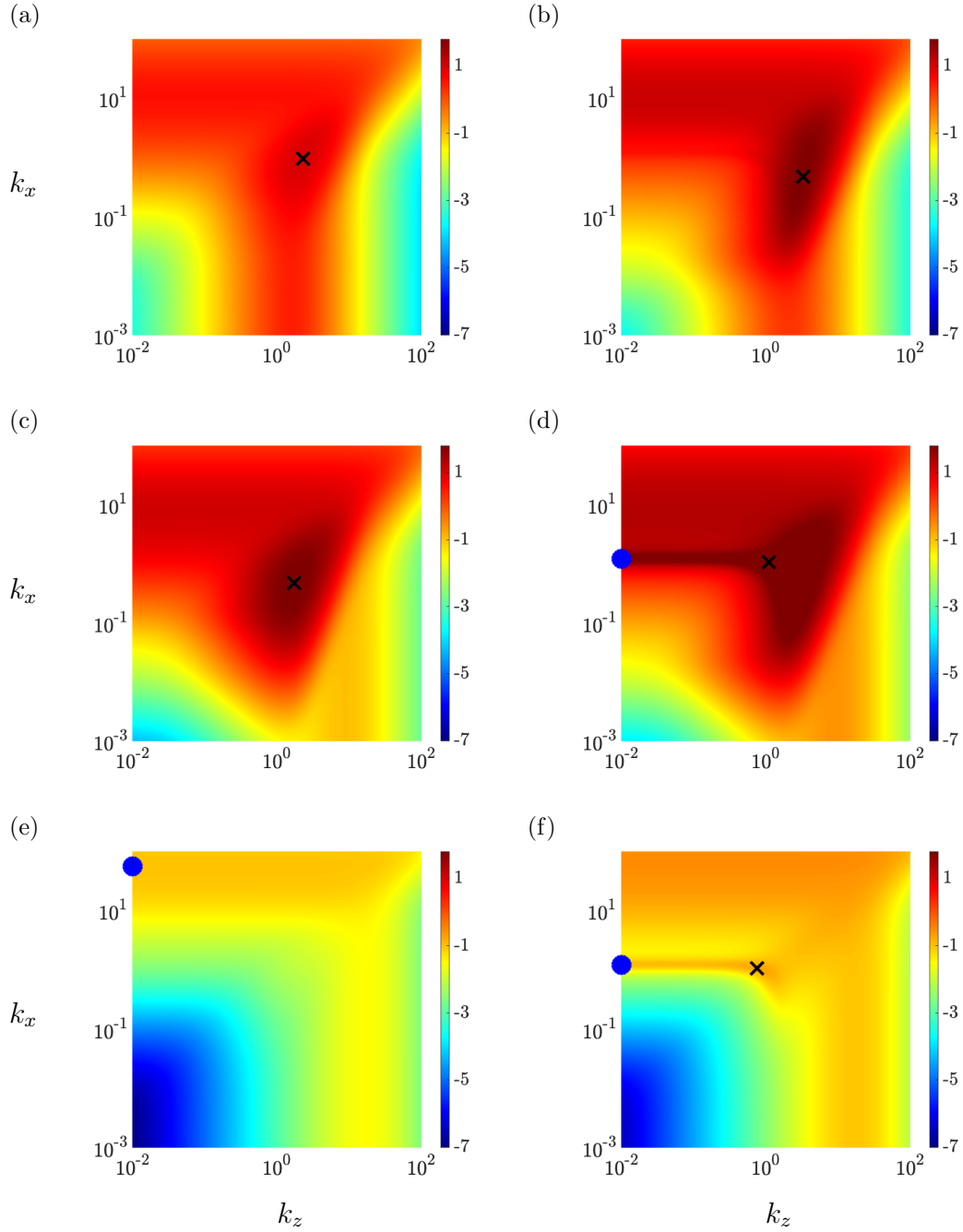


Figure 4.5. The second-order correction to the energy spectrum $E_2(\mathbf{k})$ due to multiplicative uncertainty $\bar{\gamma}_u$ in Couette flow with $R = 500$ (left); and Poiseuille flow with $R = 2000$ (right). Shape functions: (a,b) $f(y) = \bar{U}(y)/|\bar{U}(y)|$; (c,d) Fig. 2.1(a); (e,f) Fig. 2.1(b). Variances σ_u^2 : (a) 4.38×10^{-3} ; (b) 6.25×10^{-4} ; (c) 0.004; (d) 6.25×10^{-4} ; (e) 0.005; (f) 0.001. Color plots show $\log_{10}(E_2(\mathbf{k}))$. The symbols (\times) and (\bullet) mark the wavenumber pairs associated with oblique waves and TS waves, respectively.

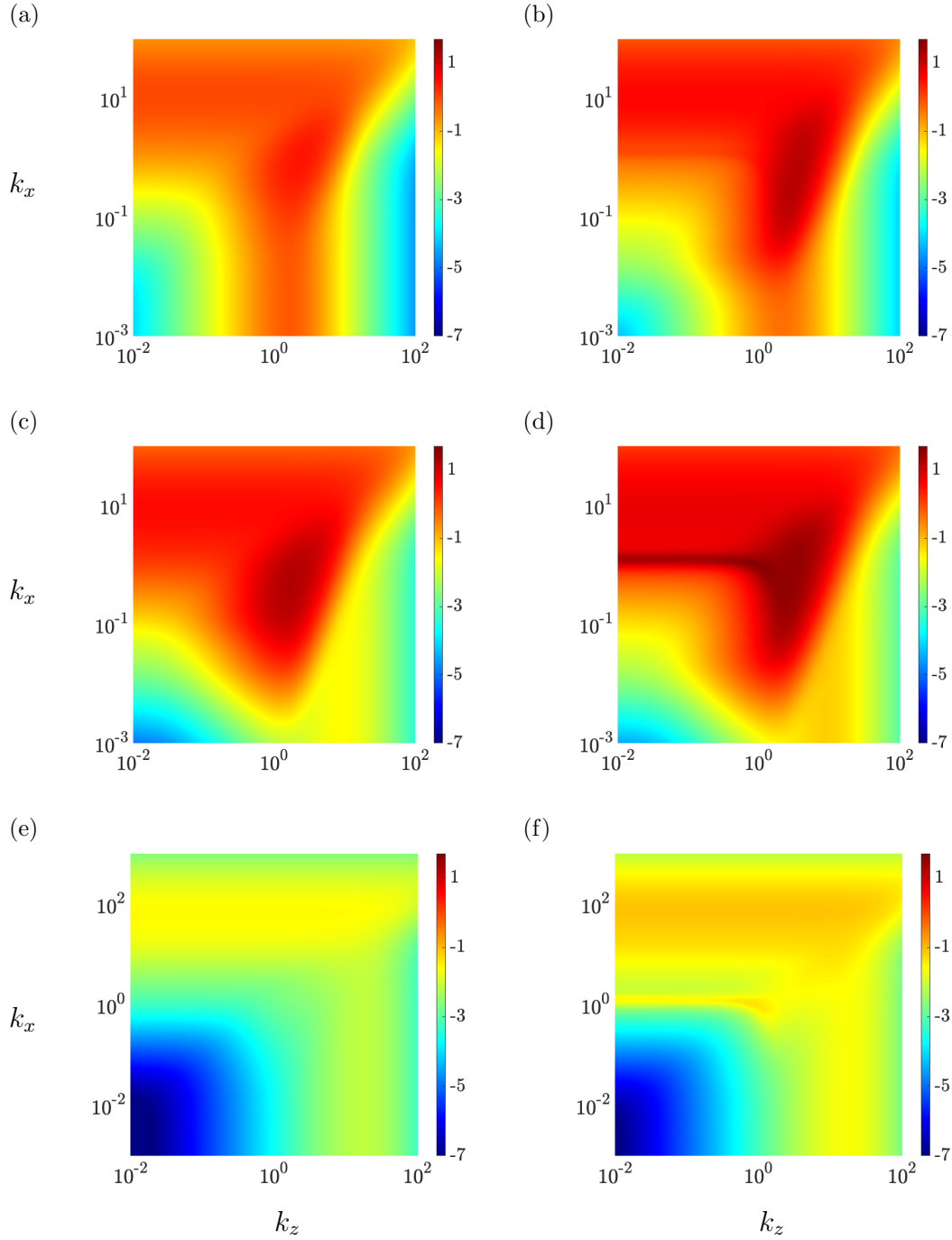


Figure 4.6. The correction to the energy spectrum $E_c(\mathbf{k})$ due to multiplicative uncertainty $\bar{\gamma}_u$ with $\alpha = 0.5$ in Couette flow with $R = 500$ (left); and Poiseuille flow with $R = 2000$ (right). Shape functions: (a,b) $f(y) = \bar{U}(y)/|\bar{U}(y)|$; (c,d) Fig. 2.1(a); (e,f) Fig. 2.1(b). Variances σ_u^2 : (a) 4.38×10^{-3} ; (b) 6.25×10^{-4} ; (c) 0.004; (d) 6.25×10^{-4} ; (e) 0.005; (f) 0.001. Color plots show $\log_{10}(E_c(\mathbf{k}))$.

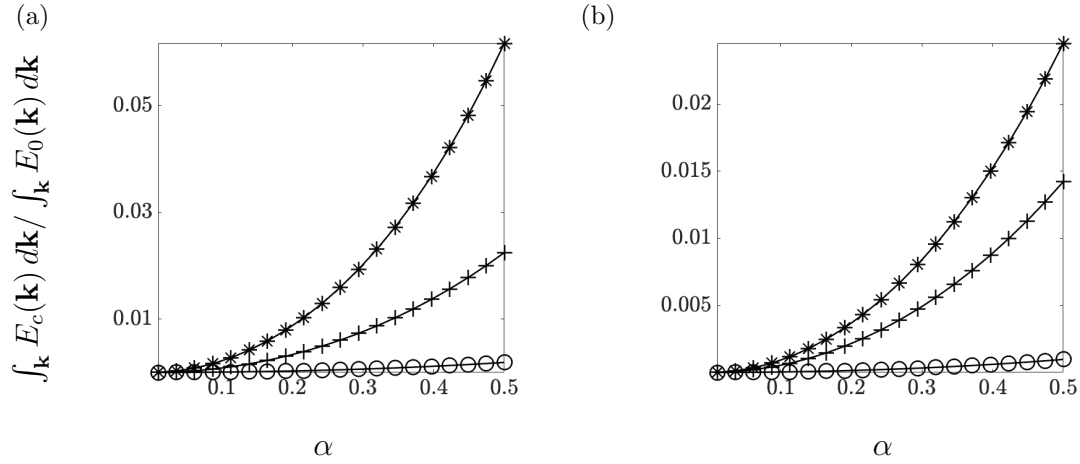


Figure 4.7. The relative correction to the turbulent kinetic energy $\int_{\mathbf{k}} E_c(\mathbf{k}) d\mathbf{k} / \int_{\mathbf{k}} E_0(\mathbf{k}) d\mathbf{k}$ in (a) Couette flow with $R = 500$; and (b) Poiseuille flow $R = 2000$ subject to base flow variations with amplitude α . The curves demonstrate the α dependence of the energy correction due to stochastic base flow perturbations entering the dynamics through $f(y) = \bar{U}(y)/|\bar{U}(y)|$ (+), Fig. 2.1(a) (*), and Fig. 2.1(b) (○). (a) Base flow perturbations are introduced with variances of $\sigma_u^2 = 4.38 \times 10^{-3}$ (+), 0.004 (*); and 0.005 (○) into Couette flow, and (b) $\sigma_u^2 = 6.25 \times 10^{-4}$ (+), 6.25×10^{-4} (*); and 0.001 (○) into Poiseuille flow.

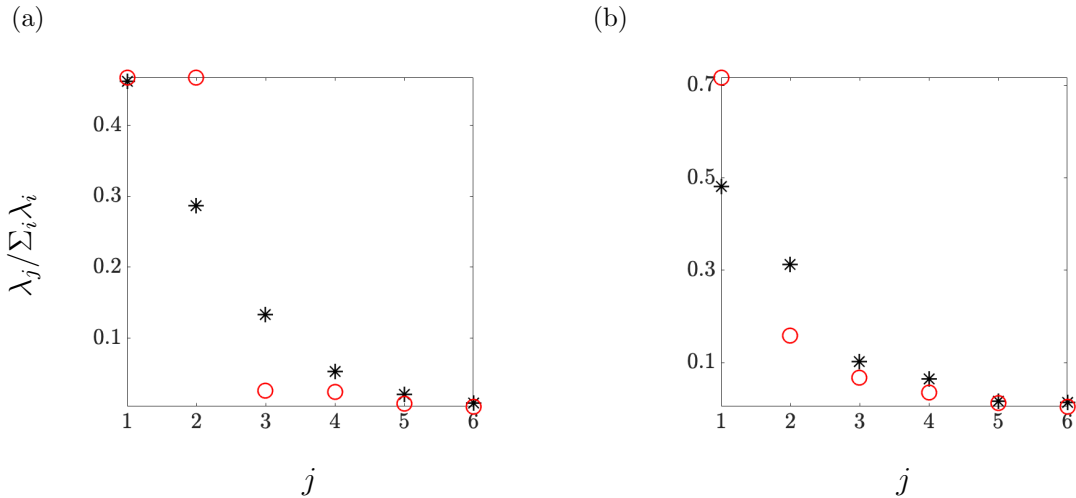


Figure 4.8. Contribution of the first six eigenvalues of the velocity covariance matrix Φ of channel flow in the absence (*) and presence (○) of base flow perturbations with $f(y) = \bar{U}(y)/|\bar{U}(y)|$ and amplitude $\alpha = 1$. (a) Couette flow with $R = 500$ at $\mathbf{k} = (0.95, 2.29)$; and (b) Poiseuille flow with $R = 2000$ at $\mathbf{k} = (0.38, 3.02)$. The variance of base flow uncertainties: (a) $\sigma_u^2 = 0.50$; (b) $\sigma_u^2 = 0.21$.

the wall-parallel directions can be used to construct the velocity components of flow structures as

$$\begin{aligned}
u(x, y, z) &= 4 \int_{k_x, k_z > 0} \cos(k_z z) \operatorname{Re}(\tilde{u}(y, \mathbf{k}) e^{i(k_x x)}) d\mathbf{k} \\
v(x, y, z) &= 4 \int_{k_x, k_z > 0} \cos(k_z z) \operatorname{Re}(\tilde{v}(y, \mathbf{k}) e^{i(k_x x)}) d\mathbf{k} \\
w(x, y, z) &= -4 \int_{k_x, k_z > 0} \sin(k_z z) \operatorname{Im}(\tilde{w}(y, \mathbf{k}) e^{i(k_x x)}) d\mathbf{k}.
\end{aligned} \tag{4.1}$$

Here, Re and Im denote real and imaginary parts, and \tilde{u} , \tilde{v} and \tilde{w} correspond to the streamwise, wall-normal, and spanwise velocity components of an eigenvector of $\Phi(\mathbf{k})$.

As shown in the previous section, while streamwise elongated streaks represent the energetically dominant flow structures in the nominal flow, oblique modes become increasingly relevant as the amplitude and variance of base flow perturbations grow. To demonstrate the influence of base flow perturbations on the energy and spatial extent of dominant flow structures, we will focus on base flow perturbations with $f(y) = \bar{U}(y)/|\bar{U}(y)|$ and the maximally affected oblique modes corresponding to the peaks in Figs. 4.6. Figure 4.8 shows the contribution of the first six eigenvalues of $\Phi(\mathbf{k})$ to the kinetic energy (sum of all eigenvalues) of Couette flow with $R = 500$ and Poiseuille flow with $R = 2000$ at the wavenumber pairs that correspond to the maximum amplification in Figs. 4.6(a) and 4.6(b); $\mathbf{k} = (0.95, 2.29)$ in Couette flow and $\mathbf{k} = (0.38, 3.02)$ in Poiseuille flow. The base flow perturbations are chosen to be of unit amplitude ($\alpha = 1$) with critically stable variance level identified in chapter 4.1. Based on Fig. 4.8(a), while streamwise base flow perturbations generally increase the energy of this oblique mode, they also concentrate the energy on the two most significant modes; the two most energetic modes in the perturbed flow contain 94% of the total energy which is a significant increase relative to 75% in the nominal flow. In contrast, Fig. 4.8(b) shows that base flow perturbations of Poiseuille flow increase the gap between the energy of the first and second most dominant eigenvalues; the perturbations increase the energetic contribution of the principal eigenvalue from 48% to 72% and decrease the contribution of the

second eigenvalue from 31% to 16%. Nevertheless, the presence of base flow perturbations increases the energetic contribution of the first two modes by 9% (from 79% to 88%).

We next visualize the streamwise component of the two most significant modes identified in Fig. 4.8 using Eq. (4.1). Figure 4.9(a) shows various views of the principal oblique structures corresponding to $\mathbf{k} = (0.95, 2.29)$ in nominal (first row) and perturbed (second row) Couette flow. While this wavenumber pair corresponds to nominally streamwise elongated mid-channel structures that are inclined to the walls, in the presence of base flow perturbations, it corresponds to near-wall streamwise elongated structures that are less inclined to the walls and exhibit an anti-symmetric arrangement with respect to the channel centerline. Similar to the energetically dominant streaks that are typically observed in such wall-bounded flows, the resulting oblique modes of the stochastically perturbed flow contain alternating regions of fast- and slow- moving fluid that are situated between counter-rotating vortical motion in the cross-stream plane (see third column of Fig. 4.9(a)). Figure 4.9(b) shows the spatial structure of the streamwise component of the second largest mode in Couette flow in the absence (first row) and presence (second row) of stochastic base flow perturbations. While in nominal conditions, the oblique mode corresponds to two rows of mid-channel streamwise elongated flow structures about the centerline, stochastic base flow perturbations give rise to near-wall flow structures that are similar to the principal modes (second row of Fig. 4.9(a)) but with a predominantly symmetric arrangement due to a phase shift. A similar analysis of the flow structures corresponding to the oblique modes ($\mathbf{k} = (0.38, 3.02)$) of Poiseuille flow is presented in Fig 4.10. Base flow perturbations cause the centerline conglomeration of the dominant flow structures that are nominally streamwise elongated and inclined to the wall (Fig. 4.10(a)). On the other hand, apart from a slight wall-normal elevation, such perturbations do not influence the physical structure of the second most significant mode (Fig. 4.10(b)).

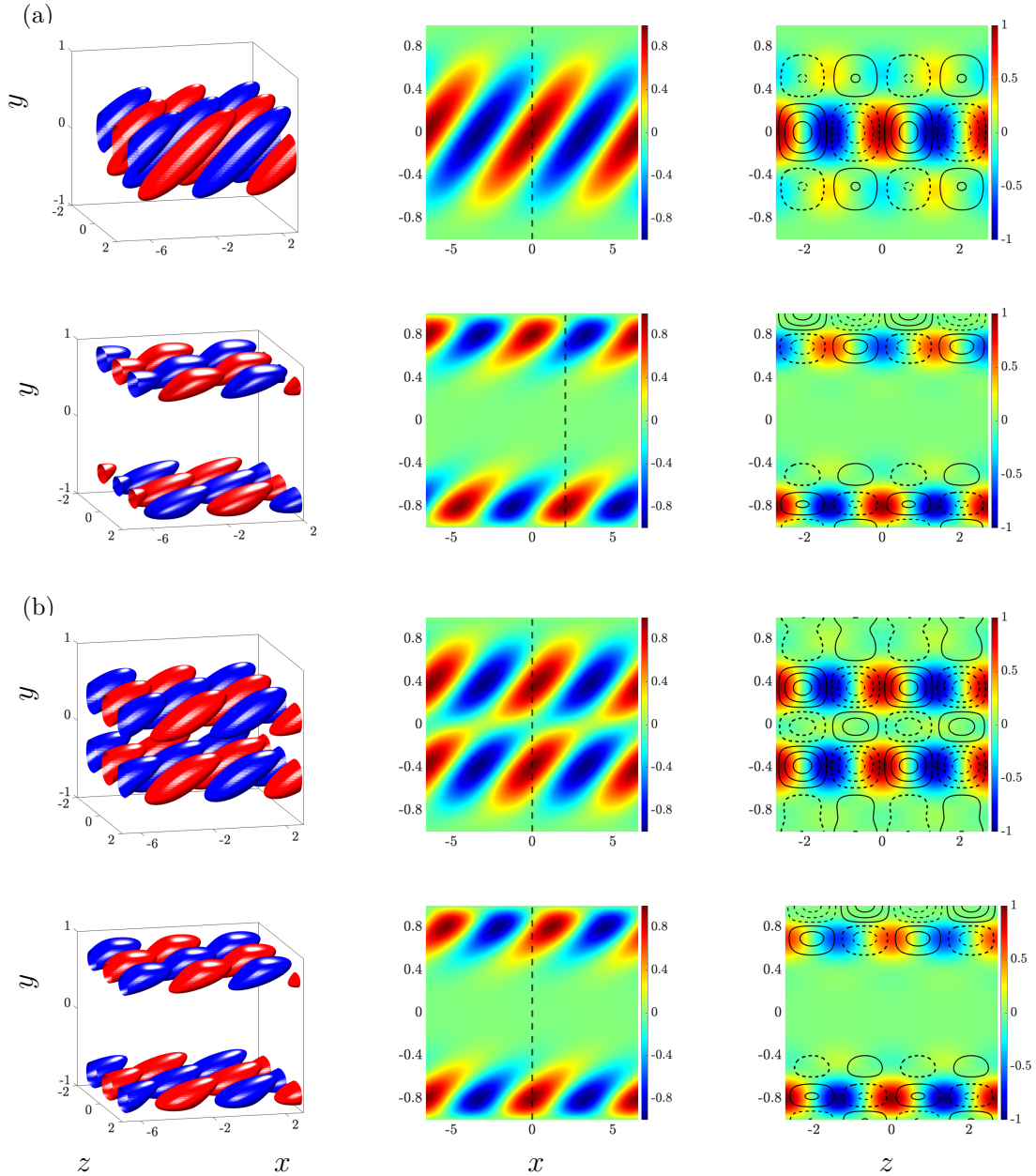


Figure 4.9. Streamwise component of dominant flow structures of Couette flow with $R = 500$ and $\mathbf{k} = (0.95, 2.29)$ in the absence (first rows) and presence (second rows) of stochastic base flow perturbations with $f(y) = \bar{U}(y)/|\bar{U}(y)|$, $\alpha = 1$, and $\sigma_u^2 = 0.50$; (a) principal modes; and (b) second most energetic modes: (left) the spatial structure of the eigenmodes with high (red) and low (blue) velocity; (middle) the streamwise velocity at $z = 0$; and (right) the $y-z$ slice of streamwise velocity (color plots) and vorticity (contour lines) at the streamwise location indicated by the dashed vertical lines in the middle panel.

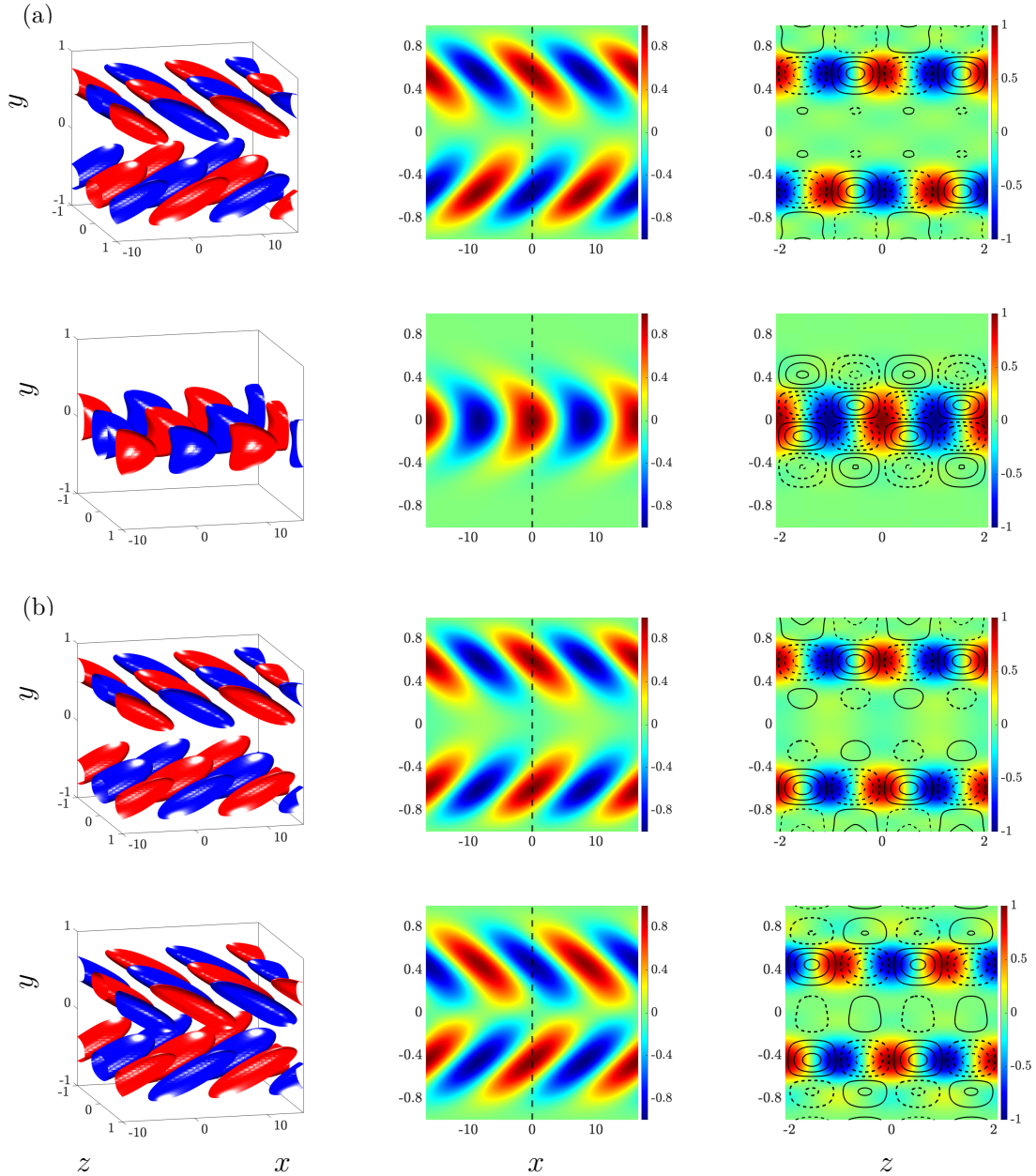


Figure 4.10. Streamwise component of dominant flow structures of Poiseuille flow $R = 2000$ and $\mathbf{k} = (0.38, 3.02)$ in the absence (first rows) and presence (second rows) of stochastic base flow perturbations with $f(y) = \bar{U}(y)/|\bar{U}(y)|$, $\alpha = 1$, and $\sigma_u^2 = 0.21$; (a) principal modes; and (b) second most energetic modes: (left) the spatial structure of the eigenmodes with high (red) and low (blue) velocity; (middle) the streamwise velocity at $z = 0$; and (right) the $y - z$ slice of streamwise velocity (color plots) and vorticity (contour lines) at the streamwise location indicated by the dashed vertical lines in the middle panel.

CHAPTER 5
EFFECT OF BASE FLOW VARIATIONS ON TURBULENT
FLOW DYNAMICS

In this chapter, we examine the dynamics of stochastically forced turbulent channel flow in the presence of zero-mean white-in-time stochastic base flow perturbations. To this end, we augment the molecular viscosity in the NS equations (2.1) with the turbulent viscosity ν_T of channel flow

$$\begin{aligned}\tilde{\mathbf{u}}_t &= -(\tilde{\mathbf{u}} \cdot \nabla) \tilde{\mathbf{u}} - \nabla \tilde{P} + \frac{1}{R_\tau} \nabla \cdot ((1 + \nu_T) (\nabla \tilde{\mathbf{u}} + (\nabla \tilde{\mathbf{u}})^T)) \\ 0 &= \nabla \cdot \tilde{\mathbf{u}}\end{aligned}\tag{5.1}$$

and linearize around the long-time averaged turbulent mean flow profile $\mathbf{u} = [U(y) \ 0 \ 0]^T$ provided by DNS of channel flow (Del Álamo and Jiménez, 2003; Del Álamo et al., 2004; Hoyas and Jiménez, 2006; Hoyas and Jimenez, 2008) (Fig. 1.1(c)) to obtain the linearized NS equations

$$\begin{aligned}\mathbf{v}_t &= -(\nabla \cdot \mathbf{u}) \mathbf{v} - (\nabla \cdot \mathbf{v}) \mathbf{u} - \nabla p + \frac{1}{R_\tau} \nabla \cdot ((1 + \nu_T) (\nabla v + (\nabla v)^T)) \\ 0 &= \nabla \cdot \mathbf{v}\end{aligned}\tag{5.2}$$

which govern the dynamics of velocity, \mathbf{v} , and pressure, p , fluctuations. Here, the Reynolds number $R_\tau = u_\tau h / \nu$ is defined in terms of the channel's half-height h and the friction velocity $u_\tau = \sqrt{\tau_w / \rho}$, where τ_w is the wall-shear stress (averaged over horizontal directions and time), ρ is fluid density, and ν is kinematic viscosity. For turbulent viscosity, we use the Reynolds and Tiederman (Reynolds and Tiederman, 1967) turbulent viscosity profile

$$\nu_T(y) = \frac{1}{2} \left(\left(1 + \left(\frac{c_2}{3} R_\tau (1 - y^2)(1 + 2y^2)(1 - e^{-(1-|y|)R_\tau/c_1}) \right)^{1/2} \right) - 1 \right)\tag{5.3}$$

where parameters c_1 and c_2 are selected to minimize the least squares deviation between the steady-state solution to (5.2) using the averaged wall-shear stress $\tilde{P}_x = -1$ and the mean

streamwise velocity obtained in experiments or simulations. Application of this least-squares procedure in finding the best fit to the mean velocity in turbulent channel flow resulting from DNS (Del Álamo and Jiménez, 2003; Del Álamo et al., 2004; Hoyas and Jiménez, 2006; Hoyas and Jimenez, 2008) yields $\{c_1 = 46.2, c_2 = 0.61\}$ at $R_\tau = 186$, $\{c_1 = 29.4, c_2 = 0.45\}$ at $R_\tau = 547$, $\{c_1 = 27, c_2 = 0.43\}$ at $R_\tau = 934$, and $\{c_1 = 25.4, c_2 = 0.42\}$ at higher Reynolds numbers.

We assume the streamwise component of the base flow \mathbf{u} to be contaminated with an additive source of uncertainty $\gamma_u(y, t) = \alpha \bar{\gamma}(t) f(y)$. As a result, the dynamic operator \mathbf{A} in the state-space representation (2.4) takes the form

$$\mathbf{A}(\mathbf{k}, t) := \begin{bmatrix} \mathbf{A}_{11} & 0 \\ \mathbf{A}_{21} & \mathbf{A}_{22} \end{bmatrix} \quad (5.4)$$

$$\mathbf{A}_{11}(\mathbf{k}, t) := \Delta^{-1} \left(\frac{1}{R_\tau} \left((1 + \nu_T) \Delta^2 + 2\nu'_T \Delta \partial_y + \nu''_T (\partial_y^2 + k^2) \right) + \right. \\ \left. ik_x (\bar{U}''(y) + \gamma''_u(y, t) - (\bar{U}(y) + \gamma_u(y, t)) \Delta) \right)$$

$$\mathbf{A}_{21}(\mathbf{k}, t)1 := -ik_z (\bar{U}'(y) + \gamma'_u(y, t))$$

$$\mathbf{A}_{22}(\mathbf{k}, t) := \frac{1}{R_\tau} \left((1 + \nu_T) \Delta + \nu'_T \partial_y \right) - ik_x (\bar{U}(y) + \gamma_u(y, t))$$

where $\bar{U}(y)$ corresponds to the streamwise component of the base flow in the absence of uncertainty. In a similar manner as Eq. (2.8), the operator-valued matrix \mathbf{A} can be decomposed into its nominal and perturbed components, i.e.,

$$\mathbf{A}(\mathbf{k}, t) = \bar{\mathbf{A}}(\mathbf{k}) + \alpha \bar{\gamma}_u(t) \mathbf{A}_u(\mathbf{k}) \quad (5.5)$$

where expressions for $\bar{\mathbf{A}}$ and \mathbf{A}_u are given in Appendix C.

We next discretize the differential operators in the linearized equations using $N = 151$ Chebyshev collocation points in the wall-normal direction and study the MSS and frequency response of the flow fluctuations in the presence of both additive stochastic forcing \mathbf{f} and

stochastic base flow perturbations γ_u . We will assume that perturbations γ_u enter the dynamics through the same shape functions considered in the prior chapter.

5.1 Stability analysis

For $\mathbf{k} = (2.5, 7)$, we analyze the MSS of the linearized NS equations around the DNS-generated mean velocity profile of turbulent channel flow $\bar{U}(y)$ at $R_\tau = 186, 547, 934, 2003,$ and 4179 (Del Álamo and Jiménez, 2003; Del Álamo et al., 2004; Hoyas and Jiménez, 2006; Hoyas and Jimenez, 2008). While we focus on $\mathbf{k} = (2.5, 7)$, which is the horizontal wavenumber pair at which the premultiplied energy spectrum of channel flow at $R_\tau = 186$ peaks, we note that similar stability trends were observed at other wavenumbers. The stability curves shown in Fig. 5.1(a) demonstrate the Reynolds number dependence of the critical variance σ_u^2 of stochastic base flow perturbation $\gamma_u(y, t)$. As expected, the fragility of this mode to base flow perturbations increases as the Reynolds numbers grows apart from an initial increase observed in the case of full channel perturbations ($f(y)$ corresponding to Fig. 2.1(a)) from $R_\tau = 186$ to 547 . The critical variance is found to approximately scale as R_τ^{-1} with higher tolerance for stochastic perturbations entering in the near-wall regions, i.e., when $f(y)$ is given by Fig. 2.1(b). Similar to the findings of chapter 4.1, the critical variance of turbulent channel flow at any given Reynolds number R_τ is lowest for length-scales that are short in the streamwise dimension, but infinitely wide in the spanwise dimension (Fig. 5.1(b)).

The maximum tolerable variance of stochastic multiplicative uncertainty can provide guidelines for the number and quality of DNS-generated samples that should be involved in the statistical averaging process that leads to a stable equilibrium for linearized analysis. We note that for all Reynolds numbers studied here, and at all wall-normal locations, the reported variance of the numerically generated turbulent mean velocities is significantly lower than the critical values identified by our MSS analysis. Nevertheless, one implication of the

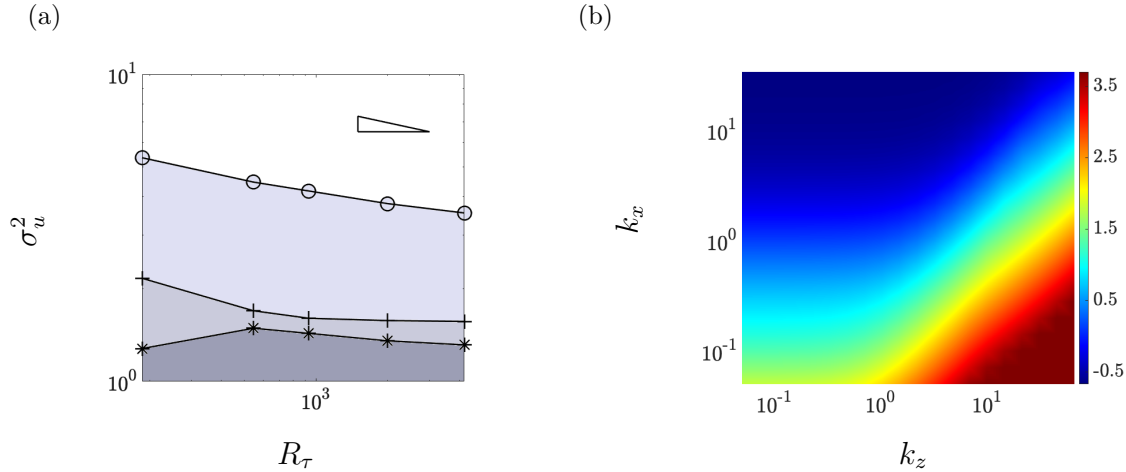


Figure 5.1. (a) Stability curves for fluctuation dynamics with $\mathbf{k} = (2.5, 7)$ in turbulent channel flow subject to stochastic base flow perturbations following $f(y) = \bar{U}(y)/|\bar{U}(y)|$ (+); or the shape functions $f(y)$ shown in Fig. 2.1(a) (*); and Fig. 2.1(b) (○). The shaded areas under the curves denote the variances of stochastic base flow uncertainty that do not violate MSS ($\rho(L) < 1$ with $\alpha = 1$). The triangle in the upper right corner demonstrates an R_τ^{-1} slope. (b) Logarithmically scaled critical variance levels of stochastic multiplicative uncertainty $\bar{\gamma}_u$ with $\alpha = 1$ and $f(y) = \bar{U}(y)/|\bar{U}(y)|$ over the horizontal wavenumber spectrum of turbulent channel flow with $R_\tau = 186$.

uncovered Reynolds number dependence observed in Fig. 5.1(a) for statistical averaging is that the admissible variance in estimating the turbulent mean velocity $\bar{U}(y)/|\bar{U}(y)|$ reduces (at the rate of R_τ^{-1}) as the Reynolds number grows.

5.2 Energy spectrum of velocity fluctuations

We now use analyze the effect of base flow perturbations on the energy spectrum of velocity fluctuations. We guarantee MSS by adjusting the variance of base flow perturbations to the maximum tolerable variance across all wavenumber pairs. For example, when $f(y) = \bar{U}(y)/|\bar{U}(y)|$, this critical variance corresponds to the shortest and widest length scales, and is identified as 0.13; see Fig. 5.1(b). We note that the overall trend observed in Fig. 5.1(b) along with the critical variance of the most sensitive mode is invariant to variations in the wall-normal extent of base flow perturbations. The steady-state covariance of velocity fluctuations

in Eqs. (5.2) can be computed from solving Eq. (3.7). Following (Moarref and Jovanovic, 2012), we select the covariance of white-in-time forcing to guarantee equivalence between the two-dimensional energy spectrum of turbulent channel flow and the flow obtained by linearized NS equations in the absence of base flow perturbations ($\gamma_u = 0$). This is achieved via the scaling

$$\Omega(\mathbf{k}) = \frac{\bar{E}(\mathbf{k})}{\bar{E}_0(\mathbf{k})} \Omega_0(\mathbf{k})$$

where $\bar{E}(\mathbf{k}) = \int_{-1}^1 E(y, \mathbf{k}) dy$ is the two-dimensional energy spectrum of a turbulent channel flow obtained using the DNS-based energy spectrum $E(y, \mathbf{k})$ (Del Álamo and Jiménez, 2003; Del Álamo et al., 2004), and $\bar{E}_0(\mathbf{k})$ is the energy spectrum resulting from the linearized NS equations in the absence of base flow perturbations and subject to a white-in-time forcing \mathbf{f} with covariance

$$\Omega_0(\mathbf{k}) = \begin{bmatrix} \sqrt{E(y, \mathbf{k})} I & 0 \\ 0 & \sqrt{E(y, \mathbf{k})} I \end{bmatrix} \begin{bmatrix} \sqrt{E(y, \mathbf{k})} I & 0 \\ 0 & \sqrt{E(y, \mathbf{k})} I \end{bmatrix}^*$$

Figure 5.2(a) shows the premultiplied energy spectrum of turbulent channel flow with $R = 186$ in the absence of stochastic base flow perturbations in the linearized dynamics ($\bar{\gamma}_u(t) = 0$). The changes to the premultiplied energy spectrum $k_x k_z E_c(\mathbf{k})$ due to stochastic multiplicative uncertainties with $\alpha = 0.05$ entering through various wall-normal regions are shown in Fig. 5.2(b)-(d). Since the amplitude of base flow perturbations is small, the second-order correction to the perturbation series of energy provides a sufficient approximation of the change to the energy spectrum, i.e., $E_c(\mathbf{k}) = \alpha^2 E_2$. Figures 5.2(e)-(g) consider the case of higher-amplitude base flow perturbations ($\alpha = 0.9$) on the premultiplied energy spectrum by $k_x k_z E_c(\mathbf{k})$, where $E_c(\mathbf{k})$ is given in Eq. (3.9). In computing $E_c(\mathbf{k})$, the limit was obtained using an 8th-order perturbation series, i.e., $Ec = \alpha^2 E_2 + \alpha^4 E_4 + \alpha^6 E_6 + \alpha^8 E_8$, and verified using the Shanks transformation (Shanks, 1955; Dyke, 1964). As evident from the second and third rows of Fig. 5.2, the influence of base flow perturbations is concentrated at an

energetically relevant region of the energy spectrum with a maximum at streamwise and spanwise wavenumbers that are slightly higher than those corresponding to the peak of the nominal premultiplied energy spectrum (Fig. 5.2(a)). Similar to the results presented in the previous chapter, stochastic base flow perturbation cannot influence streamwise streaks, which is because of the structure of $A_u(\mathbf{k})$ at $k_x = 0$; see Appendix C. Finally, as shown in Fig. 5.3, the total effect of stochastic base flow uncertainty of various amplitude, which can be quantified as $\int_{\mathbf{k}} E_c(\mathbf{k}) d\mathbf{k} / \int_{\mathbf{k}} E_0(\mathbf{k}) d\mathbf{k}$, follows a similar trend to what was observed for laminar flows (cf. Fig. 4.7).

5.3 Maximally affected flow structures

For a turbulent channel flow with $R_\tau = 186$, we follow a similar procedure as chapter 4.3 in analyzing the flow structures that are influenced by base flow perturbations with $f(y) = \bar{U}(y)/|\bar{U}(y)|$, $\alpha = 1$, and the critically stable variance $\sigma_u^2 = 0.7$. Figure 5.4 shows the contribution of the first eight eigenvalues of $\Phi(\mathbf{k})$ to the kinetic energy at the wavenumber pair corresponding to the maximum amplification in Fig. 5.2(e), i.e., $(k_x, k_z) = (1.86, 1.94)$. Base flow perturbations significantly increase the dominance of the principal eigenvalue (from 22% of the total energy in the unperturbed state to approximately 36%). Figure 5.5 depicts the flow structures corresponding to the streamwise component of the most significant eigenmode in the absence and presence of streamwise base flow perturbations. It is evident that base flow perturbations shift the core of these energetic flow structures along with the counter-rotating vortical structures away from the wall.

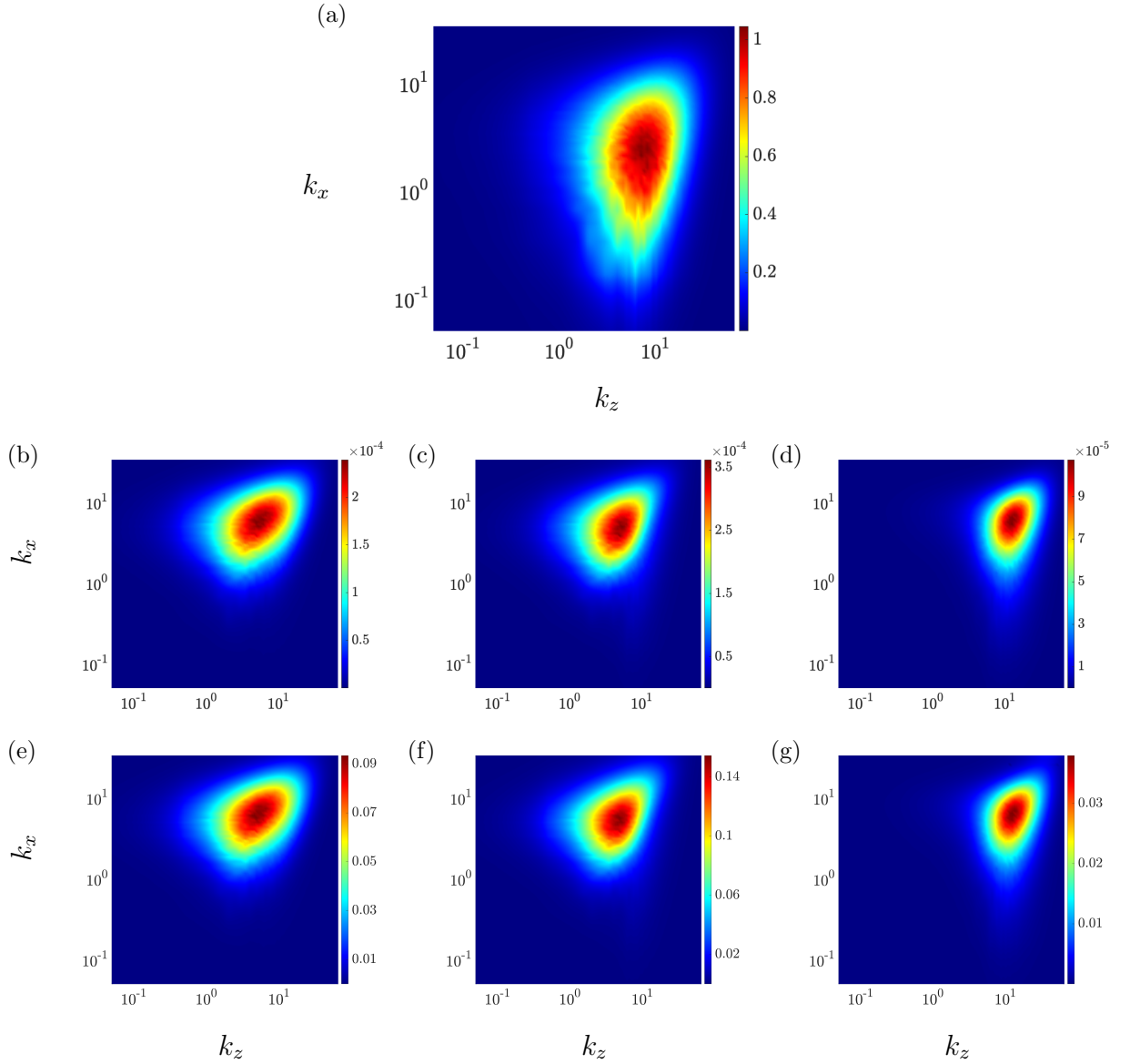


Figure 5.2. (a) Premultiplied energy spectrum of turbulent channel flow with $R = 186$ in the absence of stochastic base flow perturbations ($E_0(\mathbf{k})$). Correction to the premultiplied energy spectra $E_c(\mathbf{k})$ of turbulent channel flow $R = 186$ due to stochastic multiplicative uncertainty γ_u with variance $\sigma_u^2 = 0.13$ and perturbation amplitudes $\alpha = 0.05$ (second row) and $\alpha = 0.9$ (third row) that follow perturbations shapes $f(y) = \bar{U}(y)/|\bar{U}(y)|$ (b, e), $f(y)$ in Fig. 2.1(a) (c, f), and $f(y)$ in Fig. 2.1(b) (d, g).

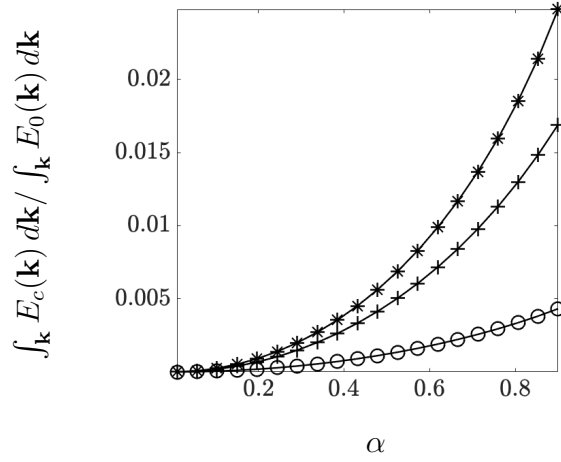


Figure 5.3. The total effect of stochastic perturbations of amplitude α on the energy spectrum of turbulent channel flow with $R_\tau = 186$. The curves demonstrate the α dependence of the energy correction due to base flow perturbations entering the dynamics through $f(y) = \bar{U}(y)/|\bar{U}(y)|$ (+), or the shape functions $f(y)$ depicted in Figs. 2.1(b) (o) and 2.1(a) (*).

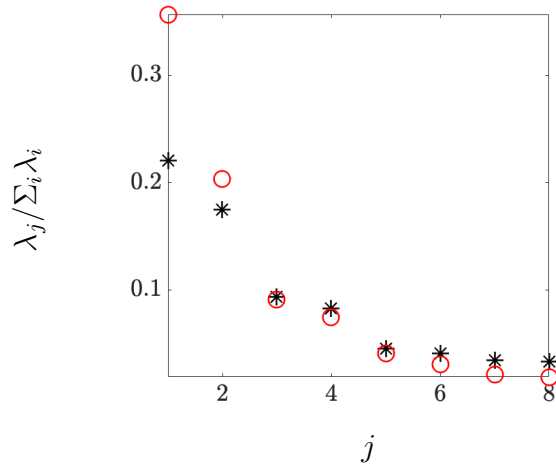


Figure 5.4. Contribution of the first eight eigenvalues of the velocity covariance matrix Φ of channel flow in the absence (*), and presence (o) of base flow perturbations with $f(y) = \bar{U}(y)/|\bar{U}(y)|$ and amplitude $\alpha = 1$ in turbulent channel flow with $R_\tau = 186$ at $(k_x, k_z) = (1.86, 1.94)$.

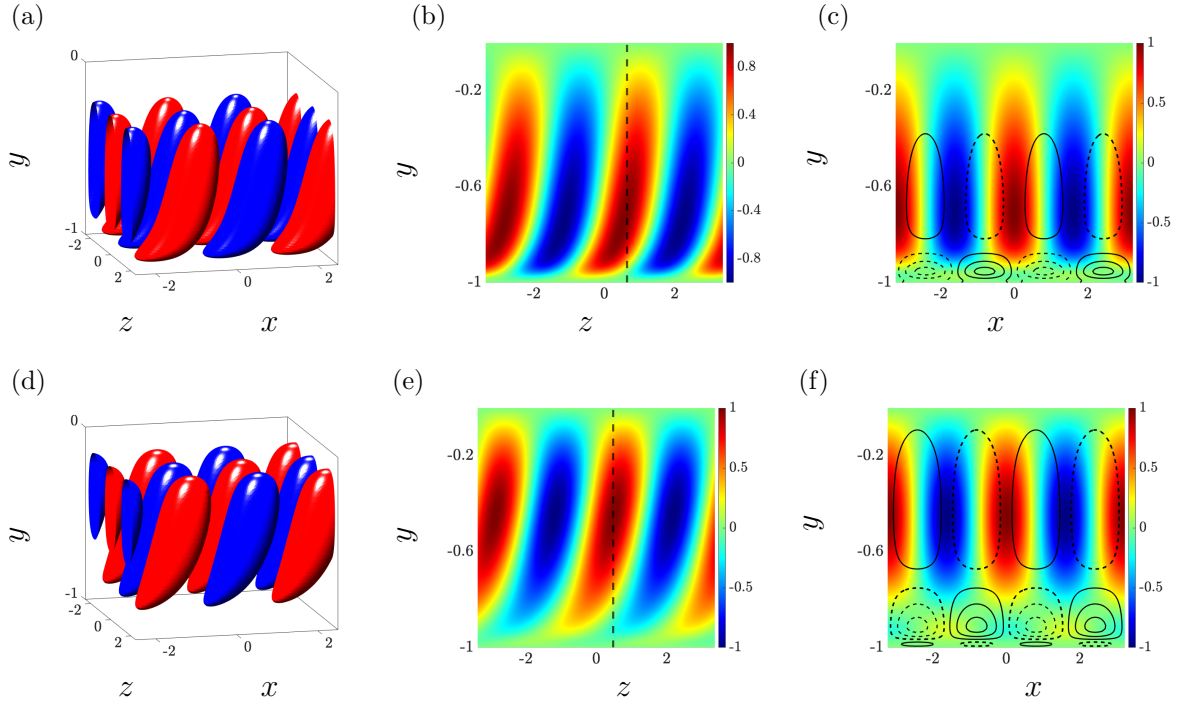


Figure 5.5. The streamwise component of the dominant flow structures of turbulent channel flow with $R_\tau = 186$ and $(k_x, k_z) = (1.86, 1.94)$ in the absence and (first row) and presence (second row) of stochastic base flow perturbations of amplitude $\alpha = 1$, shape $f(y) = \bar{U}(y)/|\bar{U}(y)|$, and variance $\sigma_u^2 = 0.49$. The three columns correspond to: (left) the spatial structure of the eigenmodes with red and blue colors denoting regions of high and low velocity; (middle) the streamwise velocity at $z = 0$; and (right) the $y - z$ slice of streamwise velocity (color plots) and vorticity (contour lines) at the streamwise location indicated by the dashed vertical lines in the middle panel ($x = 0.6$).

CHAPTER 6

REYNOLDS NUMBER DEPENDENCE

In this chapter, we analyze the Reynolds number dependence of the energy spectrum of streamwise constant velocity fluctuations ($k_x = 0$) around parallel base flow profiles subject to streamwise perturbations $\bar{\gamma}_u$. For any finite R , we assume the dynamics of such fluctuations to be MSS. Theorem 1 establishes an explicit Reynolds number scaling for the energy spectrum $E(k_z)$ of streamwise constant fluctuations in channel flow subject to streamwise base flow uncertainty.

Theorem 1. *The variance amplification of streamwise constant velocity fluctuations in channel flow with nominal velocity $\bar{U}(y)$ subject to base flow perturbations is given by,*

$$E(k_z) = f(k_z) R + g(k_z) R^2 + h(k_z) R^3 \quad (6.1)$$

where functions f , g , and h are independent of R .

A proof for this theorem is provided in Appendix D where it is shown that functions f , g and h represent traces of the solutions to Lyapunov equations which scale as R , R^2 , and R^3 , respectively. The function f does not depend on $\bar{U}(y)$ and is thus the same for all parallel channel flows. On the other hand, functions g and h depend on the underlying parallel base flow due to their dependence on the nominal shear $\bar{U}'(y)$. In nominal conditions, the energy spectrum of streamwise constant velocity fluctuations of a parallel channel flow can be decomposed into two components that scale with R and R^3 (Jovanovic and Bamieh, 2005, Corollary 4). The effect of base flow uncertainty is exclusively captured by the function g , which introduces a R^2 scaling to the energy spectrum of velocity fluctuations; see Appendix D for details. In a similar manner, Theorem 2 uses a perturbation analysis to elucidate the Reynolds number dependence of changes to the energy content of streamwise elongated structures when the amplitude of base flow perturbations is small.

Theorem 2. *The variance amplification of streamwise constant velocity fluctuations in channel flow with nominal velocity $\bar{U}(y)$ subject to small-amplitude base flow perturbations is given by,*

$$E(k_z) = E_0(k_z) + \alpha^2 E_2(k_z) + O(\alpha^4),$$

where

$$E_0(k_z) = f(k_z) R + h(k_z) R^3, \quad E_2(k_z) = g(k_z) R^2.$$

The term E_0 denotes the nominal energy, E_2 captures the effect of base flow perturbations at the level of α^2 , and functions f , g , and h are independent of R .

A proof for this theorem is provided in Appendix E. Note that for $\alpha = 1$, the functions f , g and h are the same in both Theorems. It is also evident that unless the amplitude α of base flow perturbation is significantly large, the energetic contribution of $h(z)R^3$ will dominate the energy of streamwise constant flow fluctuations especially at high Reynolds numbers.

Figure 6.1 illustrates the k_z dependence of functions f , g , and h for streamwise constant laminar channel flow subject to both white-in-time exogenous excitation and white-in-time base flow perturbations with $f(y) = \bar{U}(y)/|\bar{U}(y)|$. As explained above, and shown in Appendices D and E, the function f is independent of the choice of base flow, and is thus, identical for both Couette and Poiseuille flows; see Fig. 6.1(a). Figure 6.1(b) shows the dependence of h on the spanwise wavenumber k_z for Couette flow with $R = 500$ and Poiseuille flow with $R = 2000$. For both flows, the function h , which corresponds to the dominant Reynolds number scaling ($O(R^3)$) at high Reynolds numbers, peaks at around the same spanwise wavenumbers ($k_z = 1.59$ and 2.09 in Couette and Poiseuille flows, respectively) as their nominal spectral energy peak (cf. Fig. 4.3). In the presence of streamwise base flow perturbations $\bar{\gamma}_u$ with $\alpha = 1$ and variance levels corresponding to the critical variances obtained

from Fig. 4.2 at $k_x = 0$, the energy of streamwise constant fluctuations is complemented with the additional term g , which scales as R^2 . Figure 6.1(c) shows the k_z dependence of this function for Couette and Poiseuille flows. The spanwise wavenumbers at which the function g peaks for these two flows ($k_z = 1.91$ and 3.02 , in Couette and Poiseuille flows, respectively) is in agreement with the energy spectra in Figs. 4.6(a) and 4.6(b) for $k_x \approx 0$. To further elucidate the dependence of g on the variance of streamwise base flow perturbations, we compute this function for various spanwise wavenumbers k_z and a range of variances σ_u^2 for which MSS is guaranteed; see Fig. 6.2. As shown in Fig. 6.2, for the range of considered variances, the dependence of g on k_z predominantly follows the trends observed in Fig. 6.1(c).

A similar analysis can be conducted on the Reynolds dependence of the energy spectrum in a streamwise constant turbulent channel flow subject to both white-in-time exogenous excitation and white-in-time stochastic base flow perturbations. Figure 6.3(a) shows the variations of functions f , g , and h on the spanwise wavenumber k_z and perturbation variances σ_u^2 . As shown in Figs. 6.3(a) and 6.3(b), the k_z -dependence of functions f and h follow similar trends as was shown in Figs. 6.1(a) and 6.1(b) for transitional flows. Figure 6.3(c) shows the k_z -dependence of g when stochastic base flow perturbations with $f(y) = \bar{U}(y)/|\bar{U}(y)|$, $\alpha = 1$, and the maximum tolerable variance $\sigma_u^2 = 62.5$ corresponding to the streamwise constant wavenumber pair $(k_x, k_z) = (0, 0.01)$ are introduced into the turbulent channel flow with $k_x = 0$. The effect of uncertainty in the base flow of the turbulent channel flow is captured by the function g with a peak at $k_z = 50.22$ (Fig. 6.3(c)). Moreover, Fig. 6.3(d) illustrates the dependence of g on the variance of base flow perturbations σ_u^2 at various spanwise wavenumbers. In contrast to transitional flows, the function g monotonically increases as the spanwise wavenumber grows.

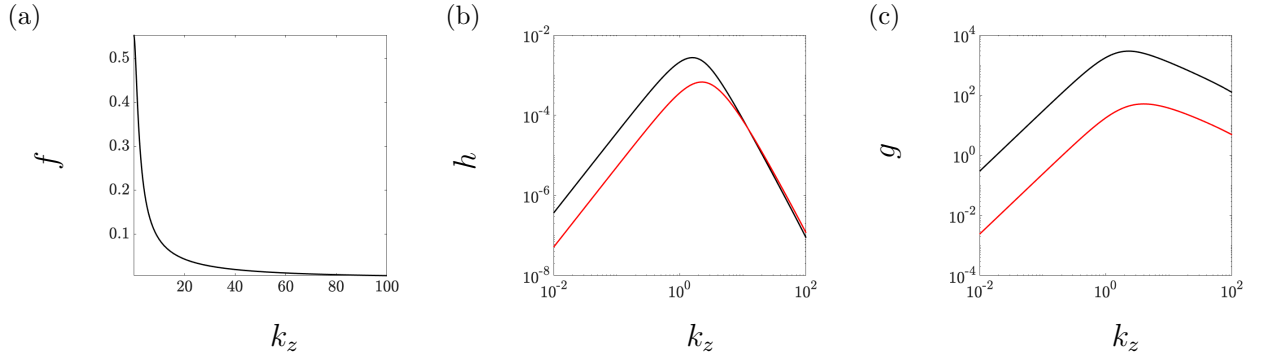


Figure 6.1. The k_z -dependence of functions (a) f , (b) h , and (c) g in Eq. (6.1) for Couette flow with $R = 500$ (—) and Poiseuille flow with $R = 2000$ (—) subject to base flow perturbations of shape $f(y) = \bar{U}(y)/|\bar{U}(y)|$ of variance $\sigma_u^2 = 1.13 \times 10^5$ and $\sigma_u^2 = 3.22 \times 10^3$, respectively. The function f , which is responsible for the $O(R)$ energy amplification is the same for both channel flows.

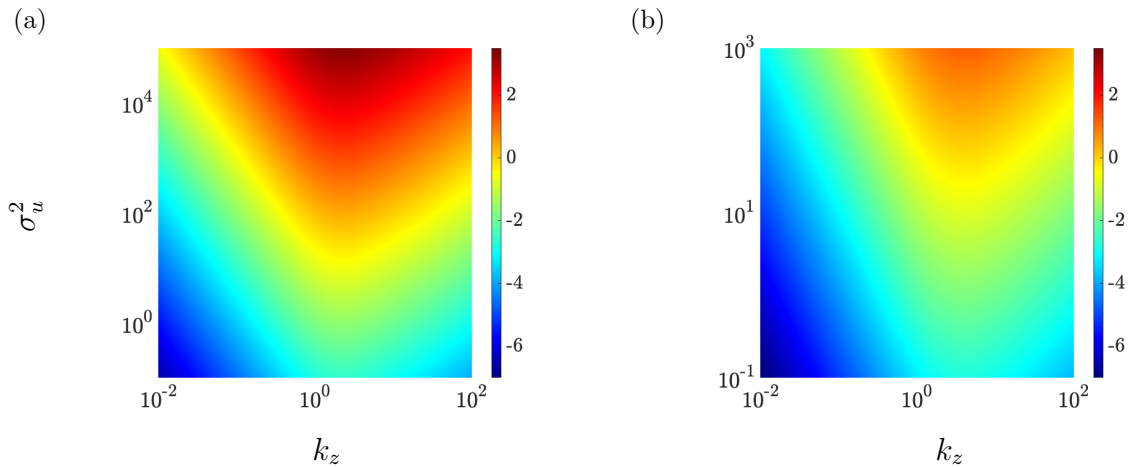


Figure 6.2. Logarithmically scaled terms that are responsible for the $O(R^2)$ energy amplification in Eq. (6.1) ($\log_{10}(g(k_z, \sigma_u^2))$) as a function of spanwise wavenumber k_z and base flow perturbation variance σ_u^2 . Perturbations to the base flow follow $f(y) = \bar{U}(y)/|\bar{U}(y)|$. (a) Couette flow with $R = 500$; and (b) Poiseuille flow with $R = 2000$.

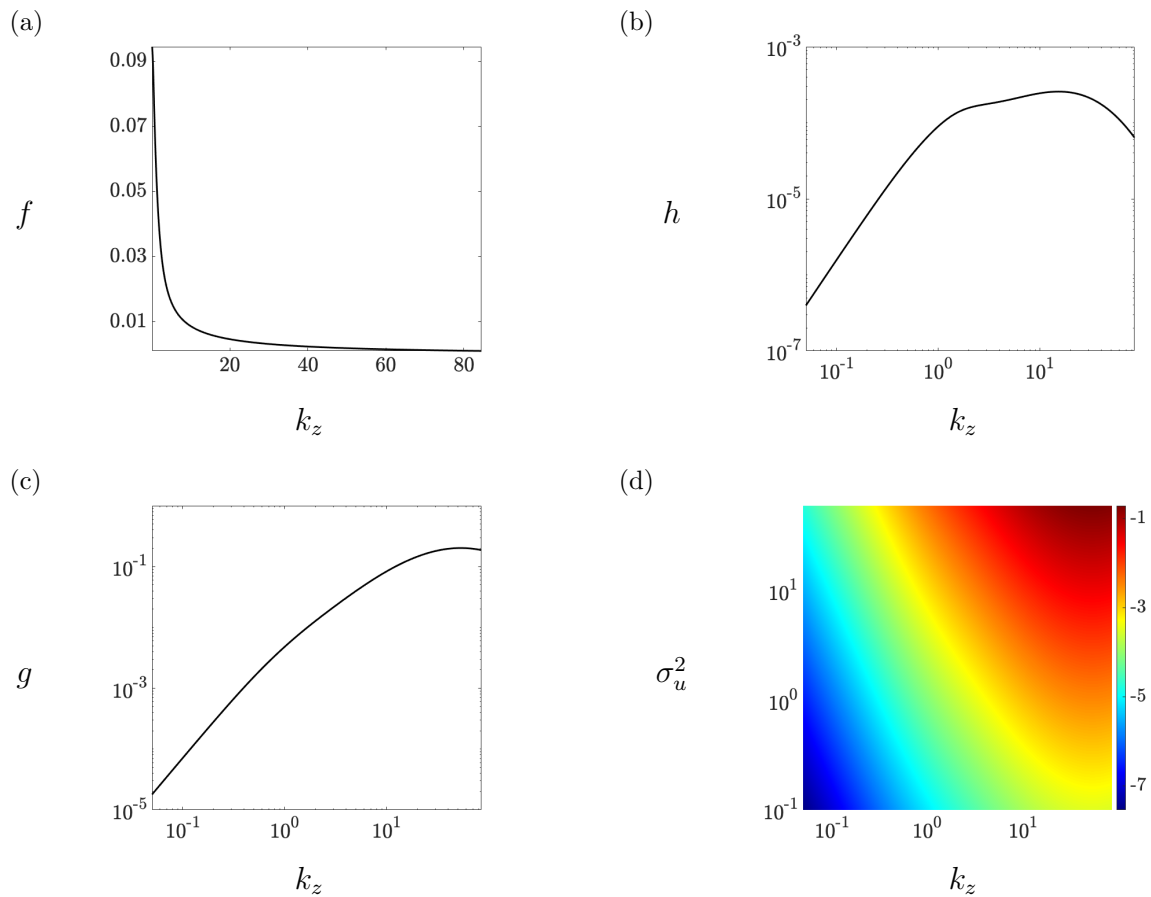


Figure 6.3. The k_z -dependence of functions (a) f , (b) h , and (c) g in Eq. (6.1) for turbulent flow with $R = 186$ subject to base flow perturbations of shape $f(y) = \bar{U}(y)/|\bar{U}(y)|$ and variance $\sigma_u^2 = 62.5$. (d) The logarithmically scaled term responsible for the $O(R^2)$ energy amplification in Eq. (6.1) ($\log_{10}(g(k_z, \sigma_u^2))$) as a function of spanwise wavenumber k_z and base flow perturbation variance σ_u^2 .

CHAPTER 7

EFFECT OF PARAMETRIC UNCERTAINTIES ON THE PERFORMANCE OF TRANSVERSE WALL OSCILLATIONS

Carefully designed transverse wall oscillations, as a flow control strategy, have been shown to reduce the receptivity of wall-bounded flows to exogenous disturbances, suppress energy of velocity fluctuations, and reduce skin-friction drag by 40%. However, experimental (Choi, 2002; Ricco, 2004), numerical (Jung et al., 1992; Quadrio and Ricco, 2004), and theoretical studies (Ricco and Quadrio, 2008; Jovanovic, 2008; Moarref and Jovanovic, 2012; Zare et al., 2012; Zare, 2016) have demonstrated that the efficacy of this flow control strategy depends on a critical selection of design parameters, e.g., amplitude and frequency (Jovanovic, 2008). This motivates the development of a complementary framework for analyzing the robust performance of such vibrational control strategies that are prone to parametric uncertainties resulting from implementation and modeling imperfections.

In this chapter, we use the theoretical developments in chapter 3 to evaluate the robust performance of transverse wall oscillations in suppressing the energy of velocity fluctuations in a channel flow with $R = 2000$. We consider a Poiseuille flow subject to lower-wall transverse sinusoidal oscillations of amplitude α and frequency ω_t that take the form $2\alpha(1 + \gamma_\alpha) \sin(\omega_t t + \gamma_\theta)$; see Fig. 7.1(a). The amplitude of wall oscillations is multiplied by 2 for convenience of algebraic manipulations, and $\gamma_\alpha(t)$ and $\gamma_\theta(t)$ denote independent sources of white-in-time stochastic uncertainty with mean and variance pairs given by $\{\mu_\alpha, \sigma_\alpha^2\}$ and $\{\mu_\theta, \sigma_\theta^2\}$, respectively. Note that $\gamma_\alpha(t)$ and $\gamma_\theta(t)$ are not required to have zero mean. These parametric uncertainties model imperfections in the amplitude and phase of oscillations and they effectively result in random lower-wall oscillations; see Fig. 7.1(b) for an illustration. We first compute the base flow in the presence of uncertainty. Then, we use the MSS analysis

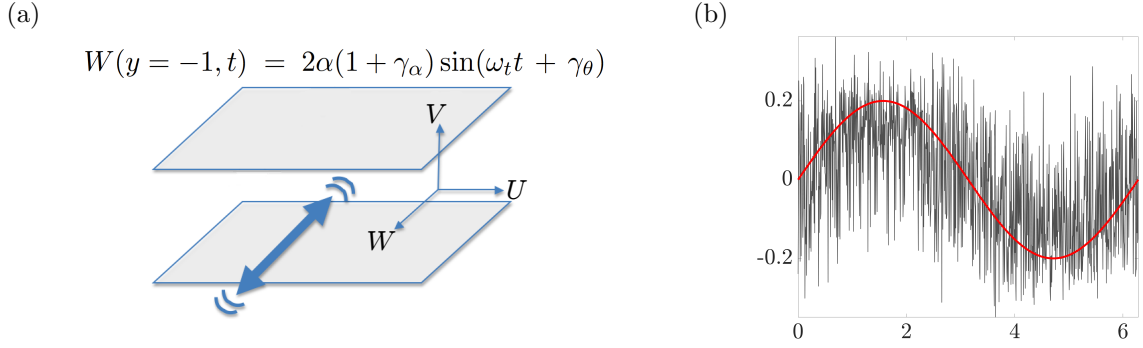


Figure 7.1. (a) Channel flow subject to transverse wall oscillations with amplitude and phase imperfections; and (b) Boundary condition on spanwise velocity due to stochastic processes $\gamma_\alpha \sim \mathcal{N}(0, 0.1)$ and $\gamma_\theta \sim \mathcal{N}(0, 1)$ (gray); see Eqs. (7.1). The amplitude and frequency of the nominal sinusoidal oscillation are given by $\alpha = 0.1$ and $\omega_t = 1$ (red).

of Sec. 3.2 and the input-output analysis of Sec. 3.3 to study the stability features of the uncertain base flow and the energy of velocity fluctuations, respectively.

7.1 Dynamics of velocity fluctuations in the presence of random wall oscillations

The base flow $\bar{\mathbf{u}} = [U \ V \ W]^T$ in a pressure-driven channel flow over transverse wall oscillations can be obtained by solving the steady-state NS equations subject to

$$\begin{aligned} U(\pm 1) &= V(\pm 1) = V_y(\pm 1) = W(+1) = 0 \\ W(-1) &= 2\alpha(1 + \gamma_\alpha) \sin(\omega_t t + \gamma_\theta) \end{aligned} \quad (7.1)$$

Due to these boundary conditions, the equations that govern the dynamics of the base flow can be simplified into a pair of decoupled partial differential equations

$$0 = -\bar{P}_x + (1/R) U_{yy} \quad (7.2a)$$

$$W_t = (1/R) W_{yy} \quad (7.2b)$$

where $\bar{P}_x = -2/R$ denotes the nominal pressure gradient in Poiseuille flow. The steady-state solution to (7.1) and (7.2) is given by $\bar{\mathbf{u}} := [U(y) \ 0 \ W(y, t)]^T$, where

$$U(y) = 1 - y^2 \quad (7.3a)$$

$$W(y, t) = \alpha \left[(1 + \gamma_{+1}) W_{+1}(y) e^{i\omega t} + (1 + \gamma_{-1}) W_{-1}(y) e^{-i\omega t} \right] \quad (7.3b)$$

Here, $\gamma_{\pm 1} := (1 + \gamma_\alpha) e^{\pm i\gamma_\theta} - 1$ are white-in-time stochastic uncertainties that capture the combined effects of parametric uncertainties and white-in-time stochastic uncertainties that capture the combined effects of γ_α and γ_θ on the base state, and $W_{\pm 1}(y)$ are solutions of a system of differential equations; see Appendix F for the mean and variance of $\gamma_{\pm 1}$ and Appendix G for details on how to obtain $W_{\pm 1}(y)$. This renders the evolution model 2.9 time-periodic with operator-valued dynamic matrix

$$\mathbf{A}(\mathbf{k}, t) = \bar{\mathbf{A}}(\mathbf{k}, t) + \alpha \left[\gamma_{+1} \mathbf{A}_{+1}(\mathbf{k}) e^{i\omega t} + \gamma_{-1} \mathbf{A}_{-1}(\mathbf{k}) e^{-i\omega t} \right] \quad (7.4)$$

where

$$\bar{\mathbf{A}}(\mathbf{k}, t) = \mathbf{A}_0(\mathbf{k}) + \alpha \left[(1 + \mu_{+1}) \mathbf{A}_{+1}(\mathbf{k}) e^{i\omega t} + (1 + \mu_{-1}) \mathbf{A}_{-1}(\mathbf{k}) e^{-i\omega t} \right] \quad (7.5)$$

and expressions for \mathbf{A}_0 , \mathbf{A}_1 , and \mathbf{A}_{-1} are provided in Appendix H. Here, we have explicitly accounted for the dynamic drift caused by the mean values of white-in-time uncertainties $\gamma_{\pm 1}$, i.e., $\mu_{\pm 1}$, by including a constant modification to the coefficients of the otherwise purely time-periodic deterministic dynamics $\bar{\mathbf{A}}(\mathbf{k}, t)$.

7.2 MSS conditions and Frequency response analysis

The MSS conditions follow the developments of Sec. 3.2 with $\Gamma = \text{diag}\{\sigma_u^2 \mathbf{1}\mathbf{1}^T, \sigma_w^2 \mathbf{1}\mathbf{1}^T\}$ and

$$B_0(\mathbf{k}) := \begin{bmatrix} I & I \end{bmatrix}, \quad C_0(\mathbf{k}) := \begin{bmatrix} A_{-1}(\mathbf{k}) e^{-i\omega t} \\ A_{+1}(\mathbf{k}) e^{+i\omega t} \end{bmatrix}.$$

The impulse response $M(\mathbf{k}, t)$ in (3.2) corresponding to the state-space representation (3.3) will inherit the time-periodicity of the nominal dynamics $\bar{A}(\mathbf{k}, t)$ (cf. (7.5)). Due to this time-periodicity, the response vectors to stationary white input processes are cyclo-stationary (Gardner, 1990), i.e., their statistical properties are periodic in time. For example, the covariance of $\boldsymbol{\psi}$ is given by

$$\begin{aligned} X(\mathbf{k}, t) &= \langle \boldsymbol{\psi}(\mathbf{k}, t) \boldsymbol{\psi}^*(\mathbf{k}, t) \rangle \\ &= X_0(\mathbf{k}) + X_1(\mathbf{k}) e^{i\omega t} + X_1^*(\mathbf{k}) e^{-i\omega t} + X_2(\mathbf{k}) e^{2i\omega t} + X_2^*(\mathbf{k}) e^{-2i\omega t} + \dots \end{aligned} \quad (7.6)$$

Moreover, the average effect of additive and multiplicative sources of excitation (over one period of wall oscillations T) is determined by X_0 , i.e.,

$$\frac{1}{T} \int_0^T X(\mathbf{k}, t) dt = X_0(\mathbf{k}) \quad (7.7)$$

and the energy spectrum of velocity fluctuations \mathbf{v} is given by

$$E(\mathbf{k}) = \text{trace}(X_0(\mathbf{k})). \quad (7.8)$$

In the lifted space of bi-infinite harmonic expansions, the state of system (3.3) is represented as a bi-infinite column vector of Fourier coefficients, i.e., $\text{col}\{\hat{\boldsymbol{\psi}}_n(\mathbf{k}, \theta)\}_{n \in \mathbb{Z}}$, with covariance

$$\mathcal{X}(\mathbf{k}) = \text{Toep} \left\{ \dots, X_2^*, X_1^*, \boxed{X_0}, X_1, X_2, \dots \right\} \quad (7.9)$$

where the box denotes the block on the main diagonal of \mathcal{X} . Note that the elements in the block-Toeplitz matrix \mathcal{X} correspond to the components in the Fourier expansion (7.6). When $\tilde{\mathbf{f}}$ and $\tilde{\gamma}_i$ are zero-mean white-in-time processes with covariance matrix Ω and variance σ_i^2 , the covariance matrix \mathcal{X} can be obtained by solving the following generalized Lyapunov equation

$$\bar{\mathcal{F}} \mathcal{X} + \mathcal{X} \bar{\mathcal{F}}^* + \sum_{i=\pm 1} \sigma_i^2 \mathcal{F}_i \mathcal{X} \mathcal{F}_i^* = -\mathcal{B} \Omega \mathcal{B}^* \quad (7.10a)$$

$$\bar{\mathcal{F}} := \bar{\mathcal{A}} - \mathcal{E}(0) \quad (7.10b)$$

$$\mathcal{F}_i := \mathcal{A}_i \quad (7.10c)$$

which is parameterized over wavenumber pairs \mathbf{k} . Here, \mathcal{B} , \mathcal{Q} , and \mathcal{E} are bi-infinite block-diagonal matrices,

$$\mathcal{B}(\mathbf{k}) := \text{diag} \{ B(\mathbf{k}) \}_{n \in \mathbb{Z}}$$

$$\mathcal{Q}(\mathbf{k}) := \text{diag} \{ \Omega(\mathbf{k}) \}_{n \in \mathbb{Z}}$$

$$\mathcal{E}(\theta) := \text{diag} \{ i(\theta + n\omega_t) I \}_{n \in \mathbb{Z}}$$

where $\bar{\mathcal{A}}$ and \mathcal{A}_i are bi-infinite block-Toeplitz matrices that represent the lifted variants of the nominal and uncertain components of the dynamics (cf. Eqs. (7.4) and (7.5)), respectively, i.e.,

$$\bar{\mathcal{A}} := \text{Toep} \left\{ \dots, 0, \alpha(1 + \mu_{+1}) A_{+1}, \boxed{A_0}, \alpha(1 + \mu_{-1}) A_{-1}, 0, \dots \right\}$$

$$\mathcal{A}_{+1} := \text{Toep} \left\{ \dots, 0, \alpha A_{+1}, \boxed{0}, 0, \dots \right\}$$

$$\mathcal{A}_{-1} := \text{Toep} \left\{ \dots, 0, \boxed{0}, \alpha A_{-1}, 0, \dots \right\}$$

At any pair of horizontal wavenumbers \mathbf{k} , a discretization of the linearized NS equations together with a truncation of the aforementioned bi-infinite dynamic matrices would require solving a large-scale generalized Lyapunov equation. We follow (Moarref and Jovanovic, 2012) in considering small-amplitude wall oscillations α , which allows us to utilize a perturbation analysis to solve the generalized Lyapunov equation (7.10) and achieve a computationally efficient way of computing the energy spectrum. In addition to the computational benefit, this choice of wall oscillation amplitude is motivated by the observation that large-amplitude oscillations can become prohibitively expensive to generate and result in a negative net efficiency for our flow control strategy (Ricco and Quadrio, 2008; Moarref and Jovanovic, 2012). As shown in Appendix I, this approach allows us to compute the second-order statistics of the uncertain model by solving a sequence of standard algebraic Lyapunov equations instead of the generalized Lyapunov equation (7.10). Up to a second

order in α , the zeroth-order harmonic X_0 that is required for computing the energy spectrum (Eq. (7.8)) is given by

$$X_0(\mathbf{k}) = X_{0,0}(\mathbf{k}) + \alpha^2 X_{0,2}(\mathbf{k}) + O(\alpha^4) \quad (7.11)$$

where $X_{0,0}$ and $X_{0,2}$ are obtained from a set of decoupled Lyapunov equations; see Appendix I for details. Note that $X_{0,0}$ represents the steady-state covariance matrix of the stochastically forced plane channel flow (no control) and $X_{0,2}$ represents the second-order correction induced by the random wall oscillations. The energy spectrum of velocity fluctuations follows a similar perturbation series:

$$E(\mathbf{k}) = E_0(\mathbf{k}) + \alpha^2 E_2(\mathbf{k}) + O(\alpha^4) \quad (7.12)$$

where $E_0(\mathbf{k}) = \text{trace}(X_{0,0}(\mathbf{k}))$ is the energy spectrum in the absence of control, and $E_2(\mathbf{k}) = \text{trace}(X_{2,0}(\mathbf{k}))$ captures the effect of boundary control at the level of α^2 .

7.3 MSS and variance amplification in channel ow subject to random lower-wall oscillations

For a Poiseuille flow with $R = 2000$, we evaluate the influence of parametric uncertainties on the MSS of the flow and robust performance of lower-wall oscillations in suppressing turbulence. Throughout this section, we use $N = 101$ Chebyshev collocation points to discretize the operators involved in the linearized equations. Grid convergence is ensured by doubling the number of collocation points. For $(k_x, k_z) = (0, 2)$ and various nominal wall oscillation parameters (α and ω_t), we evaluate the MSS of the controlled flow dynamics in the presence of zero-mean stochastic parametric uncertainties γ_α and γ_θ . The choice of horizontal wavenumber pair is motivated by the fact that in the absence of control, the energy spectrum of velocity fluctuations in plane Poiseuille flow with $R = 2000$ can be shown to peak at $k_x = 0$ and $k_z \approx 1.78$ (see, e.g., (Jovanovic and Bamieh, 2005)), which corresponds

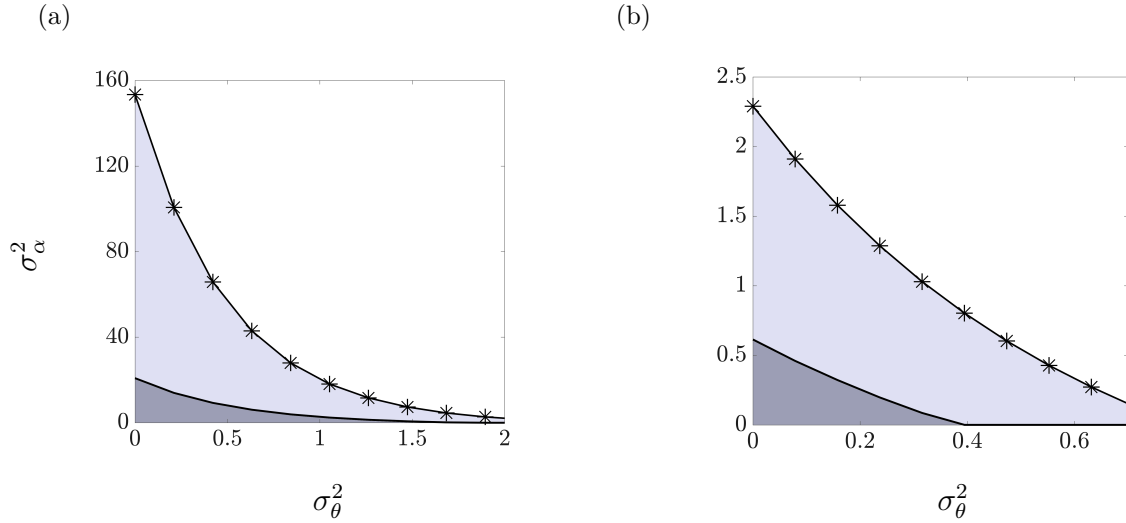


Figure 7.2. Stability curves for the dynamics of fluctuations in a channel flow with $R = 2000$ and $\mathbf{k} = (0, 2)$ subject to random lower-wall oscillations of frequency $\omega_t = 8.8 \times 10^{-3}$ (*) and $\omega_t = 5 \times 10^{-4}$ (—) with nominal oscillation amplitudes (a) $\alpha = 0.01$; and (b) $\alpha = 0.1$. The shaded areas under the curves correspond to variances of γ_α and γ_θ that do not violate MSS.

to the energetically dominant streamwise elongated streaks. While the first MSS condition, which is concerned with the stability of the nominal flow dynamics (\bar{A} Hurwitz), is satisfied no matter the uncertainty level, the second condition can be violated as the variances of γ_α and γ_θ grow. Figure 7.2 shows the regions of MSS in the presence of such uncertainties. The shaded areas under the curves denote the variances for which the flow remains asymptotically mean-square stable. While the MSS curves are specific to the choice of nominal parameters, it is evident that stability properties of the channel are more susceptible to parametric uncertainty entering in the phase of wall oscillations and that nominally larger oscillation amplitudes α and periods $T = 2\pi/\omega_t$ are less robust.

To study the effect of parametric uncertainties on the performance of our flow control strategy in reducing the energy of velocity fluctuations, we consider the case of wall oscillations with $\alpha = 0.01$ and $\omega_t = 8.8 \times 10^{-3}$ that are contaminated with zero-mean parametric uncertainties γ_α and γ_θ of variance 38 and 0.69, respectively. Based on Fig. 7.2, the linearized dynamics remain mean-square stable for these variance levels. Figure 7.3

shows the energy spectrum of velocity fluctuations in the absence (Fig. 7.3(a)) and presence (Fig. 7.3(b)) of lower-wall oscillations when $\gamma_\alpha = \gamma_\theta = 0$. These figures show that while the energetically dominant streamwise elongated structures with $k_z \sim 2$ are most attenuated, Tollmien–Schlichting (TS) waves ($k_z \sim 0$) become more energetically pronounced (by almost $O(1)$). Figure 7.3(c) shows that when the wall oscillations are contaminated with stochastic parametric uncertainties γ_α and γ_θ with variances $\sigma_u^2 = 38, 0.69$ respectively, the energy of velocity fluctuations amplifies across horizontal wavenumbers corresponding to streamwise elongated streaks that were previously suppressed in the absence of parametric uncertainty. It is also noteworthy that the amplification takes place even at shorter wave lengths causing more spanwise wavenumbers to reside in the energetically dominant streaks. Figures 7.3(d) and 7.3(e) illustrates the change in the total energy spectrum of velocity fluctuations when oscillations are contaminated with parametric uncertainty either in the phase or amplitude of oscillations. By such means, it can be observed that while uncertainty in phase can cause further suppression of streamwise elongated streaks due to lower-wall oscillations of the channel, it can result in the amplification of TS modes. On the other hand, when only wall oscillations carry uncertainty only in the phase of oscillations (cf. Fig. 7.3(d)), the streamwise elongated streaks sustain greater suppression compared to the suppression caused by nominal wall oscillations as opposed to an amplification in TS modes. For wall oscillations containing parametric uncertainty in the amplitude of oscillations (see Fig. 7.3(e))

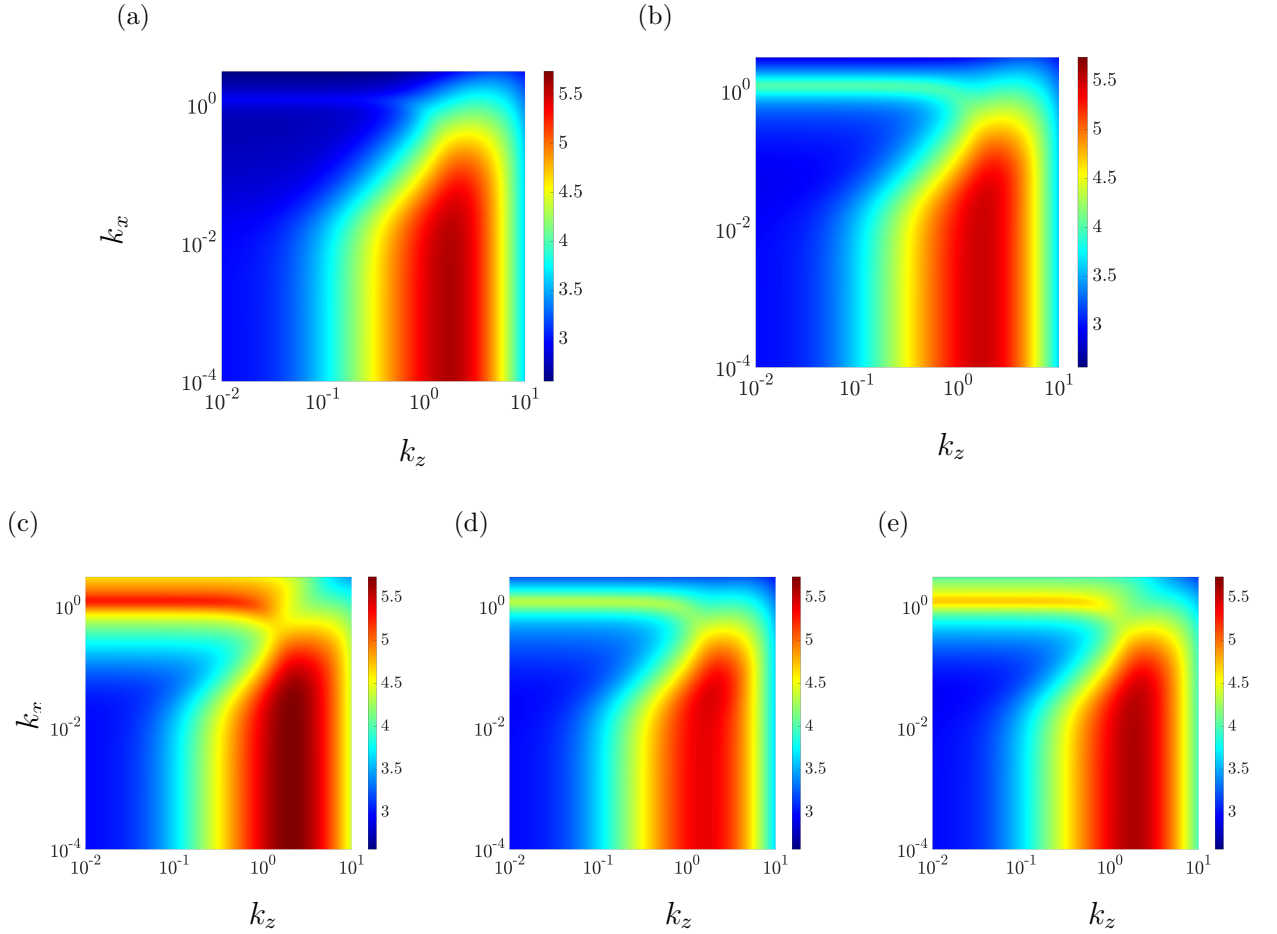


Figure 7.3. (a) Energy spectrum ($E_0(\mathbf{k})$) of the uncontrolled Poiseuille flow with $R = 2000$. Energy spectrum ($E(\mathbf{k})$) due to lower-wall oscillations with $\omega_t = 8.8 \times 10^{-3}$ up to the level of α^2 : (b) in the absence of zero-mean parametric uncertainty; and (c), (d), (e) in the presence of zero-mean parametric uncertainty with variances (c) $\sigma_\alpha^2 = 38$ and $\sigma_\theta^2 = 0.69$; (d) $\gamma_\alpha = 0$ and $\sigma_\theta^2 = 0.69$; (e) $\sigma_\alpha^2 = 38$ and $\gamma_\theta = 0$ of Poiseuille flow with $R = 2000$. The plots are given in log-log scale.

CHAPTER 8

CONCLUSION

In this thesis, we have developed an input-output framework for studying the influence of persistent stochastic base flow perturbations on the stability and energy content of velocity fluctuations in wall-bounded shear flows. We have provided verifiable conditions for the MSS of the linearized dynamics subject to stochastic base flow variations and have shown that the second-order statistics of fluctuations around the uncertain base state can be obtained as solutions to a generalized Lyapunov equation. We have used this framework to perform a thorough study of the effects of white-in-time structured stochastic base flow variations on transitional and turbulent channel flows. For transitional flows, the Reynolds number dependence of critical uncertainty variances uncovered by our method are in agreement with previously reported scaling laws for the magnitude of deterministic base flow variations. A similar power-law dependence with respect to the friction Reynolds number exists for the critical variance of stochastic perturbations to the DNS-based turbulent mean velocity of channel flows. We have shown that in both laminar and turbulent flows, shorter (in x) and wider (in z) wavelengths are least susceptible to base flow variations.

In laminar flow, while channel-wide base flow perturbations predominantly affect the oblique modes, especially those with $k_x \approx O(1)$ and $k_z \sim O(1)$, near-wall perturbations result in the dominant amplification of TS waves. Our results show that the amplification of streamwise elongated structures is relatively robust to base flow perturbations, especially if such perturbations are confined to the near-wall region of the flow. We have shown that the latter is due to the structure of dynamical perturbations induced by streamwise base flow variations at $k_x = 0$ and that streaks would also become susceptible to such sources of uncertainty if variations were allowed to enter other components of the base state. We demonstrate that large-amplitude base flow perturbations can influence the distribution of

energy among various length scales and lead to the dominance of flow structures that are significantly different from those that dominate the nominal flow. Notably, perturbations of the Poiseuille flow result in an increase in the energetic dominance of the principal mode that is excited by persistent stochastic excitations. In turbulent channel flow, base flow variations influence both oblique and streamwise elongated structures to a greater extent than two-dimensional TS modes. They also increase the wall-normal separation of dominant flow structures as well as their inclination to the wall. Regardless of their wall-normal extent, however, the effect of base flow perturbations on turbulent flow is significantly less than what is observed for laminar flows.

In addition to studying the dependence of the energy spectrum on spatial frequencies, we uncover the Reynolds number dependence of the energy of streamwise elongated fluctuations in the presence of streamwise base flow variations. We show that the contribution of base flow perturbations to the amplification of streamwise elongated flow structures scales as R^2 , which trails the R^3 scaling of energy amplification under nominal conditions. This scaling trend further explains the robust amplification of such flow structures, especially at high Reynolds numbers.

Our approach can also be used to study the effect of parametric uncertainties on the performance of boundary control strategies that reduce skin-friction drag or suppress turbulence by modulating the base state. To demonstrate this aspect, we have considered Poiseuille flow over transverse lower-wall oscillations with uncertain amplitude and phase. Our robustness analysis shows that despite a clear dependence of the stability curve on the nominal amplitude and frequency of oscillations, velocity fluctuations remain mean-square stable for relatively high levels of uncertainty, and that the detrimental effects of uncertainty on variance attenuation are negligible. This demonstrates the robust performance of lower-wall oscillations. Moreover, we have shown that even if such parametric uncertainties are zero-mean, they would translate into non-zero-mean multiplicative uncertainties in the linearized dynamics that shift the base state and affect counter intuitive changes in the energy

of velocity fluctuations. The second-order statistics of the velocity field are obtained from the solution of a large-size harmonic expansion of the generalized Lyapunov equation that cannot be solved using a direct vectorization procedure. To address this computational challenge, we have focused on small-amplitude wall oscillations and utilized a perturbation analysis over oscillation amplitudes to provide an efficient method for obtaining second-order flow statistics by solving a sequence of standard algebraic Lyapunov equations. Our approach provides the means for the robustness analysis of other flow control strategies that are prone to parametric uncertainties.

The utility of the proposed input-output framework in this study goes beyond the the analysis of streamwise base flow perturbations in laminar and turbulent flows. The framework allows for structured stochastic uncertainty to enter other components of the velocity field that may originate from exogenous sources that influence the long-time behavior of the flow, e.g., surface-mounted actuators or roughness elements. Given the influence of base flow variations on the second-order statistics of the linearized NS equations, it is also anticipated that the statistics of this source of multiplicative uncertainty can be shaped to model turbulence in wall-bounded flows. The development of a systematic framework for modeling turbulent flow statistics via stochastic base flow variations is a topic for future research that would directly uncover essential dynamical perturbations that account for the absence of nonlinear interactions in linearized models, see, e.g., (Zare et al., 2016, 2020) and (Zare et al., 2017, Sec. 6.1).

APPENDIX A

OPERATORS $\bar{\mathbf{A}}$, \mathbf{A}_u , AND \mathbf{A}_w FOR LAMINAR FLOW

Operators $\bar{\mathbf{A}}$, \mathbf{A}_u , and \mathbf{A}_w in Eq (2.8) are given by:

$$\bar{\mathbf{A}}(\mathbf{k}) = \begin{bmatrix} \mathbf{A}_{11} & 0 \\ \mathbf{A}_{21} & \mathbf{A}_{22} \end{bmatrix}$$

$$\mathbf{A}_{11}(\mathbf{k}) = \Delta^{-1} \left(\frac{1}{R} \Delta^2 + ik_x (\bar{U}'' - \bar{U} \Delta) + ik_z (\bar{W}'' - \bar{W} \Delta) \right)$$

$$\mathbf{A}_{21}(\mathbf{k}) = -ik_z \bar{U}' + ik_x \bar{W}',$$

$$\mathbf{A}_{22}(\mathbf{k}) = \frac{1}{R} \Delta - ik_x \bar{U} - ik_z \bar{W}$$

$$\mathbf{A}_u(y, t) = \begin{bmatrix} \Delta^{-1} ik_x (f_u'' - f_u \Delta) & 0 \\ -ik_z f_u' & -ik_x f_u \end{bmatrix}$$

$$\mathbf{A}_w(y, t) = \begin{bmatrix} \Delta^{-1} ik_z (f_w'' - f_w \Delta) & 0 \\ -ik_x f_w' & -ik_z f_w \end{bmatrix}.$$

APPENDIX B

**PERTURBATION ANALYSIS FOR SOLVING THE GENERALIZED
LYAPUNOV EQUATION**

The solution to (3.10) can be efficiently computed using a perturbation analysis in α . Following the form of the perturbed dynamical matrix A in Eq. (2.8), for sufficiently small α , the solution X can be expanded using the perturbation series,

$$X(\mathbf{k}) = X_0(\mathbf{k}) + \alpha X_1(\mathbf{k}) + \alpha^2 X_2(\mathbf{k}) + \dots \quad (\text{B.1})$$

Substituting (B.1) into Eq. (3.10) and collecting powers of α yields the sequence of standard algebraic Lyapunov equations,

$$\begin{aligned} \alpha^0 : \bar{A} X_0 + X_0 \bar{A}^* &= -B \Omega B^* \\ \alpha^n : \bar{A} X_n + X_n \bar{A}^* &= -[\delta(n-1) - 1] (\sigma_u^2 A_u X_{n-2} A_u^* + \sigma_w^2 A_w X_{n-2} A_w^*) \end{aligned} \quad (\text{B.2})$$

where $\delta(n)$ is the discrete delta function. Based on this perturbation expansion, $X_n = 0$ for odd values of n . This is because the right-hand-side of the algebraic Lyapunov equation is 0 for odd n . As a result, the structure identified for the steady-state covariance matrix X follows the perturbation series given in (3.12). For small-size perturbations similar to those considered in chapter 4, the limit of the perturbation series (3.13) can be obtained with one or two perturbation terms to E_0 . For large perturbations, the Shanks transformation can be used to overcome the problem of slow convergence or even divergence of the sequence; see (Shanks, 1955; Dyke, 1964; Wynn, 1966; Sidi, 2003) for additional details.

APPENDIX C

OPERATORS $\bar{\mathbf{A}}$ AND \mathbf{A}_u FOR TURBULENT FLOW

Operators $\bar{\mathbf{A}}$ and \mathbf{A}_u in Eq. (5.5), are given by:

$$\mathbf{A}(\mathbf{k}, t) := \begin{bmatrix} \mathbf{A}_{11} & 0 \\ \mathbf{A}_{21} & \mathbf{A}_{22} \end{bmatrix}$$

$$\mathbf{A}_{11}(\mathbf{k}, t) = \Delta^{-1} \left(\frac{1}{R_\tau} \left((1 + \nu_T) \Delta^2 + 2\nu'_T \Delta \partial_y + \nu''_T (\partial_y^2 + k^2) \right) + ik_x (\bar{U}'' - \bar{U} \Delta) \right)$$

$$\mathbf{A}_{21}(\mathbf{k}, t) = -ik_z \bar{U}', \quad \mathbf{A}_{22}(\mathbf{k}, t) = \frac{1}{R_\tau} \left((1 + \nu_T) \Delta + \nu'_T \partial_y \right) - ik_x \bar{U}$$

$$\mathbf{A}_u(y, t) = \begin{bmatrix} \Delta^{-1} ik_x (f_u'' - f_u \Delta) & 0 \\ -ik_z f_u' & -ik_x f_u \end{bmatrix}.$$

APPENDIX D

PROOF OF THEOREM 1

For streamwise constant channel flow ($k_x = 0$), the dynamic operators \bar{A} and A_u in Eq. (3.10) are given by,

$$\bar{A} = \begin{bmatrix} (1/R)\mathcal{L} & 0 \\ \mathcal{C}_p & (1/R)\mathcal{I} \end{bmatrix}, \quad A_u = \begin{bmatrix} 0 & 0 \\ -ik_z\gamma'_u(y, t) & 0 \end{bmatrix} \quad (\text{D.1})$$

where the operators \mathcal{L} , \mathcal{C}_p and \mathcal{I} are parametrized by the spanwise wavenumber k_z and the Reynolds number R . Moreover, assuming a solenoidal white-in-time exogenous excitation \mathbf{f} with covariance $\Omega = I$, we will have $B\Omega B^* = I$. Let the state covariance X take the form

$$X = \begin{bmatrix} X_1 & X_2 \\ X_2^* & X_3 \end{bmatrix}. \quad (\text{D.2})$$

Substituting this matrix together with those in (D.1) into Eq. (3.10) yields the set of coupled Sylvester equations:

$$\begin{aligned} \mathcal{L} X_1 + X_1 \mathcal{L}^* &= -R I \\ \mathcal{L} X_2 + X_2 \mathcal{I}^* &= -R X_1 \mathcal{C}_p^* \\ \mathcal{I} X_3 + X_3 \mathcal{I}^* &= -R (\mathcal{C}_p X_2 + X_2^* \mathcal{C}_p^* - \alpha^2 \sigma^2 k_z^2 \gamma'_u X_1 \gamma'_u + I). \end{aligned}$$

From these equations it is evident that X_1 and X_2 scale as R and R^2 , respectively, and as a result, X_3 will contain terms that scale with all orders $O(R)$, $O(R^2)$, and $O(R^3)$. Let $X_1 = R\tilde{X}_1$ and $X_3 = R\tilde{X}_{3,1} + R^2\tilde{X}_{3,2} + R^3\tilde{X}_{3,3}$. Thus, the variance amplification $E = \text{trace}(X)$ of streamwise constant fluctuations can be decomposed as

$$E = Rf + R^2g + R^3h$$

where $f := \text{trace}(\tilde{X}_1 + \tilde{X}_{3,1})$, $g := \text{trace}(\tilde{X}_{3,2})$, and $h := \text{trace}(\tilde{X}_{3,3})$.

APPENDIX E

PROOF OF THEOREM 2

For streamwise constant channel flow ($k_x = 0$), substituting the dynamic operators \bar{A} and A_u from Eq. (D.1) together with the perturbation series of the covariance matrix X (3.12) in its block operator form (cf. Eq. (D.2)) into Eq. (3.10) yields the set of coupled Sylvester equations:

$$\begin{aligned}\mathcal{L} X_{1,0} + X_{1,0} \mathcal{L}^* &= -R I \\ \mathcal{L} X_{2,0} + X_{2,0} \mathcal{J}^* &= -R X_{1,0} \mathcal{C}_p^* \\ \mathcal{J} X_{3,0} + X_{3,0} \mathcal{J}^* &= -R (\mathcal{C}_p X_{2,0} + X_{2,0}^* \mathcal{C}_p^* + I).\end{aligned}$$

at the level of α^0 , and

$$\mathcal{J} X_{3,2} + X_{3,2} \mathcal{J}^* = \sigma^2 k_z^2 R \gamma'_u X_{1,0} \gamma'_u.$$

at the level of α^2 . Here, we have assumed solenoidal white-in-time exogenous excitation \mathbf{f} with covariance $\Omega = I$, which yields $B\Omega B^* = I$, and $X_{i,j}$ denote the i th block (cf. (D.2)) of the j th term in the perturbation series (3.12). The nominal variance amplification can be computed as $E_0 = \text{trace}(X_0) = R f + R^3 h$ with functions f and h following the forms described in Appendix D, i.e., $f := \text{trace}(\tilde{X}_{1,0} + \tilde{X}_{3,0,1})$ and $h := \text{trace}(\tilde{X}_{3,0,3})$, where $X_{1,0} = R \tilde{X}_{1,0}$ and $X_{3,0} = R \tilde{X}_{3,0,1} + R^3 \tilde{X}_{3,0,3}$. On the other hand, since the exogenous forcing does not include a contribution at the level of α^2 , $X_{1,2} = X_{2,2} = 0$, $X_{3,2} = R^2 \tilde{X}_{3,2}$, and $E_2 = \text{trace}(X_2) = R^2 g$ with $g := \text{trace}(\tilde{X}_{3,2})$.

APPENDIX F

MEAN AND VARIANCE OF WHITE-IN-TIME STOCHASTIC

UNCERTAINTIE γ_1 AND γ_{-1}

Given mean and variance pairs $(\mu_\alpha, \sigma_\alpha^2)$ and $(\mu_\theta, \sigma_\theta^2)$ for the scalar-valued parametric uncertainties γ_α and γ_θ , we can compute the means and variances of γ_{+1} and γ_{-1} in Eq. (7.3)

as

$$\mu_{\pm 1} = \mathbf{E}[\gamma_{\pm 1}] = \mathbf{E}[1 + \gamma_\alpha] \mathbf{E}[e^{\pm i \gamma_\theta}] - 1 = (1 + \mu_\alpha) e^{\pm i \mu_\theta + \sigma_\theta^2/2} - 1$$

and

$$\begin{aligned} \sigma_{\pm 1}^2 &= \text{Var}(1 + \gamma_\alpha) (\text{Var}(e^{\pm i \gamma_\theta}) + \mathbf{E}[e^{\pm i \gamma_\theta}]^2) + \text{Var}(e^{\pm i \gamma_\theta}) \mathbf{E}[1 + \gamma_\alpha]^2 \\ &= e^{\pm 2i \mu_\theta + \sigma_\theta^2} \left(\sigma_\alpha^2 e^{\sigma_\theta^2} + (1 + \mu_\alpha)^2 (e^{\sigma_\theta^2} - 1) \right). \end{aligned}$$

APPENDIX G

FUNCTIONS $W_{+1}(y)$ AND $W_{-1}(y)$ IN A SYSTEM OF DIFFERENTIAL EQUATIONS IN THE PRESENCE OF RANDOM WALL OSCILLATIONS

Substituting Eq. (7.3b) under nominal conditions ($\gamma_{\pm 1} = 0$) into the the steady-state equations for spanwise velocity (7.2b) yields the system of ODEs

$$p''(y) = Gp(y); \quad p(+1) = 0, \quad p(-1) = b$$

with $p := [W_{+1} \quad W_{-1}]^T$, $b := [-i \quad i]^T$, and

$$G := \begin{bmatrix} i\omega_t R & 0 \\ 0 & -i\omega_t R \end{bmatrix}.$$

The solution, from which W_{+1} and W_{-1} can be extracted, only depends on y , ω_t , and R :

$$p(y) = (1 - N^{2y-2}) (N^{1+y} - N^{y-3})^{-1} b$$

where $N := e^{\sqrt{G}}$.

APPENDIX H

OPERATORS \mathbf{A}_0 , \mathbf{A}_{+1} , AND \mathbf{A}_{-1} IN THE DYNAMIC MATRIX OF THE SYSTEM WITH RANDOM WALL OSCILLATIONS

Operators \mathbf{A}_0 , \mathbf{A}_{+1} , and \mathbf{A}_{-1} are obtained by substituting W from Eq. (7.3b) into the expression (2.5) for \mathbf{A} :

$$\mathbf{A}_0 = \begin{bmatrix} \mathbf{A}_{0,11} & 0 \\ -ik_z U'(y) & \mathbf{A}_{0,22} \end{bmatrix}$$

$$\mathbf{A}_{0,11} = \Delta^{-1} \left(\frac{1}{R} \Delta^2 + ik_x (U''(y) - U(y)\Delta) \right)$$

$$\mathbf{A}_{0,22} = \frac{1}{R} \Delta - ik_x U(y)$$

$$\mathbf{A}_{-1} = \begin{bmatrix} \Delta^{-1} (ik_z (W''_{-1}(y) - W_{-1}(y)\Delta)) & 0 \\ ik_x W'_{-1}(y) & -ik_z W_{-1}(y) \end{bmatrix}$$

$$\mathbf{A}_{+1} = \begin{bmatrix} \Delta^{-1} (ik_z (W''_{+1}(y) - W_{+1}(y)\Delta)) & 0 \\ ik_x W'_{+1}(y) & -ik_z W_{+1}(y) \end{bmatrix}.$$

APPENDIX I

PERTURBATION ANALYSIS FOR SOLVING THE GENERALIZED

LYAPUNOV EQUATION IN THE PRESENCE RANDOM

WALL OSCILLATIONS

Following (Jovanovic and Fardad, 2008), the solution to (7.10) can be efficiently computed using a perturbation analysis in α . Specifically, the operator $\bar{\mathcal{F}}$ in (7.10) can be decomposed into a block diagonal operator $\bar{\mathcal{F}}_0$ and an operator $\bar{\mathcal{F}}_1$ that contains the first upper and lower block sub-diagonals

$$\bar{\mathcal{F}} = \bar{\mathcal{F}}_0 + \alpha \bar{\mathcal{F}}_1 \tag{I.1}$$

$$\bar{\mathcal{F}}_0 = \text{diag} \{A_0 - i n \omega_t I\}$$

$$\bar{\mathcal{F}}_1 = \text{Toep} \left\{ \dots, 0, (1 + \mu_{+1})A_{+1}, \boxed{0}, (1 + \mu_{-1})A_{-1}, 0, \dots \right\}.$$

Moreover, operators $\mathcal{F}_{\pm 1}$ take the block-Toeplitz form

$$\mathcal{F}_{+1} = \text{Toep} \left\{ \dots, 0, A_{+1}, \boxed{0}, 0, \dots \right\} \tag{I.2}$$

$$\mathcal{F}_{-1} = \text{Toep} \left\{ \dots, 0, \boxed{0}, A_{-1}, 0, \dots \right\}.$$

For sufficiently small α , the solution \mathcal{X} of (7.10) can be expanded using the same perturbation series,

$$\mathcal{X} = \mathcal{X}_0 + \alpha \mathcal{X}_1 + \alpha^2 \mathcal{X}_2 + \dots \tag{I.3}$$

Substituting (I.1)-(I.3) into (7.10) and collecting powers of α yields

$$\alpha^0 : \bar{\mathcal{F}}_0 \mathcal{X}_0 + \mathcal{X}_0 \bar{\mathcal{F}}_0^* = -B \Omega B^*$$

$$\alpha^n : \bar{\mathcal{F}}_0 \mathcal{X}_n + \mathcal{X}_n \bar{\mathcal{F}}_0^* = -(\bar{\mathcal{F}}_1 \mathcal{X}_{n-1} + \mathcal{X}_{n-1} \bar{\mathcal{F}}_1^*) + [\delta(n-1) - 1] \sum_{i=\pm 1} \sigma_i^2 \mathcal{F}_i \mathcal{X}_{n-2} \mathcal{F}_i^*$$

where $\delta(n)$ is the discrete delta function. Given the structures of $\bar{\mathcal{F}}_0$, $\bar{\mathcal{F}}_1$, and $\mathcal{F}_{\pm 1}$, we can determine the block structure of the self-adjoint operators \mathcal{X}_i in (I.3) as

$$\begin{aligned}\mathcal{X}_0 &:= \text{Toep}\left\{\dots, 0, \boxed{X_{0,0}}, 0, \dots\right\} \\ \mathcal{X}_1 &:= \text{Toep}\left\{\dots, 0, X_{1,1}^*, \boxed{0}, X_{1,1}, 0, \dots\right\} \\ \mathcal{X}_2 &:= \text{Toep}\left\{\dots, 0, X_{2,2}^*, 0, \boxed{X_{2,0}}, 0, X_{2,2}, 0, \dots\right\}\end{aligned}$$

where the first and second indices of the sub-matrices correspond to the perturbation order and harmonic number, respectively. The structure identified for the auto-correlation operators in conjunction with (7.7) and (7.9) results in the following perturbation series for X_0 :

$$X_0(\mathbf{k}) = X_{0,0}(\mathbf{k}) + \alpha^2 X_{2,0}(\mathbf{k}) + O(\alpha^4). \quad (\text{I.4})$$

Finally, the operators $X_{0,0}$ and $X_{2,0}$ are obtained by solving the following set of Lyapunov equations

$$\begin{aligned}A_0 X_{0,0} + X_{0,0} A_0^* &= -B \Omega B^* \quad (\text{I.5}) \\ (A_0 + i\omega_t I) X_{1,1} + X_{1,1} A_0^* &= -\left((1 + \mu_{-1}) A_{-1} X_{0,0} + (1 + \mu_{+1}) X_{0,0} A_{+1}^*\right) \\ A_0 X_{2,0} + X_{2,0} A_0^* &= -(1 + \mu_1)(A_{+1} X_{1,1} + X_{1,1} A_{+1}^*) - \\ &\quad (1 + \mu_{-1})(A_{-1} X_{1,1} + X_{1,1} A_{-1}^*) - \sum_{i=\pm 1} \sigma_i^2 A_i X_{0,0} A_i^*\end{aligned}$$

whose individual size is equal to the size of each block of the bi-infinite generalized Lyapunov equation (7.10). This harmonic-based decoupling is used for efficient computation of the second-order statistics of system (2.9).

REFERENCES

- Bakewell, H. P. and J. L. Lumley (1967). Viscous sublayer and adjacent wall region in turbulent pipe flow. *Phys. Fluids* 10(9), 1880–1889.
- Bamieh, B. and M. Dahleh (2001). Energy amplification in channel flows with stochastic excitation. *Phys. Fluids* 13(11), 3258–3269.
- Benner, P. (2004). Solving large-scale control problems. *IEEE Control Syst.* 24(1), 44–59.
- Benner, P. and T. Damm (2011). Lyapunov equations, energy functionals, and model order reduction of bilinear and stochastic systems. *SIAM J. Control Optim.* 49(2), 686–711.
- Benner, P., J.-R. Li, and T. Penzl (2008). Numerical solution of large-scale Lyapunov equations, Riccati equations, and linear-quadratic optimal control problems. *Numer. Linear Algebra Appl.* 15(9), 755–777.
- Bottaro, A., P. Corbett, and P. Luchini (2003). The effect of base flow variation on flow stability. *J. Fluid Mech.* 476, 293–302.
- Brandt, L., D. Sipp, J. O. Pralits, and O. Marquet (2011). Effect of base-flow variation in noise amplifiers: the flat-plate boundary layer. *J. Fluid Mech.* 687, 503–528.
- Buckwar, E. and C. Kelly (2014). Asymptotic and transient mean-square properties of stochastic systems arising in ecology, fluid dynamics, and system control. *SIAM J. Appl. Math.* 74(2), 411–433.
- Butler, K. M. and B. F. Farrell (1992). Three-dimensional optimal perturbations in viscous shear flow. *Phys. Fluids A* 4, 1637.
- Choi, K.-S. (2002). Near-wall structure of turbulent boundary layer with spanwise-wall oscillation. *Phys. Fluids* 14(7), 2530–2542.
- Damm, T. (2008). Direct methods and ADI-preconditioned Krylov subspace methods for generalized Lyapunov equations. *Numer. Linear Algebra Appl.* 15(9), 853–871.
- Del Álamo, J. C. and J. Jiménez (2003). Spectra of the very large anisotropic scales in turbulent channels. *Phys. Fluids* 15(6), 41–44.
- Del Álamo, J. C., J. Jiménez, P. Zandonade, and R. D. Moser (2004). Scaling of the energy spectra of turbulent channels. *J. Fluid Mech.* 500(1), 135–144.
- Dyke, M. V. (1964). Perturbation methods in fluid mechanics. *Academic Press*.
- Farrell, B. F. and P. J. Ioannou (1993). Perturbation growth in shear flow exhibits universality. *Phys. Fluids A* 5(9), 2298–2300.

- Farrell, B. F. and P. J. Ioannou (1998). Perturbation structure and spectra in turbulent channel flow. *Theoret. Comput. Fluid Dynamics* 11, 237–250.
- Farrell, B. F. and P. J. Ioannou (2002). Optimal perturbation of uncertain systems. *Stochastics Dyn.* 2(03), 395–402.
- Filo, M. and B. Bamieh (2018). An input-output approach to structured stochastic uncertainty in continuous time. *arXiv preprint arXiv:1806.09091*.
- Filo, M. and B. Bamieh (2020). An input-output approach to structured stochastic uncertainty. *IEEE Trans. Automat. Control*.
- Gardner, W. (1990). *Introduction to Random Processes: with Applications to Signals and Systems*. McGraw-Hill.
- Gustavsson, L. H. (1991). Energy growth of three-dimensional disturbances in plane Poiseuille flow. *J. Fluid Mech.* 98, 149.
- Henningson, D. S. and S. C. Reddy (1994). On the role of linear mechanisms in transition to turbulence. *Phys. Fluids* 6(3), 1396–1398.
- Hoyas, S. and J. Jiménez (2006). Scaling of the velocity fluctuations in turbulent channels up to $Re_\tau = 2003$. *Phys. Fluids* 18(1), 011702.
- Hoyas, S. and J. Jimenez (2008). Reynolds number effects on the Reynolds-stress budgets in turbulent channels. *Phys. Fluids* 20, 101511.
- Hwang, Y. and H. Choi (2006). Control of absolute instability by basic-flow modification in a parallel wake at low Reynolds number. *J. Fluid Mech.* 560, 465.
- Hwang, Y. and C. Cossu (2010a). Amplification of coherent streaks in the turbulent Couette flow: an input-output analysis at low Reynolds number. *J. Fluid Mech.* 643, 333–348.
- Hwang, Y. and C. Cossu (2010b). Linear non-normal energy amplification of harmonic and stochastic forcing in the turbulent channel flow. *J. Fluid Mech.* 664, 51–73.
- Ito, I. (1979). On the existence and uniqueness of solutions of stochastic integral equations of the Volterra type. *Kodai Mathematical Journal* 2(2), 158–170.
- Jovanovic, M. R. (2008, January). Turbulence suppression in channel flows by small amplitude transverse wall oscillations. *Phys. Fluids* 20(1), 014101 (11 pages).
- Jovanovic, M. R. and B. Bamieh (2005, July). Componentwise energy amplification in channel flows. *J. Fluid Mech.* 534, 145–183.

- Jovanovic, M. R. and M. Fardad (2008, August). \mathcal{H}_2 norm of linear time-periodic systems: a perturbation analysis. *Automatica* 44(8), 2090–2098.
- Jung, W., N. Mangiavacchi, and R. Akhavan (1992). Suppression of turbulence in wall-bounded flows by high-frequency spanwise oscillations. *Phys. Fluids A* 4(8), 1605–1607.
- Kim, J. and T. R. Bewley (2007). A linear systems approach to flow control. *Annu. Rev. Fluid Mech.* 39, 383–417.
- Ko, J., D. Lucor, and P. Sagaut (2011). Effects of base flow uncertainty on Couette flow stability. *Comput. Fluids* 43(1), 82–89.
- Kushner, H. J. (1967). *Stochastic stability and control*. Academic Press, New York.
- Luhar, M., A. S. Sharma, and B. J. McKeon (2014). Opposition control within the resolvent analysis framework. *J. Fluid Mech.* 749, 597–626.
- Marquet, O., D. Sipp, and L. Jacquin (2008). Sensitivity analysis and passive control of cylinder flow. *J. Fluid Mech.* 615, 221.
- McKeon, B. J. and A. S. Sharma (2010). A critical-layer framework for turbulent pipe flow. *J. Fluid Mech.* 658, 336–382.
- Moarref, R. and M. R. Jovanovic (2010, November). Controlling the onset of turbulence by streamwise traveling waves. part 1: Receptivity analysis. *J. Fluid Mech.* 663, 70–99.
- Moarref, R. and M. R. Jovanovic (2012, September). Model-based design of transverse wall oscillations for turbulent drag reduction. *J. Fluid Mech.* 707, 205–240.
- Moin, P. and R. Moser (1989). Characteristic-eddy decomposition of turbulence in a channel. *J. Fluid Mech.* 200(41), 509.
- Morra, P., O. Semeraro, D. S. Henningson, and C. Cossu (2019). On the relevance of Reynolds stresses in resolvent analyses of turbulent wall-bounded flows. *J. Fluid Mech.* 867, 969–984.
- Øksendal, B. (2003). Stochastic differential equations. In *Stochastic differential equations*, pp. 65–84. Springer.
- Pralits, J. O., L. Brandt, and F. Giannetti (2010). Instability and sensitivity of the flow around a rotating circular cylinder. *J. Fluid Mech.* 650, 513–536.
- Quadrio, M. and P. Ricco (2004). Critical assessment of turbulent drag reduction through spanwise wall oscillations. *J. Fluid Mech.* 521, 251–271.
- Rabin, S. M. E., C. P. Caulfield, and R. R. Kerswell (2012). Triggering turbulence efficiently in plane Couette flow. *J. Fluid Mech.* 712, 244.

- Ran, W., A. Zare, M. J. P. Hack, and M. R. Jovanovic (2019, September). Stochastic receptivity analysis of boundary layer flow. *Phys. Rev. Fluids* 4(9), 093901 (28 pages).
- Ran, W., A. Zare, and M. R. Jovanović (2021, January). Model-based design of riblets for turbulent drag reduction. *J. Fluid Mech.* 906, A7 (38 pages).
- Reddy, S. C. and D. S. Henningson (1993). Energy growth in viscous channel flows. *J. Fluid Mech.* 252, 209–238.
- Reddy, S. C., P. J. Schmid, J. S. Baggett, and D. S. Henningson (1998). On stability of streamwise streaks and transition thresholds in plane channel flows. *J. Fluid Mech.* 365, 269–303.
- Reddy, S. C., P. J. Schmid, and D. S. Henningson (1993). Pseudospectra of the Orr-Sommerfeld operator. *SIAM J. Appl. Math.* 53(1), 15–47.
- Reynolds, W. C. and W. G. Tiederman (1967). Stability of turbulent channel flow with application to Malkus’s theory. *J. Fluid Mech.* 27(2), 253–272.
- Ricco, P. (2004). Modification of near-wall turbulence due to spanwise wall oscillations. *J. Turbul.* 5, 20–20.
- Ricco, P. and M. Quadrio (2008). Wall-oscillation conditions for drag reduction in turbulent channel flow. *International Journal of Heat and Fluid Flow* 29(4), 891–902.
- Samuels, J. (1959). On the mean square stability of random linear systems. *IRE Trans. Circuit Theory* 6(5), 248–259.
- Schmid, P. J. (2007). Nonmodal stability theory. *Annu. Rev. Fluid Mech.* 39, 129–162.
- Schmid, P. J. and D. S. Henningson (1994). Optimal energy density growth in Hagen-Poiseuille flow. *J. Fluid Mech.* 277, 197–225.
- Schmid, P. J. and D. S. Henningson (2001). *Stability and Transition in Shear Flows*. New York: Springer-Verlag.
- Schmid, P. J., D. S. Henningson, M. R. Khorrami, and M. R. Malik (1993). A study of eigenvalue sensitivity for hydrodynamic stability operators. *Theor. Comput. Fluid Dyn.* 4(5), 227–240.
- Shanks, D. (1955). Non-linear transformations of divergent and slowly convergent sequences. *J. Math. Physics* 34(1-4), 1–42.
- Sidi, A. (2003). *Practical extrapolation methods: Theory and applications*, Volume 10. Cambridge University Press.

- Skogestad, S. and I. Postlethwaite (2007). *Multivariable feedback control: analysis and design*, Volume 2. Wiley New York.
- Stratonovich, R. L. (1966). A new representation for stochastic integrals and equations. *SIAM J. Control* 4(2), 362–371.
- Towne, A., A. Lozano-Durán, and X. Yang (2020). Resolvent-based estimation of space-time flow statistics. *J. Fluid Mech.* 883.
- Trefethen, L. N. and M. Embree (2005). *Spectra and pseudospectra: the behavior of nonnormal matrices and operators*. Princeton: Princeton University Press.
- Trefethen, L. N., A. E. Trefethen, S. C. Reddy, and T. A. Driscoll (1993). Hydrodynamic stability without eigenvalues. *Science* 261, 578–584.
- Weideman, J. A. C. and S. C. Reddy (2000, December). A MATLAB differentiation matrix suite. *ACM Trans. Math. Software* 26(4), 465–519.
- Willems, J. (1973). The circle criterion and quadratic Lyapunov functions for stability analysis. *IEEE Trans. Automat. Control* 18(2), 184–184.
- Wynn, P. (1966). Upon systems of recursions which obtain among the quotients of the padé table. *Numer. Math.* 8(3), 264–269.
- Zare, A. (2016). *Low-complexity stochastic modeling of wall-bounded shear flows*. Ph. D. thesis, University of Minnesota.
- Zare, A., Y. Chen, M. R. Jovanovic, and T. T. Georgiou (2017, March). Low-complexity modeling of partially available second-order statistics: theory and an efficient matrix completion algorithm. *IEEE Trans. Automat. Control* 62(3), 1368–1383.
- Zare, A., T. T. Georgiou, and M. R. Jovanovic (2020, May). Stochastic dynamical modeling of turbulent flows. *Annu. Rev. Control Robot. Auton. Syst.* 3, 195–219.
- Zare, A., M. R. Jovanovic, and T. T. Georgiou (2016). Perturbation of system dynamics and the covariance completion problem. In *Proceedings of the 55th IEEE Conference on Decision and Control*, pp. 7036–7041.
- Zare, A., M. R. Jovanovic, and T. T. Georgiou (2017, February). Colour of turbulence. *J. Fluid Mech.* 812, 636–680.
- Zare, A., B. K. Lieu, and M. R. Jovanovic (2012). Turbulent drag reduction by streamwise traveling waves. In *Proceedings of the 51th IEEE Conference on Decision and Control*, Maui, HI, pp. 3122–3126.
- Zare, A., H. Mohammadi, N. K. Dhingra, T. T. Georgiou, and M. R. Jovanović (2020, August). Proximal algorithms for large-scale statistical modeling and sensor/actuator selection. *IEEE Trans. Automat. Control* 65(8), 3441–3456.

BIOGRAPHICAL SKETCH

Dhanushki B. Hewawaduge is a Sri Lankan nationality and she obtained her BS degree in mathematics from the University of Peradeniya, Sri Lanka. During the first two years in the university, she studied mathematics and physics. At the end of her 2nd year, Dhanushki got selected to the special degree program in mathematics due to her high GPA, where she had the opportunity to learn complex principles in mathematics during the 3rd and 4th years. After graduating with an overall GPA of 3.68 and mathematics GPA of 3.75 in 2015, she worked as a teaching assistant from January 2016 to November 2016, and an instructor from January 2017 to July 2017, at the department of mathematics.

For her advanced studies, Dhanushki received admission to the University of Texas at Dallas as a PhD scholar in 2017 and was offered a teaching assistant position from the department of mathematical sciences. During the two years in the department, she maintained a GPA of 3.606 while taking advanced courses in mathematics.

With much interest in the improvement of her ability to apply mathematics to the solution of a more practical field, she had the privilege of receiving admission to the mechanical engineering department at UTD. Dhanushki joined the research group of Dr. Armin Zare for her graduate program at ME where she had the opportunity to work on a few publications and obtain a strong foundation in controls and fluid systems under Dr. Zare's great guidance. During her time at ME, she worked on a publication with Dr. Zare that presents an input-output approach to analyze the effect of persistent white-in-time stochastic base flow perturbations on the mean-square properties of the linearized Navier-Stokes equations, where its implementation is used to evaluate the robust performance of a flow control strategy involving wall oscillations in the presence of implementation imperfections.

Dhanushki is currently a PhD candidate at the department of electrical engineering at UTD.

CURRICULUM VITAE

Dhanushki B. Hewawaduge

December 08, 2022

Contact Information:

Department of Electrical Engineering
The University of Texas at Dallas
800 W. Campbell Rd.
Richardson, TX 75080-3021, U.S.A.

Phone: (469) 733-7164
Email: Dhanushki.Hewawaduge@utdallas.edu

Educational History:

B.S., Mathematics, University of Peradeniya, 2015
M.S., Applied mathematics, University of Texas at Dallas 2019

Publications:

Journal papers:

D. B. Hewawaduge and A. Zare, Input-output analysis of stochastic base flow uncertainty, *Phys. Rev. Fluids*, vol. 7, no. 7, p. 073901 (32 pages), July 2022

Refereed Proceedings:

D. B. Hewawaduge and A. Zare, The effect of base flow uncertainty on transitional channel flows, In *Proceedings of the 2022 American Control Conference*, Atlanta, GA, pp. 5050-5055, 2022

D. B. Hewawaduge, T. H. Summers, and A. Zare, Robustness of turbulence suppression in channel flows with imperfect transverse wall oscillations, In *Proceedings of the 2021 American Control Conference*, New Orleans, LA, pp. 292-297, 2021

Employment History:

Graduate Research assistant, The University of Texas at Dallas, Spring 2020 - Summer 2021
Graduate Teaching assistant, The University of Texas at Dallas, Fall 2017 - Spring 2019, Fall 2021 – present

Teaching Assistant, University of Peradeniya, Sri Lanka, January 2016 - December 2016
Instructor, University of Peradeniya, Sri Lanka, January 2017-July 2017